

AD-A246 399



2

# NAVAL POSTGRADUATE SCHOOL

## Monterey, California

DTIC  
ELECTE  
FEB 18 1992  
S D D



## THESIS

EMITTANCE MEASUREMENT OF THE NAVAL  
POSTGRADUATE SCHOOL LINEAR ACCELERATOR USING  
OPTICAL TRANSITION RADIATION TECHNIQUES

by

Mark Joseph Hellstern

September 1991

Thesis Advisor:

Xavier K. Maruyama

Approved for public release; distribution is unlimited

92 2 14 140

92-03980  
1000 1000 1000 1000 1000 1000

REPORT DOCUMENTATION PAGE												
1a. REPORT SECURITY CLASSIFICATION Unclassified			1b. RESTRICTIVE MARKINGS									
2a. SECURITY CLASSIFICATION AUTHORITY			3. DISTRIBUTION/AVAILABILITY OF REPORT Approved for public release; distribution is unlimited.									
2b. DECLASSIFICATION/DOWNGRADING SCHEDULE												
4. PERFORMING ORGANIZATION REPORT NUMBER(S)			5. MONITORING ORGANIZATION REPORT NUMBER(S)									
6a. NAME OF PERFORMING ORGANIZATION Naval Postgraduate School		6b. OFFICE SYMBOL (If applicable) 33	7a. NAME OF MONITORING ORGANIZATION Naval Postgraduate School									
6c. ADDRESS (City, State, and ZIP Code) Monterey, CA 93943-5000			7b. ADDRESS (City, State, and ZIP Code) Monterey, CA 93943-5000									
8a. NAME OF FUNDING/SPONSORING ORGANIZATION		8b. OFFICE SYMBOL (If applicable)	9. PROCUREMENT INSTRUMENT IDENTIFICATION NUMBER									
8c. ADDRESS (City, State, and ZIP Code)			10. SOURCE OF FUNDING NUMBERS									
			<table border="1"> <tr> <td>Program Element No.</td> <td>Project No.</td> <td>Task No.</td> <td>Work Unit Accession Number</td> </tr> <tr> <td></td> <td></td> <td></td> <td></td> </tr> </table>		Program Element No.	Project No.	Task No.	Work Unit Accession Number				
Program Element No.	Project No.	Task No.	Work Unit Accession Number									
11. TITLE (Include Security Classification) EMITTANCE MEASUREMENT OF THE NAVAL POSTGRADUATE SCHOOL LINEAR ACCELERATOR USING OPTICAL TRANSITION RADIATION TECHNIQUES												
12. PERSONAL AUTHOR(S) Hellstern, Mark J.												
13a. TYPE OF REPORT Master's Thesis		13b. TIME COVERED From To	14. DATE OF REPORT (year, month, day) September 1991	15. PAGE COUNT 128								
16. SUPPLEMENTARY NOTATION The views expressed in this thesis are those of the author and do not reflect the official policy or position of the Department of Defense or the U.S. Government.												
17. COSATI CODES			18. SUBJECT TERMS (continue on reverse if necessary and identify by block number)									
FIELD	GROUP	SUBGROUP	optical transition radiation, charged particle beams, free electron lasers, beam diagnostics									
19. ABSTRACT (continue on reverse if necessary and identify by block number) Using Optical Transition Radiation (OTR) beam diagnostics and Dr. Rule's clear foil interferometer analytic code, the normalized emittance of the Naval Postgraduate School (NPS) linear accelerator (linac) has been measured: the normalized horizontal emittance of $97\pi \pm 10\pi$ mm-mrad and the normalized vertical emittance of $54\pi \pm 8\pi$ mm-mrad. The experiment was performed independently twice using a Kapton foil/silicon mirror and a nitrocellulose foil/aluminum mirror Wartski interferometer. The Kapton foil provided an initial measurement of the emittance, and provided the lessons learned for the nitrocellulose measurement. The emittance of the NPS linac indicate that the value maybe too high for most free electron laser applications, but is very useful for radiation effect studies in high temperature superconductors, hardening, beam diagnostics, and for the production of x-rays through novel mechanisms such as transition radiation and parametric x-radiation generation. The beam divergence was determined by comparing the theoretically calculated OTR patterns with the experimental data OTR patterns. The clear foil amplitude algorithms in the code have been validated in the nitrocellulose analysis. In addition, thin clear foils, which approximate the radiation coherence length in the foil medium, provide high degrees of sensitivity to the foil's index of refraction, indicating that OTR may be used to determine indices of refraction in addition to measuring beam divergence. The diagnostic capabilities of OTR are proven as applicable to electron accelerators (including free electron lasers).												
20. DISTRIBUTION/AVAILABILITY OF ABSTRACT <input checked="" type="checkbox"/> UNCLASSIFIED/UNLIMITED <input type="checkbox"/> SAME AS REPORT <input type="checkbox"/> DTIC USERS			21. ABSTRACT SECURITY CLASSIFICATION Unclassified									
22a. NAME OF RESPONSIBLE INDIVIDUAL X. K. Maruyama			22b. TELEPHONE (Include Area code) (408) 646-2431	22c. OFFICE SYMBOL Ph/Mx								

Approved for public release; distribution is unlimited.

**Emittance Measurement of the Naval Postgraduate School  
Linear Accelerator Using Optical Transition Radiation Techniques**

by

**Mark J. Hellstern  
Lieutenant, United States Navy  
B. S., United States Naval Academy**

Submitted in partial fulfillment  
of the requirements for the degree of

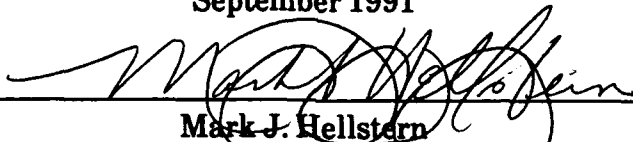
**MASTER OF SCIENCE IN PHYSICS**

from the

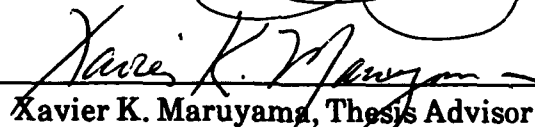
**NAVAL POSTGRADUATE SCHOOL**

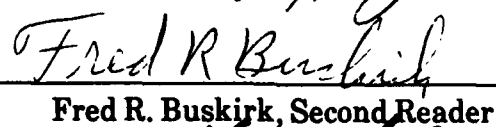
**September 1991**

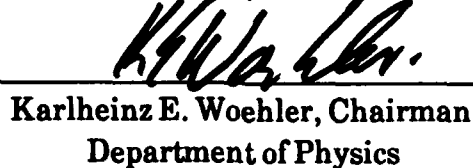
**Author:**

  
Mark J. Hellstern

**Approved by:**

  
Xavier K. Maruyama, Thesis Advisor

  
Fred R. Buskirk, Second Reader

  
Karlheinz E. Woehler, Chairman  
Department of Physics

## ABSTRACT

Using Optical Transition Radiation (OTR) beam diagnostics and Dr. Rule's clear foil interferometer analytic code, the normalized emittance of the Naval Postgraduate School (NPS) Linear Accelerator (linac) has been measured: the normalized horizontal emittance of  $97\pi \pm 10\pi$  mm-mrad and the normalized vertical emittance of  $54\pi \pm 8\pi$  mm-mrad. The experiment was performed independently twice using a Kapton foil/silicon mirror and a nitrocellulose foil/aluminum mirror Wartski interferometer. The Kapton foil provided an initial measurement of the emittance, and provided lessons learned for the nitrocellulose foil measurement. The emittance measurement of the NPS linac indicate that the value maybe too high for most free electron laser applications, but is very useful for radiation effect studies in high temperature superconductors, hardening, beam diagnostics, and for the production of x-rays through novel mechanisms such as transition radiation and parametric x-radiation generation.

The beam divergence was determined by comparing theoretically calculated OTR patterns with the experimental data OTR patterns. The clear foil amplitude algorithms in the code have been validated in the nitrocellulose foil analysis. In addition, thin clear foils, which approximate the radiation coherence length in the foil medium, provide high degrees of sensitivity to the foil's index of refraction, indicating that OTR may be used to determine indices of refraction in addition to measuring divergence. The diagnostic capabilities of OTR are proven as applicable to electron accelerators (including free electron lasers).

## TABLE OF CONTENTS

<b>I. INTRODUCTION.....</b>	<b>1</b>
A. HISTORICAL BACKGROUND.....	1
B. TRANSITION RADIATION AS A DIAGNOSTIC TOOL .....	2
C. MEASUREMENT OF THE NPGS LINAC EMITTANCE.....	3
<b>II. THEORETICAL BACKGROUND.....</b>	<b>6</b>
A. THEORETICAL DEVELOPMENT: SINGLE FOIL.....	6
B. OBSERVATION OF OPTICAL TRANSITION RADIATION.....	10
C. WARTSKI'S TWO-FOIL INTERFEROMETER.....	12
D. CLEAR FOIL EFFECTS AND RULE'S COMPUTER CODE.....	18
<b>III. EXPERIMENTAL PROCEDURE.....</b>	<b>24</b>
A. EXPERIMENTAL SETUP.....	26
B. ALIGNMENT OF THE SITCAM .....	31
C. ANGULAR AND DISTANCE CALIBRATION.....	34
D. THE EMITTANCE MEASUREMENT: SEPTEMBER 1990.....	35
E. COHERENCE, EMITTANCE MEASUREMENTS: NOV. 1990.....	38
<b>IV. EMITTANCE MEASUREMENT AND DATA ANALYSIS.....</b>	<b>43</b>
A. INTRODUCTORY REMARKS .....	43
B. EMITTANCE MEASUREMENT: KAPTON FOIL.....	43
C. CLEAR FOIL AMPLITUDE AND COHERENCE EFFECTS.....	58
D. THE EMITTANCE MEASUREMENT: NOVEMBER 1990.....	85
E. COMPARISON TO OTHER LINACS .....	101
<b>V. CONCLUSIONS AND RECOMMENDATIONS.....</b>	<b>105</b>
A. SUMMARY OF CONCLUSIONS .....	105
B. RECOMMENDATIONS.....	107

LIST OF REFERENCES.....	109
APPENDIX A: PROGRAM OPERATION.....	112
INITIAL DISTRIBUTION LIST.....	120

Accession For	
NTIS CRA&I	<input checked="" type="checkbox"/>
DTIC TAB	<input type="checkbox"/>
Unannounced	<input type="checkbox"/>
Justification	
By	
Distribution /	
Availability Codes	
Dist	Avail and/or Special
A-1	



## ACKNOWLEDGMENTS

I'd like to thank Professor X. K. Maruyama for his guidance, support, and good humor during the experiments and the writing of this thesis. My appreciation for the capricious nature of research was greatly enhanced through his efforts. Professor Buskirk deserves special recognition for his time in operating the linac during the experiment and his appreciation for fine wine which matches my own.

Dr. Donald Rule not only provided me with the accurate analytic program to complete my work, but he also gave me an insider's look into the world of government research. Moreover, his friendship and support was appreciated during my experience tour. Dr. Ralph Fiorito is the most meticulous scientist that I've ever met, and his desire for accurate measurements was responsible for the success of this measurement. Mr. Don Snyder and Mr. Harold Reitdyk are the glue which keeps the linac together, and without whom this experiment would never have been completed.

Finally, I'd like to thank my wife Jan for her constant efforts to ensure that this great procrastinator completed this thesis before the graduation deadline. This work is dedicated to her.

## **I. INTRODUCTION**

### **A. HISTORICAL BACKGROUND**

Transition radiation (TR) is produced whenever a charged particle traverses the boundary between different dielectric media. This radiation has a broad spectrum of frequencies ranging from the microwave to the x-ray regions depending on the energy of the incident particle. Ginsburg and Frank [Ref. 1] published the first theoretical treatment in 1946 and particularly noted that the intensity of the generated radiation, the polarization of the electric field, and the angular distribution of the TR are strongly dependent on the dielectric constants of the media and that TR is not connected to changes in the velocity of the charged particle. These particular aspects of TR are applicable as a diagnostic tool for the analysis of low to medium energy particle accelerators.

Since the introduction of the concept, many scientific investigations have been accomplished (more than five hundred papers published from 1946 to 1983) studying the TR effects in such environments as the boundaries between dielectric media, plasmas, inhomogeneous media, and time varying dielectric media. Ginsburg and Tsytovich [Ref. 2], Ter-Mikaelin [Ref. 3], and Garibian [Ref. 4] provide excellent overviews and treatises on the established theoretical concepts and experimental analyses. The calculations and mathematics involving TR are extremely involved and complex. Moreover, the formulae were developed by different groups of experimentalists independently of each other, and to add to the confusion, there was a lack of specific standards with respect to key concepts and universal conventions. In 1975, Wartski [Ref. 5]

attempted to rectify the confusion by using fundamental theories, basic hypotheses, and adopted conventions to develop the formulae used in Transition Radiation analysis. In addition, Wartski demonstrated the utility of Optical Transition Radiation (OTR) analysis for particle beam diagnostics. Rule and Fiorito et al. [Ref. 6-8] refined and extended Wartski's work by developing analytical solutions to the derived equations and applying these to the experimental analyses of charged particle beams.

## **B. TRANSITION RADIATION AS A DIAGNOSTIC TOOL**

Transition Radiation (TR) has a number of features which enable it to be used for diagnostic applications: as mentioned before, its intensity and angular distribution are dependent on the particle's energy; TR has a broad frequency spectrum with an upper limit related to the Lorentz factor,  $\gamma$ ; it is polarized such that the electric field vectors point along the radii about the emitted radiation cone's axis; and it has a real time capability for analysis of beam characteristics. Wartski [Ref.5] first showed how to apply Optical Transition Radiation (OTR) analysis to particle beams of energies between 30 and 70 Mev. He developed both the single foil techniques for beam profile measurements and the Wartski two-foil interferometer which utilizes OTR patterns to show that the fringe visibility is a function of the beam divergence and, consequently, beam emittance is measured. His endeavors sparked research in analytic techniques of both non-electron charged particle beams and electron beams including free electron lasers (FEL's). Wartski et al. [Ref. 9] have published results on using OTR techniques to analyze proton beams and have shown that the techniques reduce beam disturbance by an order of magnitude while providing the information required on the beam characteristics.

In addition, Rule and Fiorito et al. [Ref. 10] have developed algorithms which follow Wartski's theoretical development and incorporated these into a computer code to use for comparison of the theory to actual beam OTR patterns. Fiorito et al. [Ref 6-8] have applied these computer programs to the emittance measurements of the EG&G accelerator, and have extended the energy of the beam analysis to greater than 100 Mev for the emittance and profile measurement of the Boeing Free Electron Laser [Ref. 11].

### C. MEASUREMENT OF THE NPGS LINAC EMITTANCE

The purpose of this thesis is to use the previously developed OTR measurement techniques to determine the emittance and the divergence of the Naval Postgraduate School (NPGS) Linear Accelerator (Linac) as developed in Reid's Thesis [Ref. 12]. Using the Rule et al. analytic computer code, the captured one dimensional beam OTR intensity patterns are compared to theory using the parameters of the experiment, varying these parameters within their margins of error, and allowing the divergence to be a free parameter. The divergence,  $\theta_{RMS}$ , which gives the best fit of the data to the theory and the measured RMS beam radius are multiplied to give the emittance in equation (1):

$$\epsilon_{RMS} = Radius_{RMS} \theta_{RMS} \quad (1)$$

The emittance measurement was first accomplished using first a Kapton clear foil interferometer with a silicon mirror later an independent measurement using a nitrocellulose transparent foil interferometer with an aluminum mirror was made. Both measurements are compared to each other and analyzed for differences both in technique of the data acquisition and the induced errors.

Moreover, the emittance of the NPS Linac is compared to other emittance measurements of other electron linear accelerators. Another aspect of this investigation compares the differences between thick and thin transparent foils with respect to coherence effects in the OTR patterns and the validation of the analytic computer code developed by Rule for clear foil amplitude effects for nitrocellulose (the foil material).

The thesis is divided into five chapters with Chapter I, the introduction, providing a historical background and purpose. Chapter II describes the theory as developed primarily by Wartski and ties these formulae into a description of the analytical expressions used by Rule et al. for the two-foil interferometer and clear foil OTR effects. Chapter III contains the experimental setup and experimental procedure which is largely based on Reid's thesis since both experiments ran consecutively for the clear foil interferometer measurement. The comparison of the foil thicknesses used the same procedure since the OTR measurement techniques do not differ, but are standardized. Chapter IV describes the emittance measurements for both the Kapton foil and the nitrocellulose foil. The comparison of the two measurements are accomplished and, additionally, the results are compared to similar linacs. The chapter also displays the results of the coherence effects of thick and thin clear foils and compares the data to the theoretical fits generated from the computer code. These results are discussed in relation to the theory, and the differences are analyzed with recommendations for improvement or change. Moreover, the effects of filter bandwidth on the OTR patterns are discussed with regard to computer modelling of the filter. Chapter V contains a synopsis of the

conclusions and results of the analysis as well as recommendations for improving the OTR techniques.

.

.

.

.

## II. THEORETICAL BACKGROUND

### A. THEORETICAL DEVELOPMENT: SINGLE FOIL

The theory of Transition Radiation (TR) is extremely complicated and contains many cumbersome formulae. This chapter provides an overview of the derivations developed mainly in Wartski's dissertation and applied to the analytical solutions for the computer code designed by Rule et al. The impetus of the key principles is directed toward highly relativistic particle treatment as applied to charged particle beams.

Transition Radiation occurs whenever a charged particle traverses a boundary between different dielectric media. Ginsburg and Frank [Ref. 1] proposed the simplest case of TR to predict the effects of the phenomena: the case of a charged particle crossing a planar boundary between two media of different constant dielectrics (see Figure 1). The intensity and the spectrum

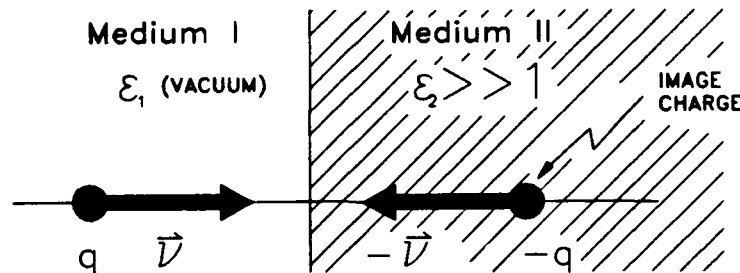


**Figure 1: Schematic of a charged particle approaching a dielectric medium with a velocity ( $v$ ). Note that the image charge approaches with velocity ( $-v$ ) in order that the Maxwell equations are satisfied at the far field and the boundary.**

of the emitted TR is a strong function of the particle's energy and depends on its trajectory with respect to the boundary normal, the dielectric constants of the media, and the angle of observation.

In order to satisfy the boundary conditions for the electric fields involved when the particle is near the interface, the solutions of the homogeneous Maxwell equations, the inhomogeneous Maxwell equations, and the radiation fields must be combined using the particle as the source. To avoid complicated mathematics, Wartski [Ref. 5] considers a collapsing dipole produced by a charged particle (q) having velocity (v) travelling from a perfect vacuum to a dielectric medium ( $\epsilon_2$ ) along a beam line normal to the interface (a mirror), and its image charge (-q) travelling with velocity (-v) on the opposite trajectory as in Figure 1. The TR caused by the collapsing dipole is given by the formula for radiation from charges whose velocities change rapidly with respect to their period ( $2\pi/\omega$ ) of the light generated at a frequency  $\omega$ , given by Garibian [Ref.4] for the resulting radiation intensity (I):

$$\frac{d^2 I}{d\omega d\Omega} = \frac{e^2 \beta^2 \sin^2 \theta \cos^2 \theta}{\pi^2 c (1 - \beta^2 \cos^2 \theta)^2} \left| \frac{(\epsilon - 1) [1 - \beta^2 - \beta(\epsilon - \sin^2 \theta)^{1/2}]}{(\epsilon \cos \theta + (\epsilon - \sin^2 \theta)^{1/2}) [1 - \beta(\epsilon - \sin^2 \theta)^{1/2}]} \right|^2 \quad (2)$$

where  $\epsilon$  is the complex dielectric constant of the medium related to the complex index of refraction,  $n^*$ , by equation (2A):

$$\epsilon = \frac{|n^*|^2}{\mu_o} \quad (2A)$$

and  $|n^*|$  is defined as the complex modulus index of refraction in equation (2B):

$$|n^*| = |n + iK| = \sqrt{n^2 + K^2}$$

where  $n$  is the real part of the index of refraction and  $K$  is the imaginary part of the refractive index or, more commonly, the attenuation index. Wartski [Ref. 13] shows that for highly relativistic particles and  $|\epsilon| \gg 1$  that equation (2) simplifies to:

$$\frac{d^2 I}{d\omega d\Omega} = \frac{e^2 \beta^2 \sin^2 \theta}{4\pi^2 c (1 - \beta \cos \theta)^2} \quad (3)$$

where  $d\Omega$  is a solid angle about  $\theta$ , the angle of observation measured from the boundary surface normal, and  $\beta = v/c$  where  $c$  is the speed of light in a vacuum. For the case of normal incidence, one can readily ascertain that the electric field lies in the plane containing the surface normal and the direction vector of the emitted radiation, because the radiation is based on a dipole type radiation field. Moreover, the maximum intensity of the TR occurs at an angle of:

$$\theta_{MAX} \cong 1/\gamma, \text{ where } \gamma = (1 - \beta^2)^{1/2} = E/mc^2 \quad (4)$$

where  $E$  is the total energy of the particle and  $mc^2$  is the rest energy of the same particle.  $\gamma$  is commonly referred to as the Lorentz factor.

Keeping in mind that the boundary is a mirror interface, Wartski [Ref. 5] shows that the intensity ( $I$ ) of the backward radiation emission is easily obtained by changing  $\beta$  to  $-\beta$  in equation (2) to yield for the extreme relativistic case corresponding to equation (3):

$$\frac{d^2 I}{d\omega d\Omega} = \frac{e^2 \beta^2 \sin^2 \theta}{4\pi^2 c (1 - \beta \cos \theta)^2} \left| \frac{\sqrt{\epsilon} - 1}{\sqrt{\epsilon} + 1} \right|^2 \quad (5)$$

where  $\theta$  is the emission angle measured from the  $-v$  direction. This result is easily understood if one realizes that this equation is equation (3) multiplied by the Fresnel relation for reflection and is derived by the Williams-Weizaker

method for the reflection of virtual photons due to the relativistic incident particle energies [Ref. 13].

One realizes that the above formulae are only valid at a distance from the boundary/interface. Therefore, following the treatise by Garibian [Ref. 4], the location of the detection point for the observation of the fully developed radiation wave must be greater than the formation zone in a vacuum for a given frequency  $\omega$ :

$$L_V = (c / \omega) \beta (1 - \beta \cos \theta)^{-1} \quad (6)$$

This concept of formation zone is based on the total field which includes the particle's field, the radiation field, and the fields induced in the media on either side of the boundary. In addition, the total field must adjust to the change in the dielectric constant as the particle crosses the boundary. Basically, the adjustment occurs within the formation zone [Ref. 3]. Garibian [Ref. 4] followed the Landau-Lifshitz classical method by assuming that all the fields can be convolved into four-fold Fourier integrals in the wave-vector domain and the particle can be represented as a Dirac-delta function to derive an expression for the physical interpretation of  $L_V$ . The quantity,  $L_V$ , can be understood as the length (in a vacuum) measured along a particle's trajectory for which the phase difference between the radiation field and the particle's field is 1 radian such that:

$$L_V \times [\omega / v - (\omega / c) \cos \theta] = 1 \text{ radian} \quad (7)$$

where  $\omega/v$  ( $v$  is the velocity of the particle) and  $(\omega/c)\cos\theta$  are the longitudinal components of the particle and radiation fields respectively. The arbitrary value of one radian in the phase difference is the basis of the difference between the

formation zone and the fully developed wave zone. Moreover, the formation zone is thought of as the length required for the redistribution of the fields or the coherence length of the radiation [Ref. 5]. At relativistic energies, Wartski [Ref. 13] shows that the coherence length is (using small angle approximations with respect to the beam line):

$$L_V = \frac{\lambda}{\pi} [\gamma^{-2} - \theta^2]^{-1} \quad (8)$$

where  $\lambda$  is the wavelength of the emitted radiation,  $\theta$  is the angle of incidence on the interface, and  $1/\gamma$  is the angle of peak intensity of the radiation. Therefore,  $L_V$  increases as the square of the energy near the maximum intensity angle  $\gamma^{-1}$ . Yuan [Ref. 14] has measured and verified formation lengths with these formulae using stacks of aluminum foils with air gaps. Similarly, the formation zone in the medium,  $L_m$ , is derived and given by Garibian [Ref. 4]:

$$L_m = \frac{\beta c}{\omega} [1 - \beta \sqrt{\epsilon} \cos \theta]^{-1} \quad (9)$$

where  $\epsilon$  is the complex dielectric of the medium and  $\omega$  is the frequency of the radiation. Again, the arbitrary one radian phase difference used in defining  $L_m$  is chosen in order that the particle and radiation fields add coherently.

## B. OBSERVATION OF OPTICAL TRANSITION RADIATION

In order to observe Optical Transition Radiation (OTR), the foil was aligned to 45 degrees from the beam line axis as shown in Figure 2. In this way, the backward emission is observed at 90 degrees from the beam axis. The theoretical formulae are beyond the scope of this text, but Pafomov [Ref. 15] offers an excellent treatise on the subject. Image charge theory for highly

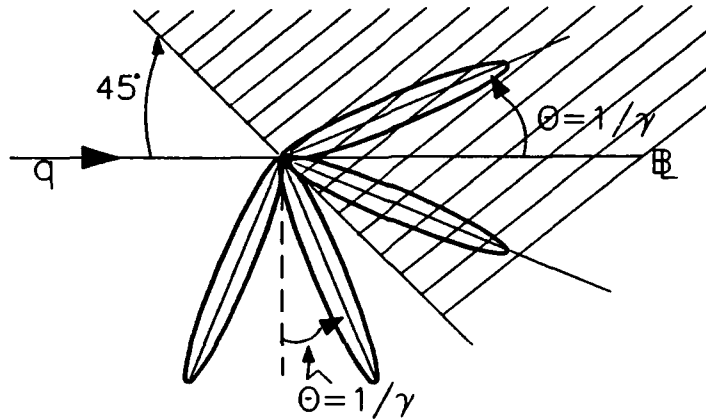


**Figure 2: By rotating the foil 45°, the observation of the radiation occurs at 90° from the beam axis by observing the backward emission due to Fresnel reflection. Forward emission is not measurably affected by incidence angle for highly relativistic particles.**

relativistic particles [Ref. 13] shows that the forward OTR emission is not measurably affected by the incidence angle and remains symmetric about the beam axis, but the backward OTR emission takes the form of equation (5), where the Fresnel reflection expression is dependent on the incidence angle.

In the limiting cases of a small observation angle,  $\theta_o$ , medium-vacuum forward OTR emission ( $\beta \sim 1$  and  $\epsilon_1 > \epsilon_{vac}$ ) as in Figure 3, equation (5), by integrating in the angular interval  $(0-\theta)$ , becomes [Ref. 16]:

$$\frac{dI_2(\omega)}{d\omega} \approx \frac{e^2}{2\pi c} \gamma^4 \theta_o^4 \text{ where } \theta_o \ll \gamma^{-1} \quad (10)$$

which shows that the intensity (for a single foil) per frequency interval emitted in small solid angles varies as the Lorentz factor to the fourth power. These equations have been independently verified by Wartski [Ref. 13] in the OTR region. Similarly, for observation angles  $\theta_o > \gamma^{-1}$ , the intensity per frequency

interval varies logarithmically with  $\gamma^2$  as in equation (11):

$$\frac{dI_2(\omega)}{d\omega} \approx \frac{e^2}{\pi c} \left[ \ln(\gamma^2 \theta_o^2) - 1 \right] \quad (11)$$

Finally, in Figure 4 [Ref. 13], Wartski shows that the backward observed OTR incident on an aluminum foil at 45 degrees exhibits an asymmetry in the lobes of the peak intensities due to the oblique incidence of the particles in the beam divergence. Furthermore, for a single foil, he notes that at  $\gamma \sim 100$ , the asymmetry is of the order of a few percent. This phenomena figures significantly in the analysis of the data.

### C. WARTSKI'S TWO-FOIL INTERFEROMETER

By using a two-foil TR interferometer developed by Wartski et al. [Ref. 16], a  $\gamma^8$  dependence for the intensity of the central peak of the interference pattern is obtained. The interferometer consists of two parallel foils positioned 45 degrees from the beam axis. In this configuration, the front face of the second foil (II) acts as a mirror for the forward TR emission produced by the back of the first foil (I), as shown in Figure 5. The radiation field from (I) adds coherently with the backward TR of the mirror (II) since both are caused by the same particle. The resulting TR pattern is centered on the angle of specular reflection and the phase difference between the TR on the first and second is [Ref. 13]:

$$\phi = (2\pi L / \lambda \beta)(1 - \beta \cos \theta) = L / L_V \quad (12)$$

where  $L$  is the separation between the foils,  $\theta$  is the direction measured from the angle of specular reflection, and  $L_V$  is the formation length in a vacuum.

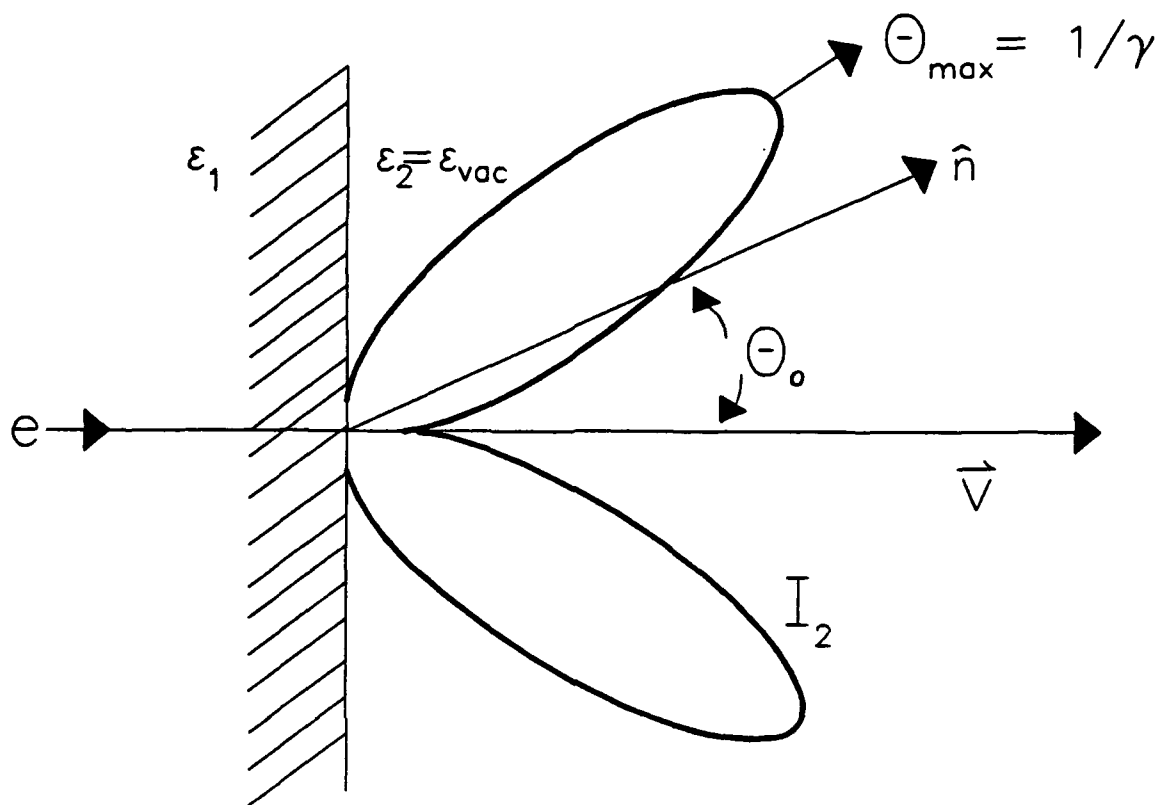


**Figure 3: OTR in the forward direction at an interface. Note: the direction of observation is along  $\hat{n}$  and  $\theta_0$  is the angle wrt the beam velocity direction  $\vec{v}$ .**

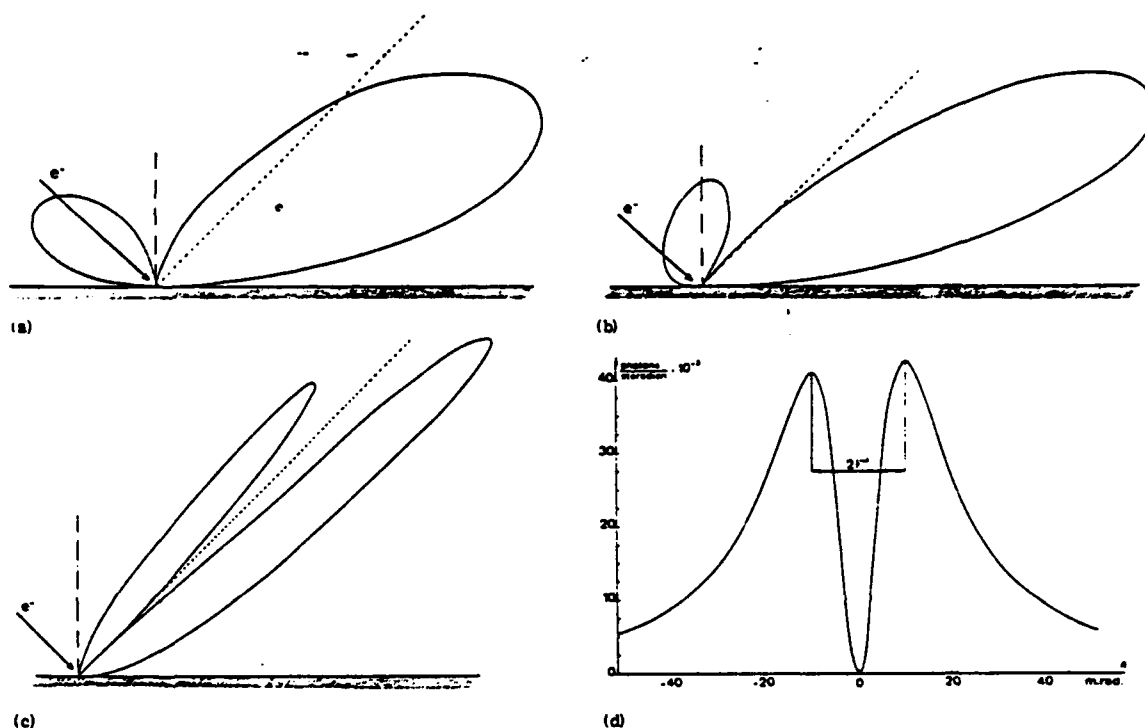


**Figure 4: Note: from Ref. 13. Theoretical transition patterns for different energies incident at  $45^\circ$ ,  $\lambda=4046\text{\AA}$ ,  $\Delta\lambda=1\text{\AA}$ ,  $n=0.45$ ,  $k=3.98$  (a)  $\gamma=1.05$  (b)  $\gamma=2$  (c)  $\gamma=10$  (d)  $\gamma=100$  [ in (d),  $\theta$  is measured from the angle of specular reflection].**

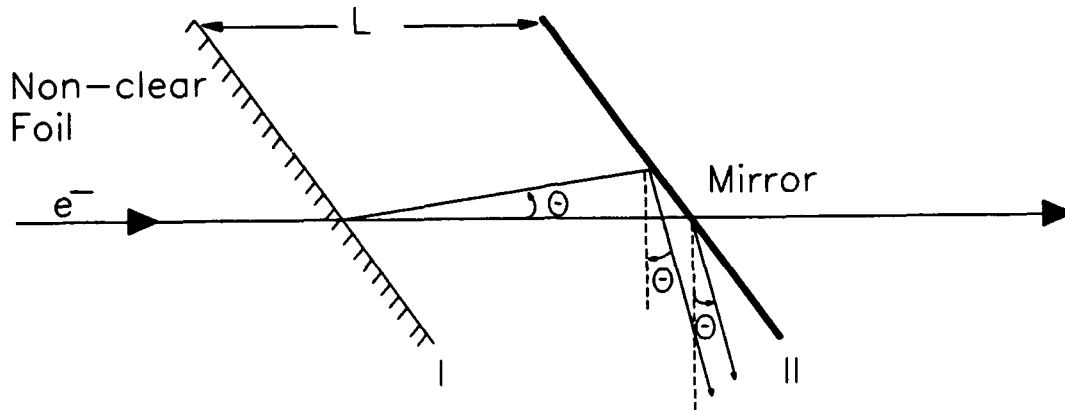


**Figure 5: Two parallel foils (angle of incidence  $45^\circ$ ) of the foil to vacuum, vacuum to mirror case.**

Wartski [Ref. 16] used the virtual photon method to analyze the interference effects for the intensity which translates simply as multiplying the intensity for a single foil by a Fresnel term  $F(\psi, \theta, \omega)$ :

$$\frac{d^2 I}{d\omega d\Omega} = F(\psi, \theta, \omega) \frac{e^2 \beta^2 \sin^2 \theta}{4\pi^2 c (1 - \beta \cos \theta)^2} |1 - e^{-j\phi}|^2 \quad (13)$$

where  $F(\psi, \theta, \omega)$  is the reflectance for light with the electric field vector parallel to the plane of incidence [Ref 13],  $\theta$  is the angle of observation measured from the angle of specular reflection, and  $\psi$  is the angle of the incident particle. A more complete treatise on oblique incidence is given by Ashley [Ref.17]. Wartski [Ref. 13] further shows that for highly relativistic beams ( $\beta \sim 1$ ,  $\theta \sim \gamma^{-1}$ )

the  $\theta$ -dependence of  $F(\psi, \theta, \omega)$  may be ignored transforming equation (13) into:

$$\frac{d^2 I}{d\omega d\Omega} = 4F(\psi, \omega) \frac{e^2 \theta^2}{\pi^2 c (\gamma^{-2} + \theta^2)^2} \sin^2 \left( \frac{\pi L}{2\lambda} (\gamma^{-2} + \theta^2) \right) \quad (14)$$

Note that the interference patterns are analogous to optical interference patterns which produce fringe patterns. In his dissertation [Ref. 5], Wartski gives the interference order ( $p$ ) of the fringes for equation (13) by:

$$p = \frac{L}{\lambda \beta} (1 - \beta \cos \theta) = \frac{L}{2\pi L_V} \quad (15)$$

where  $L$  is the foil separation and  $L_V$  is the coherence length in a vacuum. As  $\beta$  approaches 1, equation (15) becomes:

$$p \approx \frac{L}{2\lambda} (\gamma^{-2} + \theta^2) \quad (16)$$

Therefore, the local minimum  $\theta_{\min}$  occurs when  $p$  is an integer  $k$ . The local maximum  $\theta_{\max}$  occurs when  $p = k \pm 0.5$ . The interference order  $p$  at the center of specular reflection is defined as:

$$p_0 = \frac{L}{2\lambda} \gamma^{-2}, \theta = 0 \quad (17)$$

Further, the angle of local maximum  $\theta_M$  and local minimum  $\theta_m$  are approximated by:

$$\theta_{M,m} = \frac{2\lambda}{L} (p - p_0), \text{ where } p = k \text{ or } k \pm 0.5 \text{ respectively} \quad (18)$$

The order of interference is shown in equation (17) to be inversely proportional to the square of the Lorentz factor.

Wartski et al. [Ref. 16] used the interferometer to measure the RMS beam divergence after passing it through aluminum foils. The angles were

measured to tenths of milliradians. This is achieved by assuming a Gaussian distribution in angle and averaging equation (14) over this distribution. To describe this technique in more detail, Wartski [Ref. 5] showed that the mean angle at which OTR appears is the angle of specular reflection. If the beam has an angular divergence (see Figure 6), then the particles have different angles of incidence upon the TR foil centered around the angle of specular reflection. If the angle of a particular particle is  $\alpha$ , then the OTR appears at an angle  $\alpha$  to the

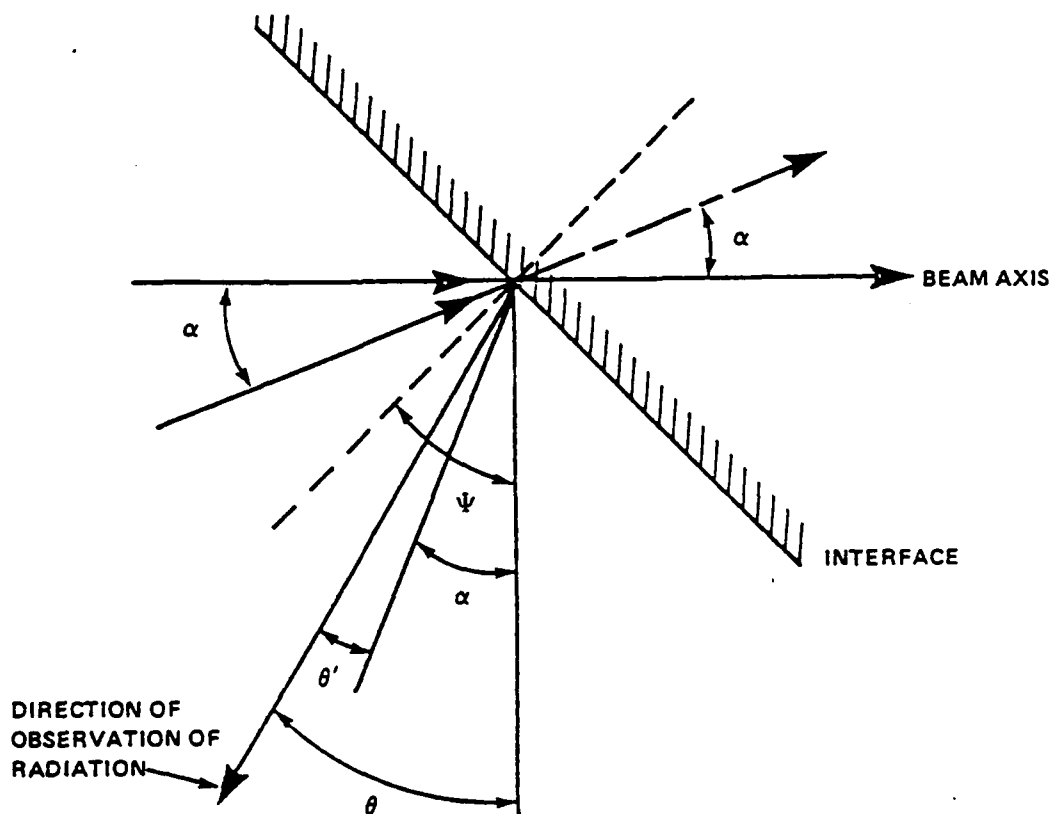


**Figure 6: Definition of the particular angle  $\alpha$  with respect to the beam axis, the angle of specular reflection  $\psi$ , and the observation angle  $\theta$  for a particle encountering a boundary at an oblique incidence [Ref. 5,8].**

axis of specular reflection. The interest in the aforementioned is that the intensity of the radiation at any point in the plane of observation is a function of the observation angle  $\theta$ . This angular information is a valuable diagnostic tool for beam analysis.

Since the experiment is concerned with optical frequencies one must consider the effects of finite bandwidth on the intensity. Wartski [Ref. 13] integrates equation (14) over a finite bandwidth ( $\Delta\lambda$ ) to give:

$$\frac{dI}{d\Omega} = F(\psi, \omega) \frac{e^2 L^2 \Delta\lambda \sin^2 \theta}{\pi \lambda (\lambda^2 p^2)} [1 - \text{sinc}(\pi p \Delta\lambda / \lambda) \cos(2\pi p)] \quad (19)$$

where  $\Delta\lambda$  is the bandwidth of the wavelength,  $L$  is the foil separation, and  $p$  is the interference order. Equation (19) shows that as the bandwidth  $\Delta\lambda$  increases, fringe visibility will decrease or wash out. This phenomena is verified in Longstaff's thesis [Ref. 18]. Discussion of finite bandwidth modelling is included in chapters 4 and 5.

#### D. CLEAR FOIL EFFECTS AND RULE'S COMPUTER CODE

The previous section described the radiation effects due to a two-foil non-clear interferometer, and most of the concepts apply to the emittance measurement. The NPS novel experiment utilized the two-foil interferometer concept, but incorporated a clear front foil and a mirror which added another intensity amplitude of TR caused by the forward TR of the front surface of the clear foil as shown in Figure 7. The transparent nature of the foil allowed the forward OTR from the front surface of the foil to travel through the foil into the vacuum to be reflected off the metal mirror. This additional radiation produces

# Interferometer and OTR Amplitudes

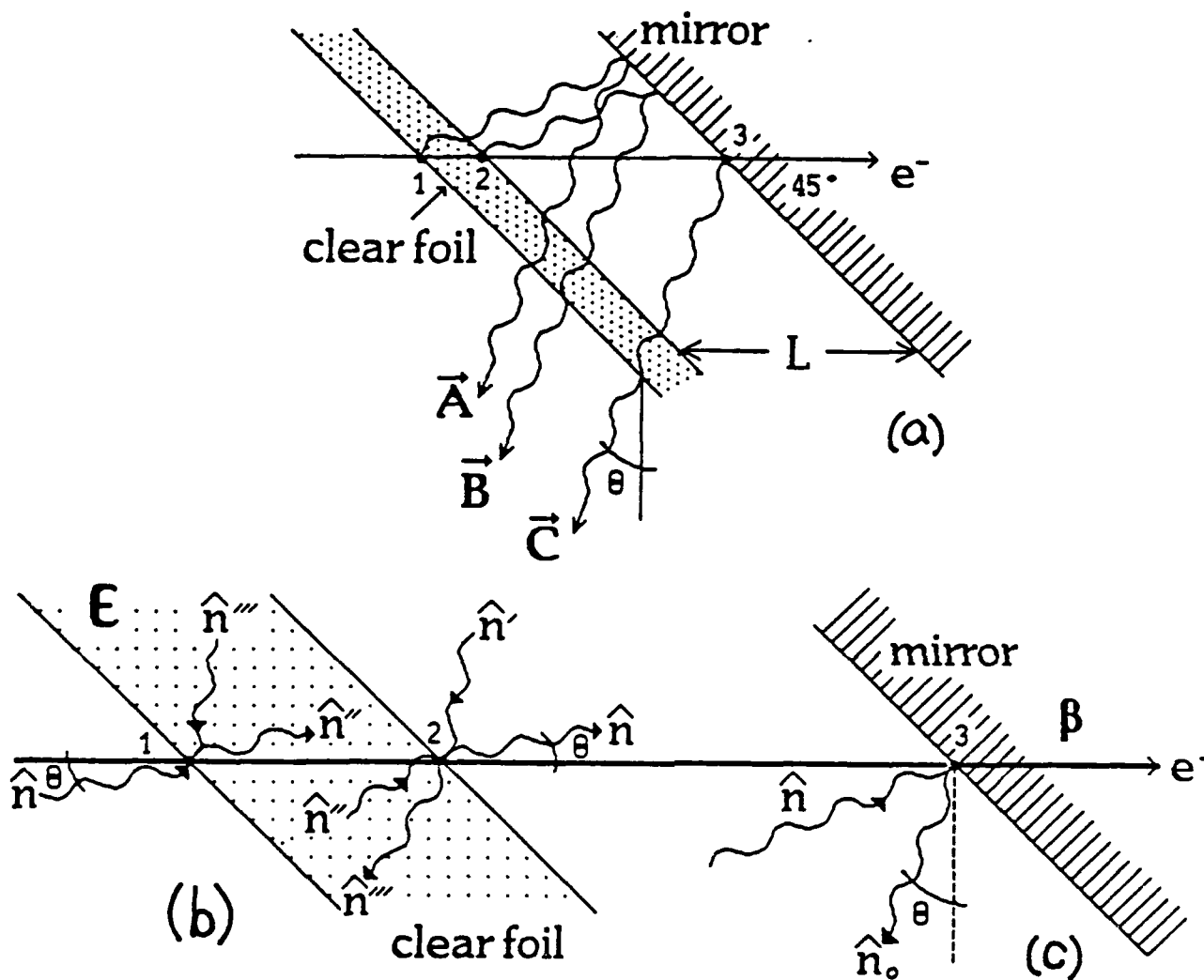


**Figure 7: (a) the combined effects of the OTR produced by the front and back surfaces of the clear foil and the backward OTR from the mirror. The amplitudes add coherently. (b) the clear foil directional components. (c) the mirror's directional components [Ref. 19].**

an additional interference term by adding coherently with the radiation caused by the subsequent interfaces [Ref. 13]. Rule [Ref. 19] shows that the resulting intensity of TR per unit frequency interval is (refer often to Figure 7):

$$\frac{d^2 I}{d\omega d\Omega} = \frac{e^2}{4\pi^2 c} \left| r_m (\vec{A} + \vec{B}) e^{-i\phi_{23}} - \vec{C} \right|^2, \quad \phi_{23} = L / L_V \quad (20)$$

where according to Wartski [Ref. 5] the amplitudes are given by:

$$\vec{A} = (1 - T e^{i\phi_{12}}) \frac{\vec{\beta} \times \hat{n}}{1 - \vec{\beta} \cdot \hat{n}} + \frac{R(\vec{\beta} \times \hat{n}')}{1 - \vec{\beta} \cdot \hat{n}'} \quad (20A)$$

$$\vec{B} = \frac{T(e^{-i\phi_{12}} - 1)}{t' \sqrt{\epsilon}} \frac{\vec{\beta} \times \hat{n}''}{1 - \sqrt{\epsilon} \vec{\beta} \cdot \hat{n}''} + \frac{Tr'(e^{-i\phi_{12}} - 1)}{t' \sqrt{\epsilon}} \frac{\vec{\beta} \times \hat{n}'''}{1 - \sqrt{\epsilon} \vec{\beta} \cdot \hat{n}'''} \quad (20B)$$

$$\vec{C} = \frac{\vec{\beta} \times \hat{n}_o}{1 - \vec{\beta} \cdot \hat{n}_o} + \frac{r_m \vec{\beta} \times \hat{n}}{1 - \vec{\beta} \cdot \hat{n}} \quad (20C)$$

where T,R are the transmission and reflection coefficients across the foil,  $t',r'$  are the transmission and reflection coefficients inside the foil,  $r_m$  is the Fresnel coefficient of reflection for the mirror,  $\epsilon$  is the dielectric constant of the foil,  $\vec{\beta}$  is the beam line vector,  $\phi_{12}$  is the phase of light from interface 1 with respect to the particle fields at interface 2, and the n-direction vectors are shown in Figure 7. The interferometer analytic program designed by Rule et al. used the above basic equations to predict theoretical OTR patterns for clear foils. A finite optical bandwidth is built into the program and described in a later section.

At the time of this writing, Rule and Fiorito had not published a full description of their analytical solutions. On the other hand, a published development of the parallel component of intensity using a non-clear two-foil interferometer [Ref. 8] and notes used by Rule [Ref. 19] in his development of

the current clear two-foil interferometer computer code form the basis of the presentation here. The perpendicular component of the intensity is not presented but follows a similar development.

Rule and Fiorito's analysis uses Wartski's [Ref. 5] treatment of clear foil effects in a two-foil interferometer. Rule shows (using the basic equations developed by Wartski) that the parallel component of intensity per unit frequency interval could be approximated by restricting  $\vec{E} = \vec{E}_{\parallel}$  and  $\vec{\beta} = \vec{\beta}_{\parallel}$  in the plane of observation such that the clear foil parallel amplitudes from Figure 7 are approximated as:

$$\vec{A}_{\parallel} \approx \beta_{\parallel} (1 - T_{\parallel} e^{i\phi_{12}}) \frac{\sin \theta}{1 - \beta_{\parallel} \cos \theta} \quad (21A)$$

$$\vec{B}_{\parallel} \approx \beta_{\parallel} \frac{T_{\parallel}}{t'_{\parallel} \sqrt{\epsilon}} (1 - e^{-i\phi_{12}}) \frac{\sin \theta'}{1 - \sqrt{\epsilon} \beta_{\parallel} \cos \theta'} \quad (21B)$$

$$\vec{C}_{\parallel} \approx \beta_{\parallel} r_{m\parallel} \frac{\sin \theta}{1 - \beta_{\parallel} \cos \theta} + \frac{\beta_{\parallel} \cos \theta}{1 - \beta_{\parallel} \sin \theta} \quad (21C)$$

where  $\phi_{12}$  is again the phase of TR from interface 1 with respect to the electron field at interface 2 and noting that  $\phi_{12}$  and  $\phi_{23}$  are proportional to the  $k$  value, to yield the parallel component of the intensity per unit frequency per unit solid angle:

$$\frac{d^2 I}{d\omega d\Omega} = \frac{e^2}{4\pi^2 c} \left| r_{m\parallel} (\vec{A}_{\parallel} + \vec{B}_{\parallel}) e^{-i\phi_{23}} - \vec{C}_{\parallel} \right|^2 \quad (22)$$

Note that the parallel components in equations (21) and (22) of  $T, R, r', t'$ , and  $r_m$  are similarly defined as in the total values defined previously. Similar to the non-clear two-foil interferometer [Ref. 8], equation (22) is folded into a

Gaussian distribution of angle divergence given in equation (23):

$$f_{\text{gaussian}} = \frac{1}{\sqrt{2\pi\sigma_x^2}} \frac{1}{\sqrt{2\pi\sigma_y^2}} e^{\frac{-\alpha_x^2}{2\sigma_x^2}} e^{\frac{-\alpha_y^2}{2\sigma_y^2}} \quad (23)$$

where  $\sigma_x, \sigma_y$  are the RMS divergence in milliradians in the X,Y directions and  $\alpha_x, \alpha_y$  are the actual particle angle components such that these yield the average intensity per unit frequency per solid angle:

$$\frac{\bar{d}^2 \bar{I}}{d\omega d\Omega} = \int \frac{d^2 I_{\parallel}(\theta_x - \alpha_x, \theta_y - \alpha_y, \gamma_z)}{d\omega d\Omega} f_g(\alpha_x, \alpha_y, \gamma_z) d\alpha_x d\alpha_y d\gamma_z$$

where the moments of the distributions of the particles at the beam waist are defined as follows:

$$\sigma_x^2 = \langle \theta_x^2 \rangle, \sigma_y^2 = \langle \theta_y^2 \rangle, \text{ the RMS beam divergence} \\ \langle x^2 \rangle, \langle y^2 \rangle, \langle \gamma_z \rangle, \text{ the RMS beam radii measured in the X,Y directions.}$$

Note that  $\langle \gamma_z \rangle$  is the average electron energy. In order to incorporate a finite optical bandwidth, Rule [Ref. 19] averaged equation (24) over an assumed Lorentian shaped filter bandwidth profile given by equation (25):

$$F(k) = \frac{\Delta k}{2\pi} \frac{1}{(k - k_o)^2 + (\Delta k/2)^2}, \text{ where } k = 2\pi/\lambda \quad (25)$$

which when integrated with equation (24) yields the intensity per unit solid angle:

$$\frac{dI(\theta)}{d\Omega} \equiv \int_{-\infty}^{\infty} F(k) \frac{\bar{d}^2 \bar{I} dk}{d\omega(k) d\Omega} \quad (26)$$

Equations (20) to (26) form the basis for the analytical computer code which generates the theoretical OTR one-dimensional traces from the inputted

parameters of the data, which are: the foil spacing  $L$ , the transmission and reflection coefficients of the foil and the mirror ( $T, R, t', r', r_m$ ), the foil thickness, the energy of the electron beam (MeV), the filter bandwidth with central frequency  $\omega(k)$ , and the Gaussian divergence of the beam. The divergence is the only free parameter, which is used as the main fitting parameter for the data. The other inputted parameters of the experiment are varied only within their error bars. The code plots the theory OTR intensity patterns against the data OTR patterns for direct graphical comparisons of the fits. The data is stored in a digital or ASCII format, and the graphics program is GRAFPLUS to display the one-dimensional data and theory. The intensity peaks are normalized on the graphics display. The program stores the real values of the parallel component of the intensity, the perpendicular component of intensity, and the total intensity for display depending on the polarization of the beam and whether one is obtaining an emittance measurement or comparing coherence of different foils. Appendix A gives a description on the operation of the program using a data interface program, but the listing of the clear-foil interferometer OTR program is in the possession of Dr. Don W. Rule at Naval Surface Weapons Center, Silver Spring, Md. and use of the program can be obtained with his permission.

### III. EXPERIMENTAL PROCEDURE

The experimental procedure and setup for the two independent NPS linac emittance measurements and the coherence effects of differing thicknesses of clear foils is extensively described in Reid's thesis [Ref. 12]. The specific equipment involved in the emittance measurement is listed in Appendix A of Reid's thesis. All three experiments follow the same procedures, but differ in the type of Wartski interferometer and the data collection devices. In the past, emittance measurements required time intensive calculations and large, heavy equipment. Rule and Fiorito [Ref. 6-8] recently used the properties of optical transition radiation (OTR) as a means to determine the time resolved beam emittance and energy for even single beam pulses. This chapter describes an abridged version of the procedures for the application of OTR as a beam diagnostic to measure the emittance of the NPS linac.

Emittance measurements are made first by focusing the electron beam at a beam waist at the scattering foils and relating the local root mean square (rms) beam emittance to the rms beam radius and the calculated divergence according to equation (1). The procedures for the three experiments are similar; therefore, the procedure is discussed more in depth for the September 1990 emittance measurement relative to Reid's thesis, and the November 1990 coherence and emittance measurements follow the same procedure with minor equipment and technique changes. These experiments used the same equipment [Ref. 12] which consisted of a data acquisition capability, optical alignment tools, and control of the linac beam to produce X and Y waists to

measure the emittance. Moreover, the beam divergence was measured by observing the OTR patterns from the beam polarized at the waist.

The data acquisition device used for the beam emittance measurement was the Hamamatsu Silicon Intensified Target Camera (SITCAM) and a Compaq Portable II MSDOS computer installed with the Cross-Talk (XTALK) data conversion program [Ref.20]. In addition, a Hewlett-Packard 7475A X-Y Plotter was connected to the SITCAM to record the OTR scans from the camera for primarily the September 1990 data set and as a backup for the November 1990 experiment. The SITCAM consists of a highly light sensitive camera and a specialized control unit capable of time integration of the incoming signal and background noise subtraction. The control unit has the capability to perform one and two dimensional scans of the captured image intensity recorded by pixel location. For these experiments, the one dimensional scans were used. The OTR is generated by placing a Wartski interferometer, consisting of a clear foil and a mirror separated by a vacuum spacing, at an angle of 45 degrees to the beam line. The clear foil is the front foil generating OTR from the front and back foil surfaces. These OTR amplitudes interfere coherently with the backward OTR from the mirror given by equation (20) and shown in Figure 7 in chapter II. The spacing between the foils was vacuum, and the foil spacing was chosen to correspond to the bandwidth of the selected OTR for observation by using equation (27):

$$\lambda = \frac{2\pi L}{\beta\phi}(1 - \beta \cos \theta) \quad (27)$$

and to be the same order of magnitude as the radiation formation zone,  $L_V$  (see equation (8)). The interferometer spacing is directly related to the number of

visible fringes in the OTR pattern. As the width of the foil spacing approaches  $L_V$ , the OTR pattern yields more fringes, and, consequently, greater sensitivity to the beam divergence [Ref. 5].

The optical devices and alignments are detailed in Reid's thesis [Ref. 12], but the following sections provide an overview of these procedures. The procedures for the September 1990 emittance measurements and the November 1990 experiments are very similar, but the November 1990 emittance measurement represents a refinement in the accuracy of the measurements due to greater familiarity with the equipment and lessons learned from the September experiment.

#### **A. EXPERIMENTAL SETUP**

The setup for the emittance measurements consisted of assembling and positioning the optics on a Newport Optical table designed to permit accurate alignment of the optics in mounting holes, the assembly of the interferometer in the OTR chamber, and the installation of data acquisition equipment in the control station.

The Newport Optical table was positioned parallel to the beam line in order to support observation of the beam profile (another experiment) in the main scattering chamber and the radiation from the OTR chamber simultaneously. The optical positioning consisted of first determining the preferred path of the electron beam and causing the alignment laser to bounce off a mirror (on a rotation station positioned at 45 degrees) in the main

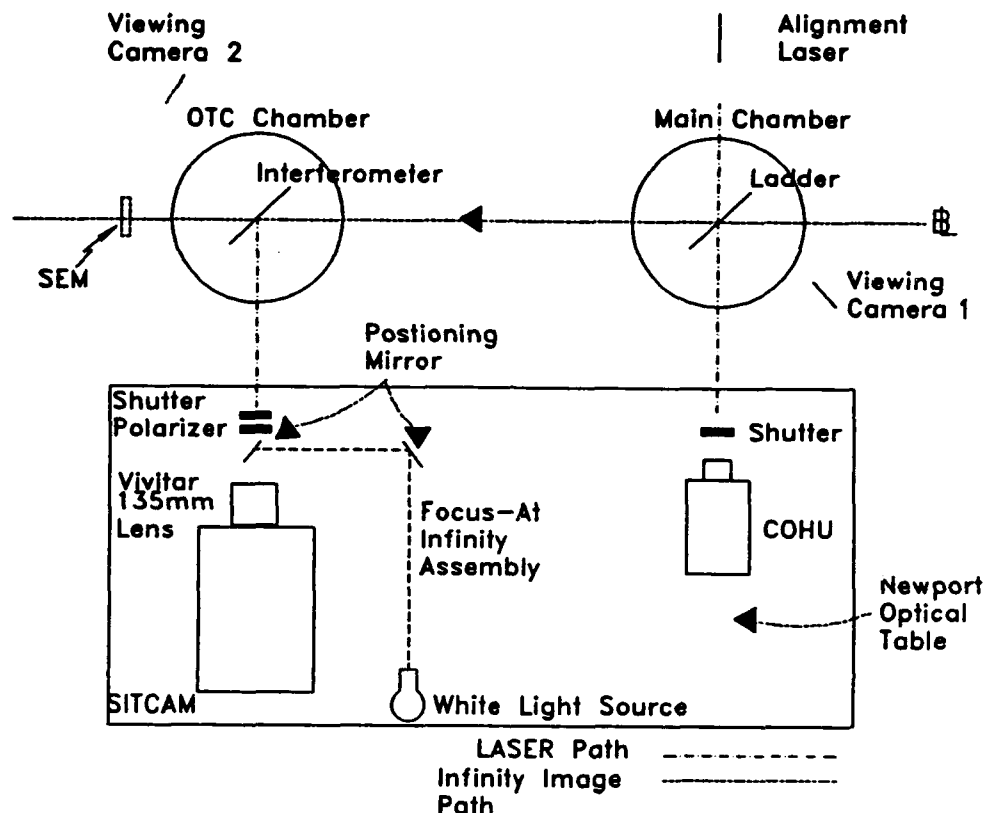


**Figure 8: Equipment Setup.** A Newport Optical Table is positioned parallel to the beamline. The SITCAM is positioned on the left side of the table to measure the emittance from the OTR chamber. The focus-at-infinity device is outboard of the SITCAM on an optical rail parallel to the SITCAM. Camera 1 was focused on the target ladder and Camera 2 was focused on the SEM.

scattering chamber and follow the beam path into the OTR chamber (see Figure 8). Convinced of the co-linearity, the alignment of the Newport Optical table was made by bouncing the alignment laser light off a mirror positioned at 45 degrees in the OTR chamber and exiting out the perpendicular port (with reference to the beam line) of the chamber (see Figure 8). Two optical posts were aligned along the exiting laser path and were positioned in mounting holes in the table. Once the table was aligned, the SITCAM was positioned facing the perpendicular port of the OTR chamber as shown in Figure 8. A focus-at-infinity apparatus was placed on an optical rail outboard and parallel to the SITCAM next to the angular calibration device for the camera. The focus-at-infinity device consisted of a rail raised to the beam height determined by the alignment laser and a standard white light source projecting through a neutral density (ND 4) filter through an aperture to a sector star target. The sector star image was focused by a two-inch diameter 20 mm focal length lens at the infinity focal plane and projected by positioned mirrors onto the lens of the SITCAM. The sector star consisted of a radial array of alternating opaque and transparent rays. The image plane focus assembly was simpler, and consisted of a grid target positioned at the same distance from the SITCAM as the center of the OTR chamber which holds the interferometer. These two devices permitted calibration of the SITCAM with the Vivitar 135 mm lens which was positioned on a remotely controlled vernier slide in front of the SITCAM. Just prior to the start of the measurements, an electronic shutter and a polarizer were positioned as needed to capture both the polarized and unpolarized OTR patterns.

The OTR chamber was installed along the beam line (see Figure 8) on a lab jack strong enough to support the weight. A target grid the size of the interferometer pellicle was mounted on a mirror pellicle to find the beam line located on the pellicle by bouncing the alignment laser off the mirror ( located on the target ladder) oriented 45 degrees from the beam line in the main scattering chamber down to the OTR chamber. The OTR chamber was adjusted until the laser light impinged the center of the target grid. Once the chamber and the SITCAM were aligned, the Wartski interferometer for the experiment was installed in the OTR chamber. The interferometer was oriented 45 degrees from the beam line for observation of the forward OTR from the front foil and the backward OTR from the mirror. The interferometer foil spacing was determined based on an order of magnitude of the formation zone in a vacuum and the observation bandwidth given by equation (27).

The data acquisition devices were placed in the control station of the NPS linear accelerator. The NPS linear accelerator is a product of 1960's technology and is primarily designed for radiation and nuclear structure studies. The linac is a three stage, pulsed, S-band RF accelerator with an energy from 20-100 MeV and average currents of about 0.5 microampere. The beam pulse duration is about one microsecond and the pulse repetition rate is 60 Hz. Simply described, electrons, generated by an electron gun similar to a TV, are accelerated by riding an RF wave through three stages of acceleration. Once accelerated, the electron beam is deflected by magnets into the main scattering chamber as shown in Figure 9. The control room has the control equipment for the acceleration of the electrons and to steer the beam into the target areas. The data acquisition equipment was installed in

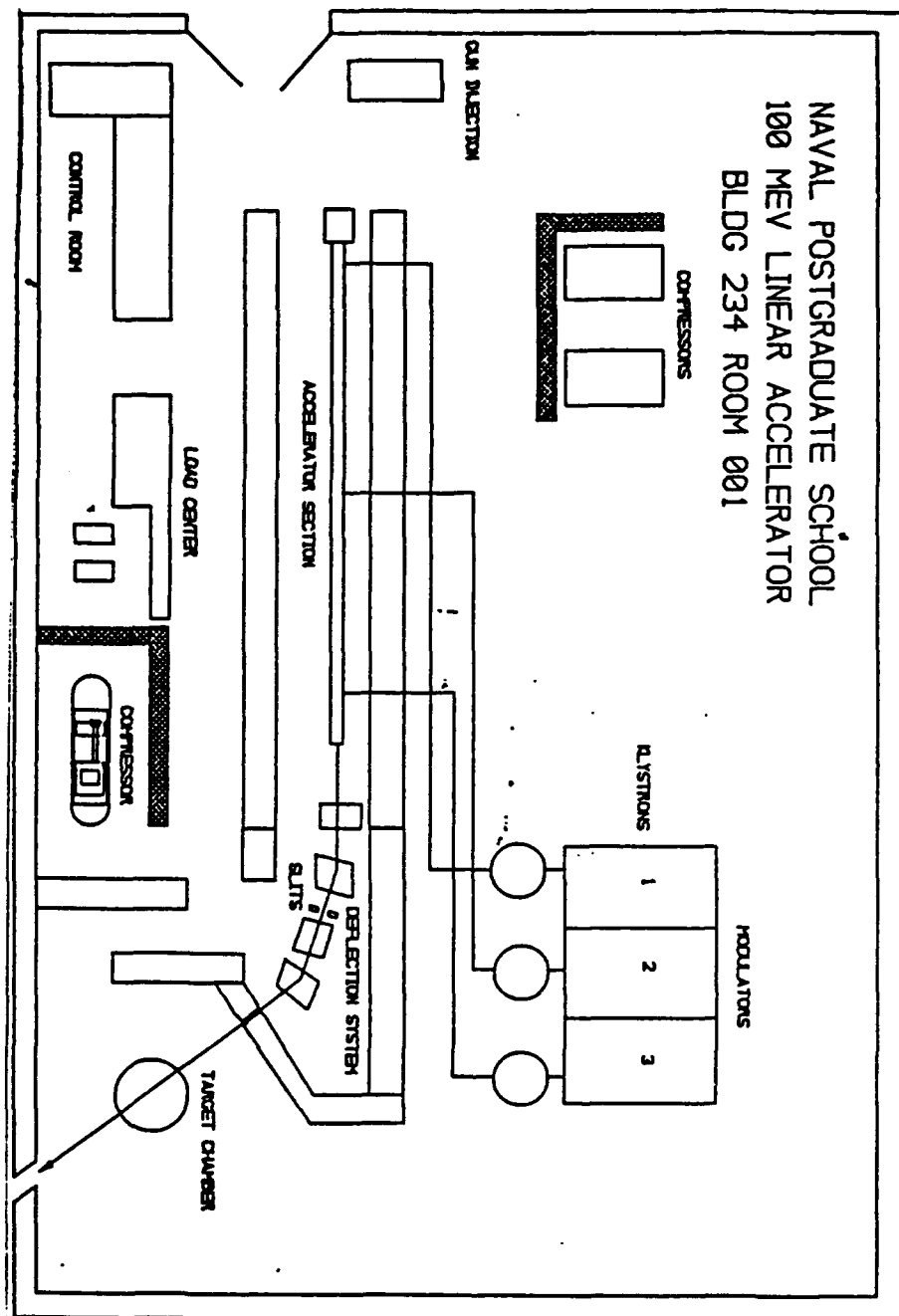


**Figure 9: Linear Accelerator equipment layout.**

the control room and included the SITCAM controller (which has the image capture and integration capability), the Hewlett-Packard 7475A X-Y plotter, the Compaq II computer installed with the XTALK data conversion program, a video recorder for live imaging, polaroid cameras for still photos, remote monitors for reading the Secondary Emission Monitor (SEM) and the camera images. Oriel Mike Encoders, model 18011, were used to remotely control the translation of the 135 mm lens between the image and infinity focal planes and to perform the angular calibration. Finally, the target ladder controls were located at the linac operation panel, and a step motor remotely controlled the rotation of the ladder in the main scattering chamber.

## **B. ALIGNMENT OF THE SITCAM**

Alignment of the SITCAM was a two-man iterative process after the initial setup. First, the laser beam was used to align the SITCAM without the 135 mm lens in place. The SITCAM was positioned on an optical rail by means of an attached jack with translational and vertical vernier controls and adjusted until the laser impinged the center of the lens cap covering the light sensitive lens (the rail was bolted into position in the mounting holes previously determined by the optical posts used in the alignment of the table). The 135 mm lens was then installed on the rail using a remotely controlled vernier slide with a lens holder. The lens was levelled and then adjusted so that the laser struck the center of the 135 mm lens cap (installed with a target grid). Then, the lens cap was removed, and an iterative process was used to align the lens to strike both the center of the 135 mm lens cap and the center of the SITCAM optical sensor cap without the 135 mm lens cap.

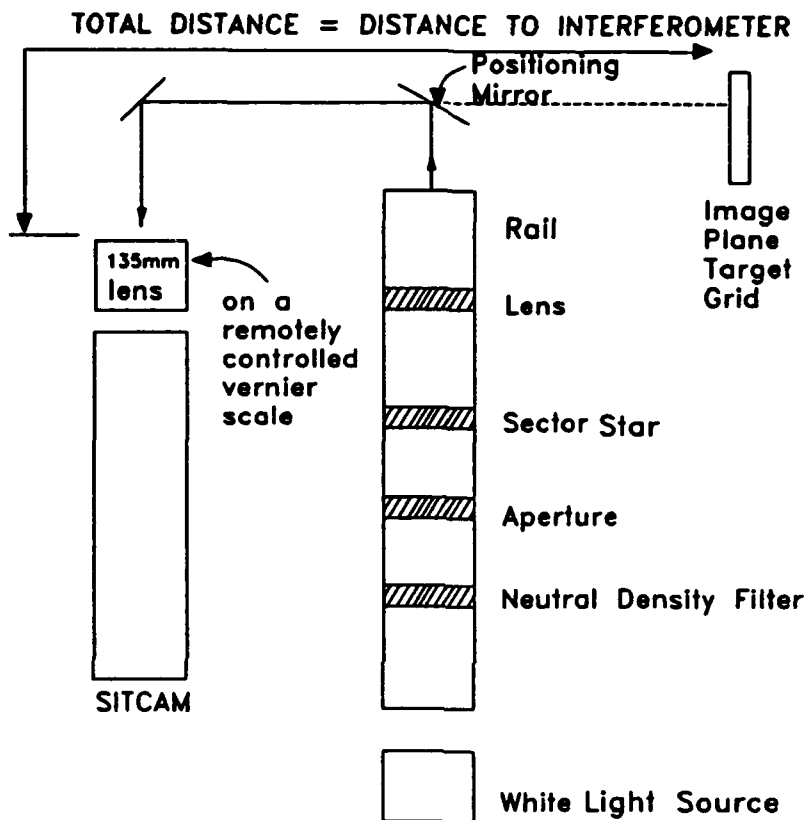


**Figure 10: Focus-at-infinity and image plane assembly. This assembly was used to establish the focal plane. The white light projected the sector star image into the camera lens. Neutral density filters prevented saturation. The target grid was positioned the same distance from the SITCAM as the OTR interferometer to determine the image plane.**

The focal plane was established by using the focus-at-infinity assembly. Using an ND 4 neutral density filter to assure that the camera was not saturated, the sector star image was focused at infinity by covering the bottom half of the sector star with black construction paper (exposing the top half to the light source) and focusing the top half of the sector star back through the 20 mm lens onto the bottom half of the star target by sliding the sector star back and forth on the rail. Figure 10 shows the position of all the elements of the focal plane devices for the SITCAM. The lights were then turned off, and the SITCAM was turned on. Adjustments were made by remotely translating the 135 mm lens to bring the sector star into focus by using a remote monitor connected to the SITCAM. Once focused, as shown in Figure 11, the position



**Figure 11: Sector Star image seen at infinity by the SITCAM.  
For a fuller description of the procedure, see Ref. 12.**

was recorded both locally on the vernier scale and remotely on the Oriel encoder. To establish the image plane, the mirror, shown in Figure 10, blocking the target grid was removed, and the target grid was placed 28.5 inches away

from the SITCAM lens. Using a controlled low light source shined on the grid, the other lights were turned off and the SITCAM was turned on. Again the 135 mm lens was translated to the image plane remotely until the grid was focused on the SITCAM's remote monitor. The positions were recorded, and the traverse distance from the focal plane to the image plane was ~1.4 inches.

### C. ANGULAR AND DISTANCE CALIBRATION

The next step was to calibrate the optical devices using the computer pixel locations corresponding to angle and distance. These included a step motor calibration for angular measurements and a target grid calibration for traverse distance measurements. Detailed descriptions of these procedures are found in Reid's thesis [Ref. 12], but the following provides a brief synopsis. Calibrating the Oriel Encoder was accomplished by comparing the relative digital number outputs of the controller to the actual distance travelled on the associated vernier scales. For the horizontal angular calibration of the SITCAM, the scattering chamber mirror (located on the target ladder) was rotated in steps of twenty, and the laser scanned the SITCAM lens from left to right and back again taking into account the backlash of the stepper motor. The pixel position was recorded at each interval in both directions; the lens scans were plotted, and the straight curve slope of 1.41 steps per pixel [Ref. 12] converted to an angular calibration of 0.304 milliradians per pixel. The vertical calibration was similarly performed [Ref. 12] and resulted in 0.290 milliradians per pixel.

The number of pixels per millimeter in the horizontal and vertical directions were determined using the image plane target grid made of graph paper captured by the SITCAM. The change in the number of pixels across

ten grid squares was recorded. The average horizontal and vertical distance calibrations were 7.37 pixels/millimeter and 10.2 pixels/millimeter respectively. The overall magnification was 1.92:1 [Ref. 12].

#### **D. THE EMITTANCE MEASUREMENT: SEPTEMBER 1990**

The procedures for recording the emittance measurements for both the September and November 1990 experiments are virtually the same, but differ in the type of Wartski interferometer utilized and in the increased accuracy of the November data set due to the learning experience from September. Reid [Ref. 12] provides a detailed description of the procedure and the associated impediments. For both experiments, the calibrations were identical, because the apparatus from September was left in place and used in November. The following provides a brief description of the procedure with some clarification on key points and lessons learned.

The September 1990 experiment used a Wartski interferometer consisting of a Kapton foil (3/10000 of an inch thick) and a front-surfaced silicon polished mirror with a inter-foil spacing of .325 inches or 0.825 cm. Since the interferometer was oriented at 45 degrees to the beam line, the effective foil spacing was 1.167 cm. This foil spacing,  $L$ , was chosen to be the same order of magnitude as the radiation formation zone in a vacuum,  $L_V$ . Beam energy was 92.58 MeV.

Verification of the coincidence of the alignment laser beam and the electron beam was made with the remote camera 1 (see Figure 8) and a phosphorous screen on the target ladder. In the September experiment, the image plane was observed on the SITCAM to be displaced [Ref. 12], and the electron beam tended to be locationally unstable at the laser beam position and

to stabilize at a different location. To correct this problem, the laser was aligned to follow the preferred path of the electron beam, and all the optics were realigned accordingly. After checking the alignment, the SITCAM was positioned at the image plane to capture the beam waist intensity profiles. The captured profiles looked normal, and the SITCAM was repositioned at the infinity focal plane to capture the polarized OTR patterns. The resulting OTR pattern was flat and spread out due to the electron beam energy spread, but the image pattern was focused when an interference filter was positioned between the SITCAM and the 135 mm lens. Reid [Ref. 12] details some other minor problems such as the change in the effective optical distance due to the introduction of the filter and the consequent solutions.

Measuring the beam emittance is done by capturing the OTR pattern caused by an electron beam incident on the interferometer, focused at the X or Y-waists. The SITCAM is first placed at the image plane, and the beam is focused at the X-waist as shown in Figure 12. The intensity profile of the X-waist is recorded on the X-Y plotter and in turn digitized for analysis in the computer code. The SITCAM is then repositioned at the infinity focal plane and the polarizer is placed in front of the camera in a horizontal configuration. Figure 13 shows the horizontal polarization, horizontal scan of the X-waist OTR pattern. Although Figure 13 shows a relatively clear pattern, initial OTR patterns exhibited secondary flares due to lens and filter reflections and the two component nature of the unsynchronized beam pulse from the accelerator [Ref.12]. These problems were corrected by masking off the reflected images and by closing the energy slits to an energy spread of 0.125% (in line with the 1971 energy calibration) respectively [Ref. 12]. Finally, the polarizer didn't



Figure 12: Beam focused at the X-waist for determining beam size for the emittance calculation.

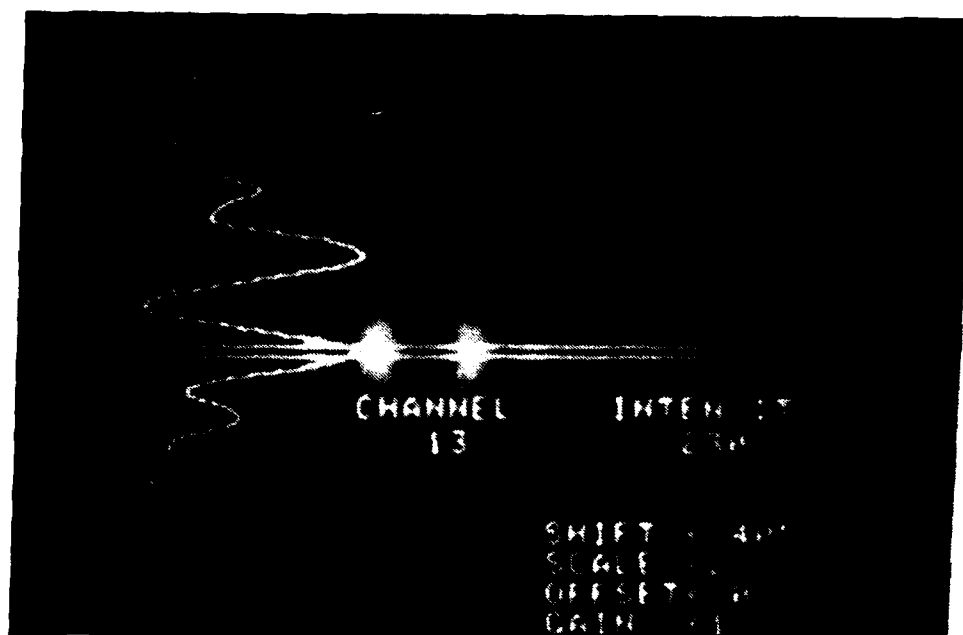


Figure 13: X-waist at the focal plane, horizontal polarization, horizontal scan used for divergence in the emittance measurement.

allow enough photons to pass through to the camera for a clear image using a 595-605 nm filter; therefore, a blue Corning filter 428x100 nm was installed resulting in Figures 12 and 13. Figure 12 was analyzed to provide the RMS beam radius, and Figure 13 was analyzed to determine the divergence for the emittance measurement in accordance with equation (1). Using the X-waist scan in Figure 13 as an example, the scan was recorded on the Hewlett-Packard X-Y plotter and digitized by hand at the Naval Surface Weapons Center in Silver Spring, Md. The digitized files were input into Rule's clear foil analytic code and compared to theory based on the aforementioned foil spacing, foil thickness, bandpass filter, indices of refraction for both the foil and the mirror, and a free parameter of electron beam divergence. The results of the investigation are in Chapter IV. The Y-waist images are obtained similarly and are presented in the analysis.

In the September 1990 experiment, transition radiation served to maximize the quality of the electron beam, and demonstrated the utility of OTR to solve beam diagnostic problems. Reid's thesis [Ref. 12] describes the detailed procedure and should be used as the source for optical alignment, erratic beam disturbances, and beam energy information.

#### **E. COHERENCE, EMITTANCE MEASUREMENTS: NOV. 1990**

The November 1990 experiment used the same experimental procedures for alignment and capturing OTR images as the September 1990 data set with one exception. First, the calibration data for the November data set was exactly the same as the September experiment, because the apparatus was not dismantled in the interim. The exception was that the data acquisition utilized the HP X-Y plotter as a backup, and primarily converted the data to an ASCII

format using the XTALK program installed in the Compaq II computer. These ASCII files were inputted into Rule's clear foil analytic code for comparison against the theoretically derived OTR patterns. The November 1990 experiment started by investigating the coherence effects of differing thicknesses of clear foils. The different foil thicknesses served to show the sensitivity of the interferometer to changes in medium (foil) thickness and input parameters to the code such as the foil refractive index. In addition, the measurements served to validate the theoretical premise and calculations in Rule's clear foil interferometer computer code. The two thicknesses of foil were  $.5\mu\text{m}$  and  $5\mu\text{m}$  of nitrocellulose with a broadband index of refraction of 1.5 [Ref. 21]. The interferometer consisted of one of these nitrocellulose thicknesses and a front-surfaced aluminum mirror with an effective foil spacing of  $.523\text{ cm}$ . The beam energy was  $91.36\text{ MeV}$ . The optical alignments and the procedure for imaging were the same as outlined previously in the September experiment. The SITCAM operation consisted of the following procedure for capturing the image:

1. Focus the image at the focal plane.
2. Capture the image and integrate the intensity.
3. Close the SITCAM shutter and subtract background.
4. Scan the image in one-dimension.
5. Plot on the X-Y plotter.
6. Run the XTALK program and store in an ASCII file.

The beam was steered using machine steering after the first accelerator section (10 ft. steering) so that the beam went through the center of the end station focusing quadrupoles. The SITCAM was positioned at the infinity

image plane, and the polarizer was removed from the SITCAM setup. The first foil used was the 0.5  $\mu\text{m}$  thickness, and three unpolarized images were captured using interference filters of 455x10 nm, 455x50 nm, and 650x70 nm respectively. Vertical and horizontal scans were taken on each captured image. Next, the beam was shutdown, and the interferometer replaced with a 5  $\mu\text{m}$  nitrocellulose foil. After vacuum was established, the beam was re-established before, and three images were captured using the same beam energy and the aforementioned set of filters. Figure 14 shows the captured unpolarized image with the 5  $\mu\text{m}$  foil thickness and the resulting horizontal scan of the image intensity (the filter was the 455x50 nm bandpass). The other scans were stored as ASCII files and compared to theory in Rule's computer code. These scans are discussed in Chapter IV.

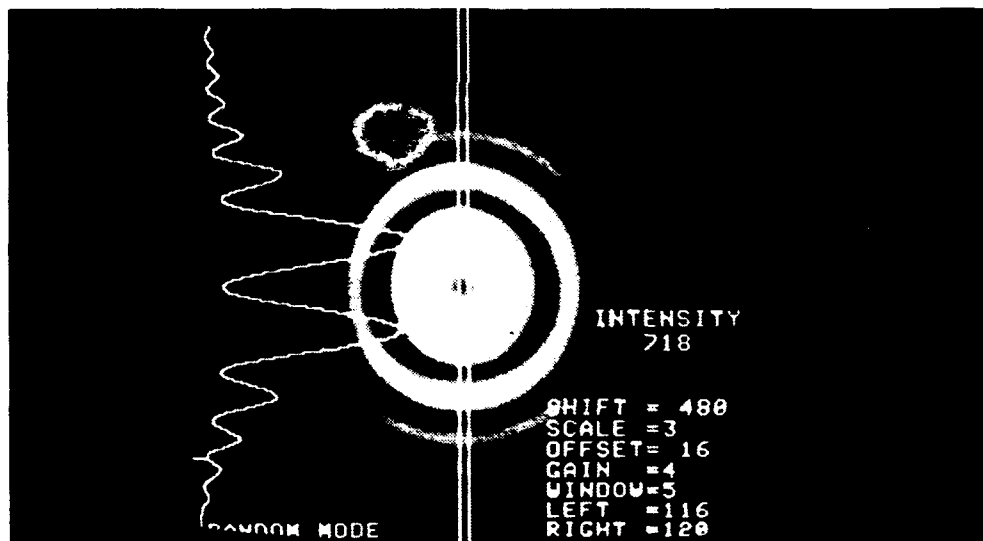


**Figure 14: Horizontal intensity scan of the 5  $\mu\text{m}$  foil thickness with a 455x50 nm filter unpolarized OTR image.**

Using the information obtained from the foil sensitivity measurements, the emittance measurement was accomplished. The SITCAM was positioned at

the image plane; the polarizer was reinstalled, and the beam was established at an X-waist shown in Figure 15. Due to more careful, accurate alignments and experimental experience, the beam was positioned at a true X-waist, and, consequently, when the SITCAM was repositioned at the focal plane, the horizontally polarized, horizontal intensity scan yielded good fringe visibility with the absence of undetermined asymmetries and eventually a better measurement of the divergence. For clarification, the emittance measurement used the 5  $\mu\text{m}$  nitrocellulose foil interferometer and the 455x50 nm filter bandwidth. The foil index of refraction was determined from the foil coherence effects measurements described in Chapter IV. Similarly, the Y-waist was established, and the vertically polarized vertical intensity scans were captured, stored in ASCII files, and analyzed. Discussion of these OTR images and the resulting measurements are in the following chapter and are the main objective of this thesis.



**Figure 15: X-waist beam spot for the beam radius measurement of the nitrocellulose clear foil interferometer emittance measurement. The smaller wings are due to reflection, and are mathematically removed in the analysis.**

## **IV. EMITTANCE MEASUREMENT AND DATA ANALYSIS**

### **A. INTRODUCTORY REMARKS**

The data analysis presented in this paper is a graphical comparison of the captured OTR intensity patterns from the installed interferometer to the theoretical OTR patterns calculated by the analytic computer code developed by Don Rule et al. from published theory primarily based on Wartski's dissertation. The chapter is divided into three sections consisting of the Kapton foil interferometer emittance measurement of the electron beam, the nitrocellulose clear foil interferometer coherence effects, and the nitrocellulose interferometer emittance measurement. Appendix A offers a detailed step-by-step description of the interface subroutine with Rule's analytic clear foil program, but details on the algorithms associated with the program must be addressed to Dr. Donald W. Rule, Naval Surface Weapons Center, Silver Spring Md. The analysis validates the computer code, but does suggest some improvements to increase the accuracy of the measurement especially in the area of filter modelling. Fitting the data to the theory presented some anomalies which are discussed, but the divergence used in the emittance measurement was the free parameter. The presentation is chronologically organized with a summary of conclusions and a comparison of the emittance of the NPS linac with other similarly designed particle accelerators.

### **B. EMITTANCE MEASUREMENT: KAPTON FOIL**

From the calibration of the optical equipment, the angular conversion was  $3.04\text{E-}4$  radians/pixel, which was twice the measurement calculated in Reid's

thesis [Ref. 12], because the angle of reflection off the alignment mirror was not previously properly taken into account geometrically. In addition, the x-direction calibration and the y-direction calibration yielded 0.136 mm/pixel and 0.100 mm/pixel respectively. The Wartski interferometer consisted of the Kapton foil (3/10,000 of an inch thick) and a silicon polished mirror (refractive index of  $n=0.818$  and attenuation index of  $K=6.150$  [Ref. 22]) with an effective foil spacing,  $L$ , of 1.167 cm parallel to the beam line. With the interferometer oriented at 45 degrees to the beam line, the effective foil thickness converted to  $1.08E-3$  cm, and the index of refraction was 1.823 in the bandwidth of the blue Corning filter, 4820-5700 Å. The energy of the beam was  $92.58 \pm 0.1$  MeV. The emittance measurements for the September 1990 data were recorded on the X-Y plotter and digitized in files as documented in Chapter III. The above calibration parameters and the data parameters were inputted into Rule's computer code using the procedure described in Appendix A. The divergence was varied until the data correlated with the theoretical OTR pattern. The graphs presented herein are the correlations of the data with the theory. The vertical scale intensities are normalized for comparison purposes for both the data and the theory. For purposes of clarification, the graphical representation of the experimental OTR patterns are drawn by a solid line (—) and the theoretical OTR patterns are drawn by a dashed line (---) for all data sets in this thesis.

The Kapton foil emittance measurements have many anomalies in the data due to the pioneering aspects of the procedure, and should be viewed as a rough, first cut approximation to the emittance. With the exception of energy (which was very accurately measured), the Kapton foil did not exhibit

sensitivity to small changes (within error margins) to the foil thickness, the foil spacing, the indices of refraction, and the filter bandwidth due probably to the large foil thickness (the foil thickness was greater than the radiation coherence length as described in Part C) and the approximation of the Corning filter to a Lorentzian filter shape. The data and the theoretical OTR patterns are presented together for correlation using the center minimum of the patterns as the reference point (GRAFPLUS is the plotting program incorporated into the code and is explained in Appendix A).

Figure 12 in Chapter III shows a photo of the X-waist beam spot image for the Kapton foil. Using a root mean square (RMS) subroutine interfaced with the computer code, Figure 16 is generated plotting the X-waist beam intensity profile for a horizontal scan with the intensity normalized to the peak intensity, and calculates the RMS beam radius to be 1.65 mm. Note that the beam X-waist focus is not symmetric, and suggests that the beam is not fully at the X-waist. This particular phenomena seems to bear out, and is consistent throughout the data set. In fact, Figure 17 shows a photo of the vertically polarized, horizontal scan of the perpendicular component of intensity (IPERP) of the X-waist OTR pattern, and Figure 18 displays the data against the theoretically generated IPERP for the same input conditions. Figure 18 demonstrates that the IPERP data cannot be fit to the theory, and the presence of fringes suggests that the beam is not focused at the X-waist or the SITCAM is misaligned with respect to the outgoing OTR. The SITCAM misalignment is best described by the fact that the intensity scan is not performed at the center of the polarized OTR pattern ( the dark center area). Normally, IPERP is used as a consistency check against the parallel component of intensity (IPAR) for

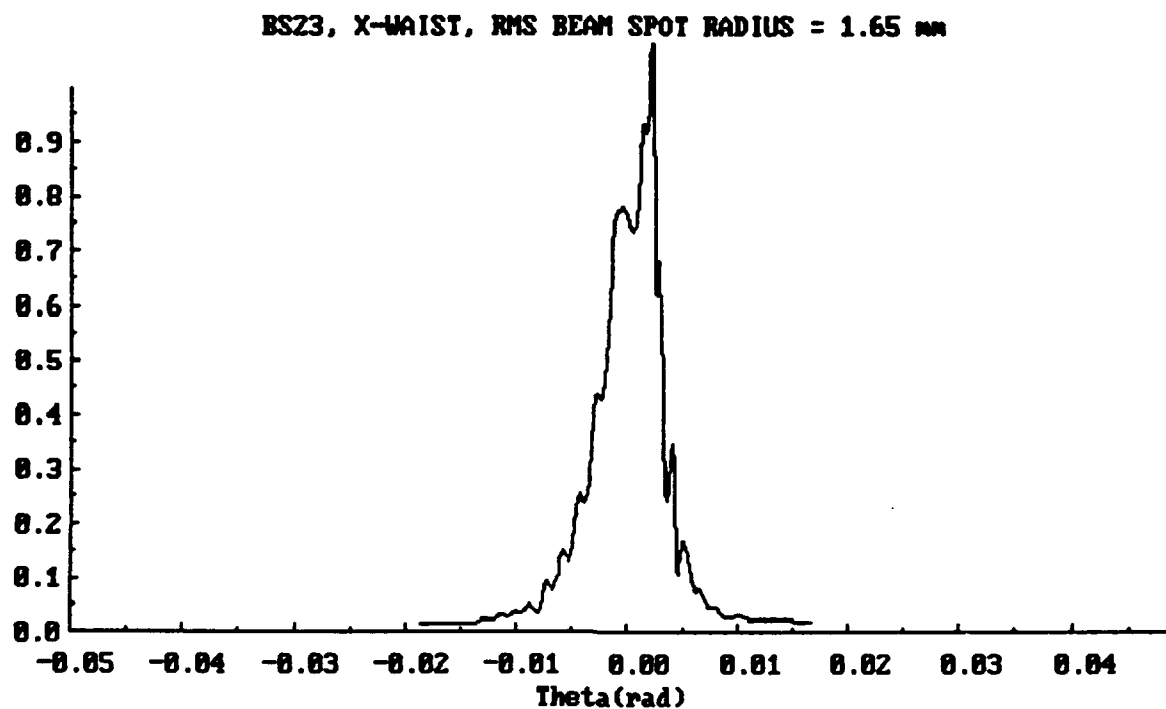


**Figure 16: X-waist beam spot intensity image for the Kapton foil. The horizontal scan is used to calculate the RMS beam spot radius, which is 1.65 mm.**



**Figure 17:** Photo of the X-waist IPERP horizontal scan. Note the fringe visibility denoting that the SITCAM is not scanning at the center of the X-waist.

BS24, X-WAIST, UP, HS, IPERP, DIV.=1.0 mrad

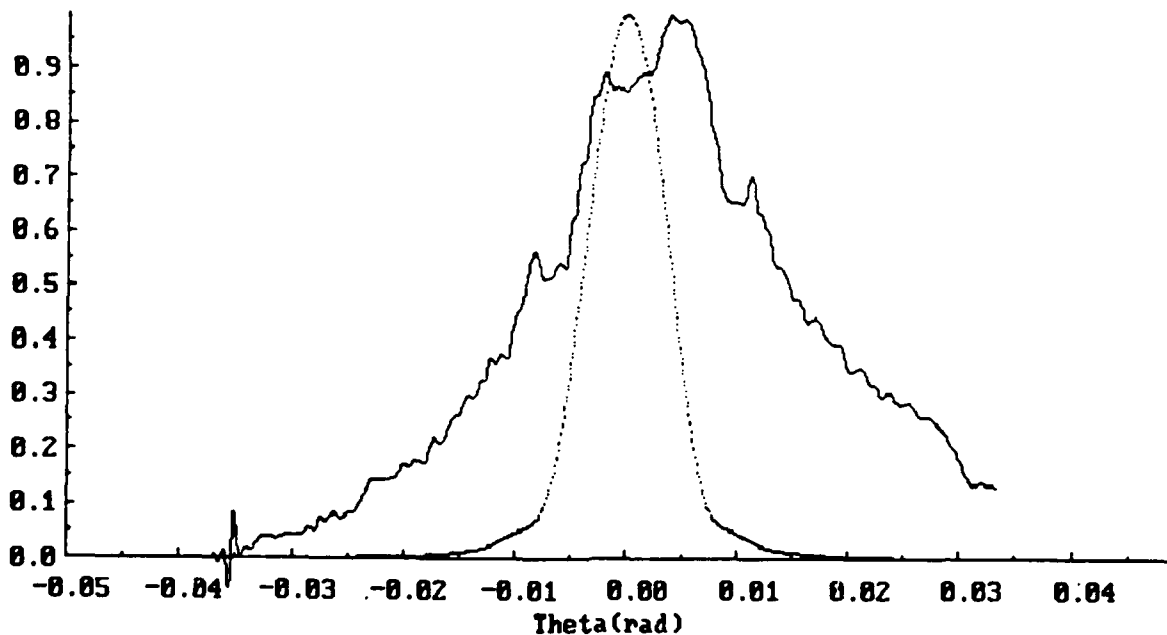


**Figure 18:** The theoretical X-waist vertically polarized, horizontal scan does not correlate with the data indicating that the scan is not at the center of the X-waist.

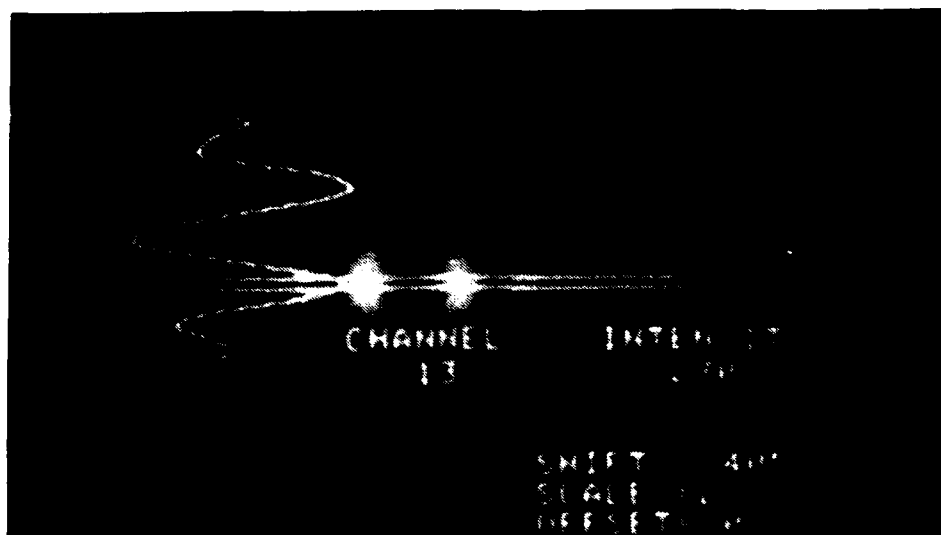


**Figure 19: The X-waist horizontally polarized, horizontal scan of the Kapton foil OTR pattern used for the divergence measurement.**

the correct divergence measurement. IPAR incorporates equations (20) and (26) described in Chapter II into the computer code algorithm. For the X-waist emittance measurement, the divergence,  $\theta_x$ , is determined from the comparison of the horizontally polarized, horizontal scan of IPAR compared to the theoretically generated IPAR for the same previously described input conditions. Figure 19 shows the photo of the OTR pattern of the horizontally polarized, horizontal scan, and Figures 20A, 20B, and 20C show the graphical comparisons to the theoretically generated OTR patterns for divergences of 1.0, 0.7, and 1.3 milliradians respectively. In Figure 20A, the divergence fits the rightside of the data with respect to fringe visibility and contour to the theoretically generated OTR pattern. The leftside exhibits some asymmetry, but, from Figure 18, this phenomena is due probably to the fact that the scan is not done at the geometric center of the X-waist and the fact that the X-waist focus is not obtained. The cutoffs abruptly at -0.035 and 0.027 radians is due to

BS25, X-WAIST, HP, HS, IPAR, DIV.=1.0 mrad

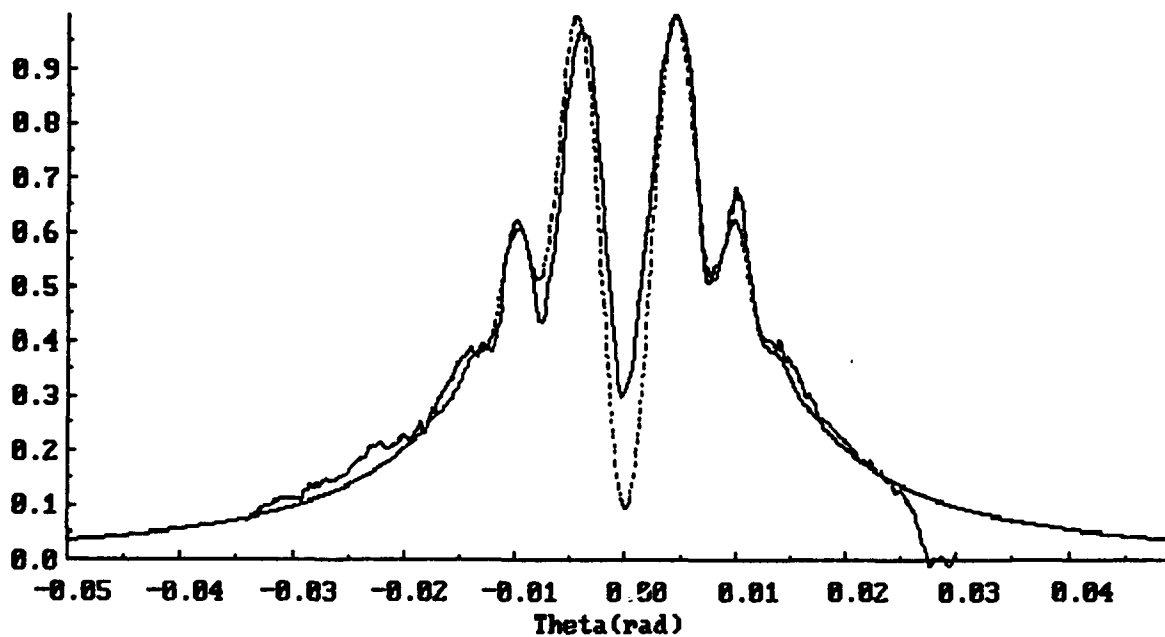


**Figure 20A: Kapton foil divergence measurement at the X-waist horizontal polarization, horizontal scan of the OTR. The IPAR intensity plot gives a good correlation at 1.0 mrad. Note: the rightside of the data is the better correlation with the exception of the second fringe intensity.**

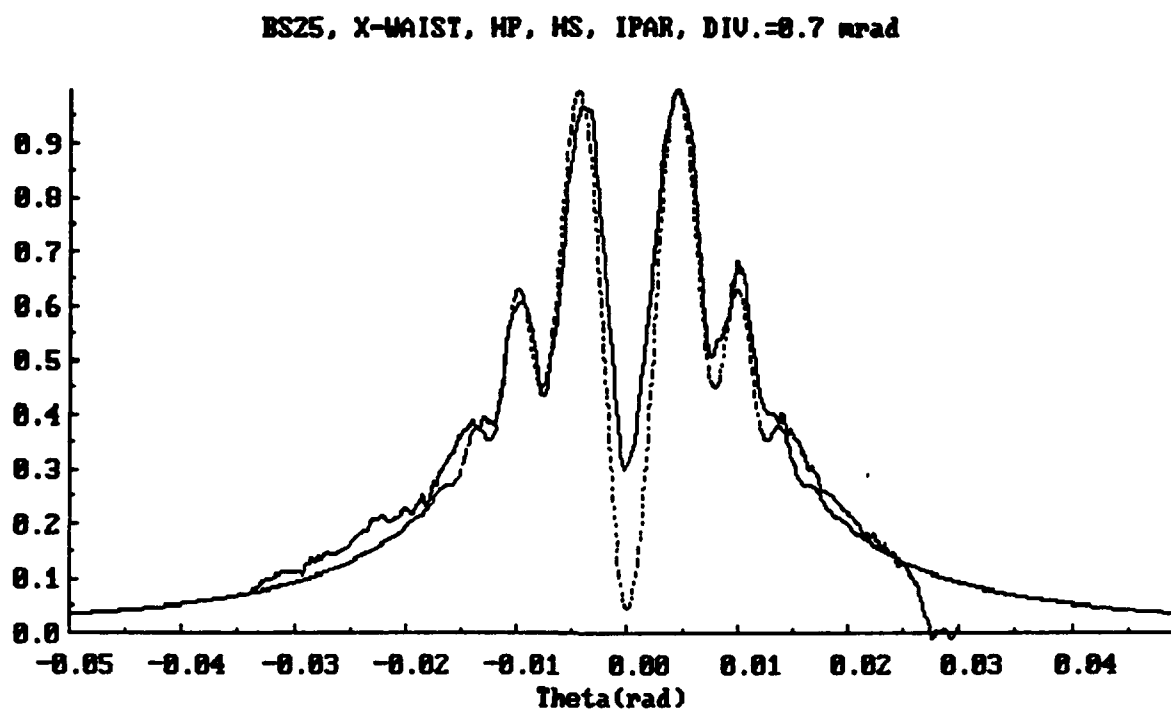


**Figure 20B: Kapton foil, X-waist horizontal polarization, horizontal scan with a divergence of 0.7 mrad.**

BS25, X-WAIST, HP, HS, IPAR, DIV.=1.3 mrad

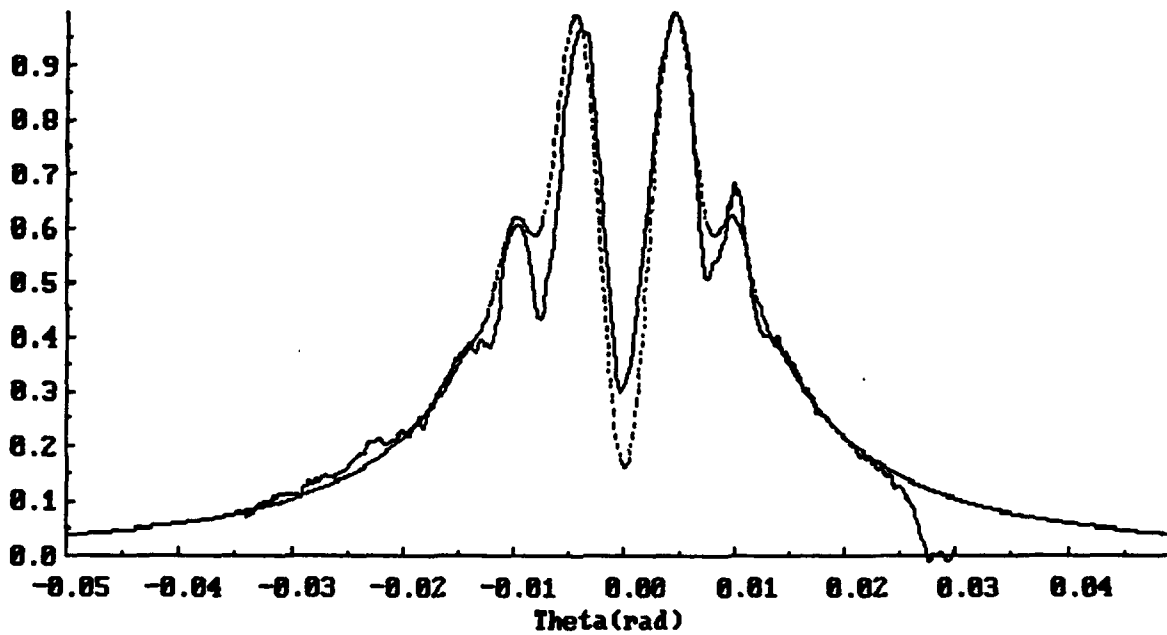


**Figure 20C: Kapton foil, X-waist horizontal polarization, horizontal scan with a 1.3 mrad divergence. Note the poor fringe visibility.**

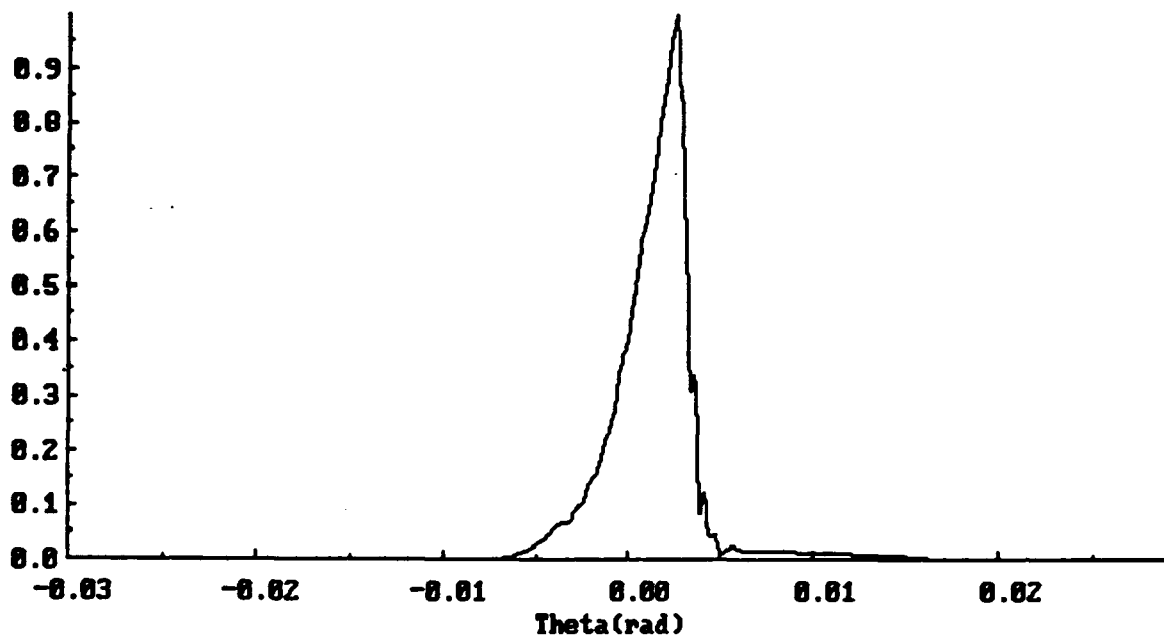
the SITCAM alignment and the reflection masking. Figure 20A uses a 1.0 milliradian divergence to obtain the data correlation for the X-waist, and, using Figures 20A and 20B in the error analysis, the x-divergence,  $\theta_x$ , is 1.0 milliradian. Figure 20B fits the data on the leftside with good fringe visibility, but the contour matching is poor for the inputted divergence of 0.7 milliradians (mrad). Figure 20C shows good contour matching of the data, but very poor fringe visibility for the inputted divergence of 1.3 mrad. Consequently, the input parameters for the x-emittance are the RMS beam radius of  $1.65 \pm 0.1$  mm (error based on a small change in the geometric center of  $\pm 1$  pixel) and a divergence of  $1.0 \pm 0.3$  mrad.



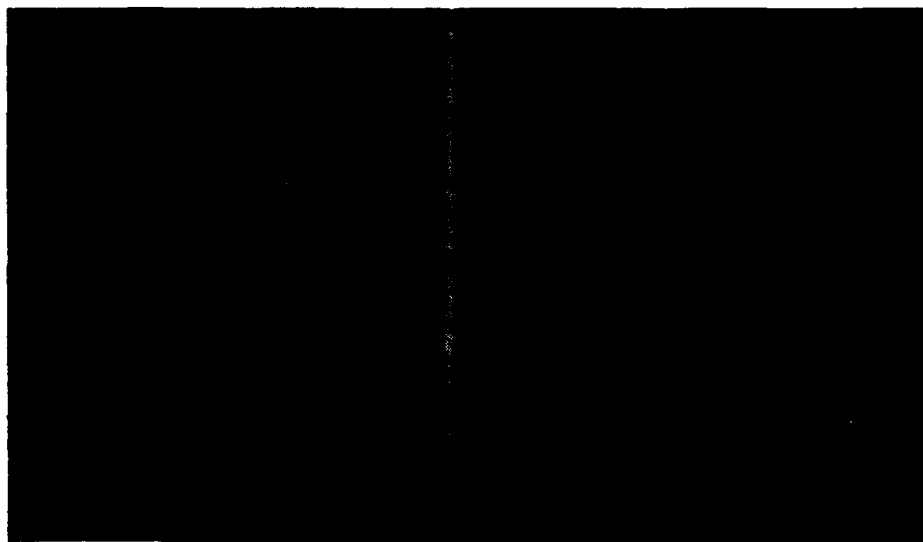
**Figure 21: The Y-waist beam image and intensity scan.**

Figure 21 shows a photo of the Y-waist beam spot image focus from the SITCAM, and Figure 22 is the plot of the vertically scanned intensity of the beam spot which yields the RMS beam radius for the emittance measurement in the vertical direction. The RMS beam spot Y-radius is  $0.89 \pm 0.1$  mm based

BS19, Y-WAIST, RMS BEAM RADIUS= .890 mm



**Figure 22:** An intensity plot of the Y-waist beam spot. The RMS beam spot radius is 0.89 mm.



**Figure 23:** The Y-waist vertically polarized, vertical scan of the IPAR intensity. Note the flare in the right side of the data caused by an improper focus or alignment.

on the y-direction calibration of 0.100 mm/pixel. It is again important to note that the beam shows an asymmetry in the intensity, which suggests that the beam is not focused at the Y-waist exactly. The Y-waist horizontal polarization, vertical scan of the IPERP intensity exhibits the same result as Figure 18 of the X-waist IPERP data, and consequently was not analyzed. Figure 23 shows the photo of the Y-waist vertically polarized, vertically scanned IPAR OTR pattern, which was used for the vertical divergence of the emittance measurement. Immediately, one notices the asymmetry of the right side of the pattern, which suggests some problem in the determination of the Y-waist or the camera alignment. Figures 24A, 24B, and 24C plot the vertically polarized, vertical scans of the OTR patterns against the theoretically generated OTR patterns for inputted divergences of 1.0, 0.7, and 1.3 milliradians respectively. Figure 24A with a divergence of 1.0 mrad. fits the left side of the data reasonably with fair fringe visibility and matching, and the divergence of 1.0 mrad is used as the  $\theta_y$  divergence for the y-emittance measurement. Figures 24B and 24C provide a very rough estimation of the divergence error as  $\pm 0.3$  mrad. The right side of the data in Figure 24A provided no information to the analysis, and is treated as an aberration in the data. The asymmetry in the right side is undetermined, but could be a flare in the OTR pattern or a focusing problem. The resulting input parameters to the y-emittance measurement are the RMS beam radius of  $0.89 \pm 0.1$  mm and a beam divergence of  $1.0 \pm 0.3$  mrad.

Using equation (1), the unnormalized emittance measurements, for a beam energy of 92.58 MeV and the corresponding  $\gamma$  of 182, are:

$$\epsilon_x = 1.65 \text{ mm-mrad.}$$

$$\epsilon_y = 0.89 \text{ mm-mrad.}$$

BS21, Y-WAIST, UP, VS, IPAR, DIV.=1.0 mrad

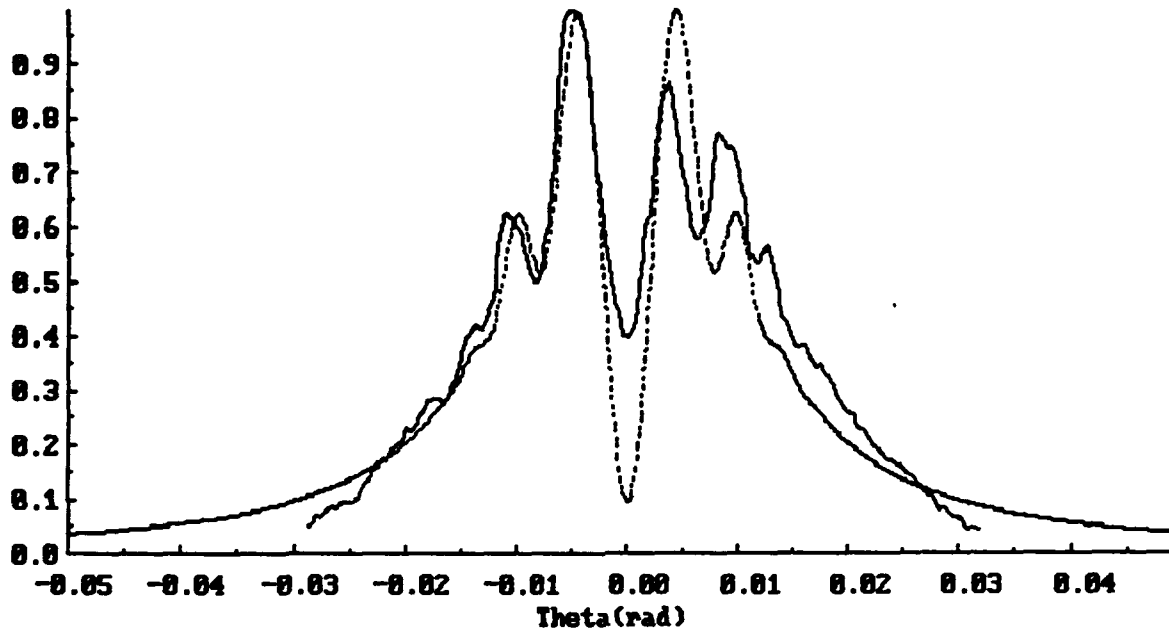


**Figure 24A: Y-waist vertically polarized, vertical scan of IPAR with an inputted divergence of 1.0 mrad. The left side of the data shows good correlation with the theory, but the right side is unable to be correlated. The divergence of 1.0 mrad is used in the y-emittance measurement.**

BS21, Y-WAIST, UP, US, IPAR, DIV.=0.7 mrad

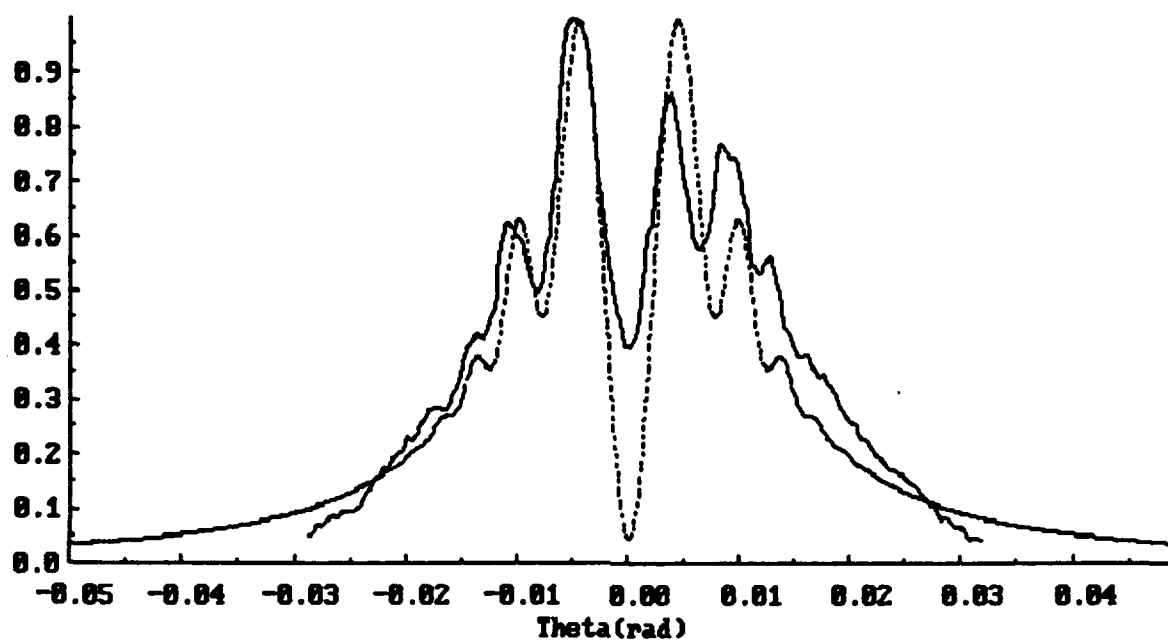


**Figure 24B: The Kapton foil Y-waist vertically polarized, vertical scan of IPAR with a divergence of 0.7 mrad.**

BS21, Y-WAIST, VP, VS, IPAR, DIV.=1.3 mrad

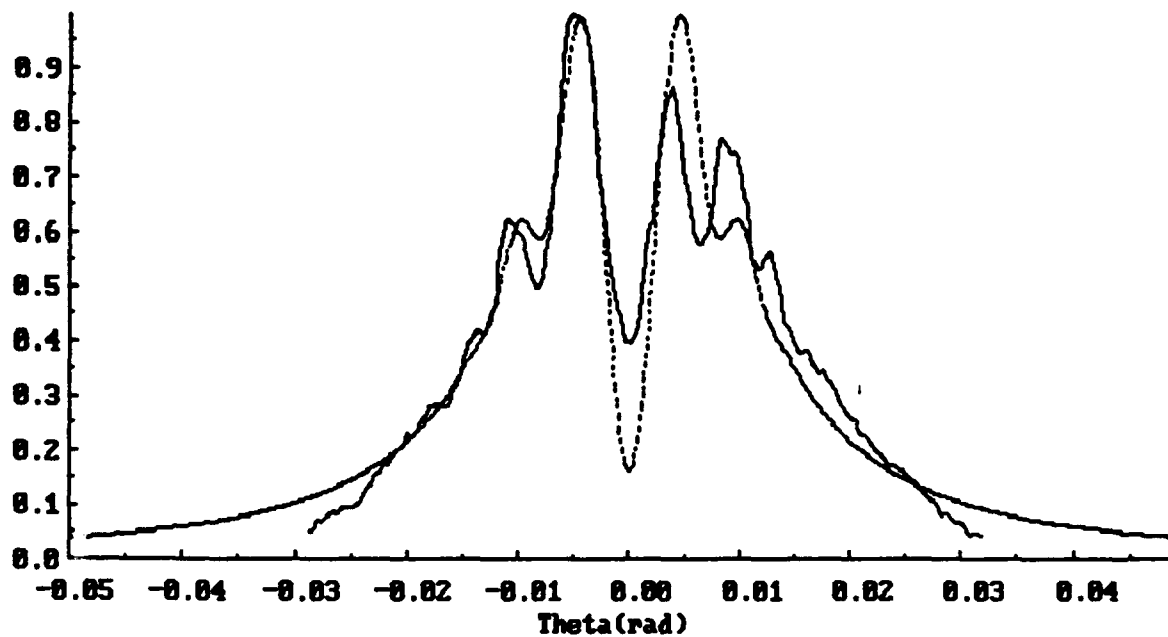


**Figure 24C:** The Kapton foil Y-waist vertically polarized, vertical scan of IPAR with a divergence of 1.3 mrad. This scan is used in error estimation.

The unnormalized emittance measurements are normalized by multiplying by  $\gamma$  such that:

$$\epsilon_n = \gamma \epsilon_{unorm} \quad (27)$$

The normalized emittance values with the margins of error are:

$$\epsilon_x = 95\pi \pm 34\pi \text{ mm-mrad.}$$

$$\epsilon_y = 52\pi \pm 12\pi \text{ mm-mrad.}$$

These normalized values are compared in a later section with the nitrocellulose foil interferometer emittance measurement and other similarly designed linear accelerator emittances.

### C. CLEAR FOIL AMPLITUDE AND COHERENCE EFFECTS

In the November 1990 experiment, the polarizer was initially removed to observe the coherence effects of differing thicknesses of foils on the OTR total intensity (ITOT) emitted as compared to the theoretically generated OTR patterns from Rule's computer code. The premise is that the thinner foil would show greater sensitivity to small changes to its thickness and its index of refraction due to the thickness being closer to the radiation coherence length (given in equation (9)) in the foil medium, more asymmetry of the transition radiation generated from the front surface of the foil, and less attenuation of the emitted OTR through the foil to the optical sensor. The optical calibrations were verified to be the same as the September 1990 experiment, because the experimental setup was identical. The angular calibration is  $3.04\text{E-}4$  radians/pixel, and the x-direction and y-direction conversions are again  $0.136$  mm/pixel and  $0.100$  mm/pixel respectively. The beam energy for this experiment is  $91.36$  MeV, which corresponds to a new Lorentz factor of  $\gamma=179$ .

The Wartski interferometer is a  $.5\text{ }\mu\text{m}$  or  $5\mu\text{m}$  nitrocellulose clear foil and a front surfaced, polished aluminum mirror with an effective foil spacing parallel to the beam of  $0.523\text{ cm}$ . The published foil thicknesses are within 10% of their nominal values, and the average index of refraction over the entire spectrum is 1.5 [Ref. 21]. The filters used for the analysis are  $455\times 50\text{ nm}$  and  $650\times 70\text{ nm}$  bandpass filters. The indices of refraction and attenuation for the aluminum mirror in the optical spectrum are  $n=0.450$  and  $k=3.98$  respectively [Ref. 22].

The emittance and coherence data for the November 1990 experiment were recorded both by the Compaq II computer installed with the XTALK data conversion program for storage in an ASCII format and the HP X-Y plotter as a backup. Appendix A describes the interface of these ASCII data files with Rule's analytic clear foil computer code. for generation of theoretical OTR patterns. Figure 25 displays the unpolarized, horizontal scan of ITOT of the  $0.5\text{ }\mu\text{m}$  foil thickness interferometer with a filter bandwidth of  $455\times 50\text{ nm}$ , and , immediately, one notices the greater fringe visibility and clarity due to the greater accuracy of the optical alignments and learned experience. On the other hand, Figure 26, which is the nominal fit of ITOT of the theory to the data for an effective foil thickness of  $7.571\text{E-}5\text{ cm}$  (based on  $0.5\text{ }\mu\text{m}$ ), a foil spacing of  $0.523\text{ cm}$ , a filter bandwidth of  $440\text{--}470\text{ nm}$ , and a foil refractive index of 1.60, exhibits a washing out of the left side of the data OTR pattern, and the image spans from  $-0.03$  to  $0.04$  radians, which is better than the September experimental result, but indicates that the SITCAM needs to be centered more accurately. The washing out of one side of the data suggests that possibly the SITCAM is not aligned parallel to the center axis of the outgoing OTR, but the phenomena is not significant in the analysis. Moreover, the central minimum is

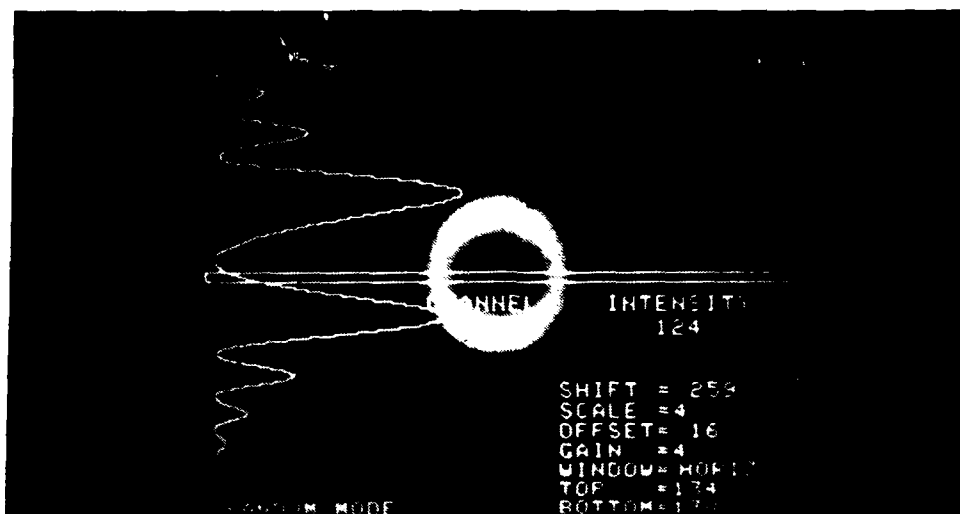


Figure 25: Photo of the unpolarized, horizontal scan of ITOT for the  $0.5\ \mu\text{m}$  foil thickness. Notice the good fringe visibility.

OTR25-2, THIN FOIL  $.5\mu\text{m}$ , ITOT, NOMINAL PARAMETERS

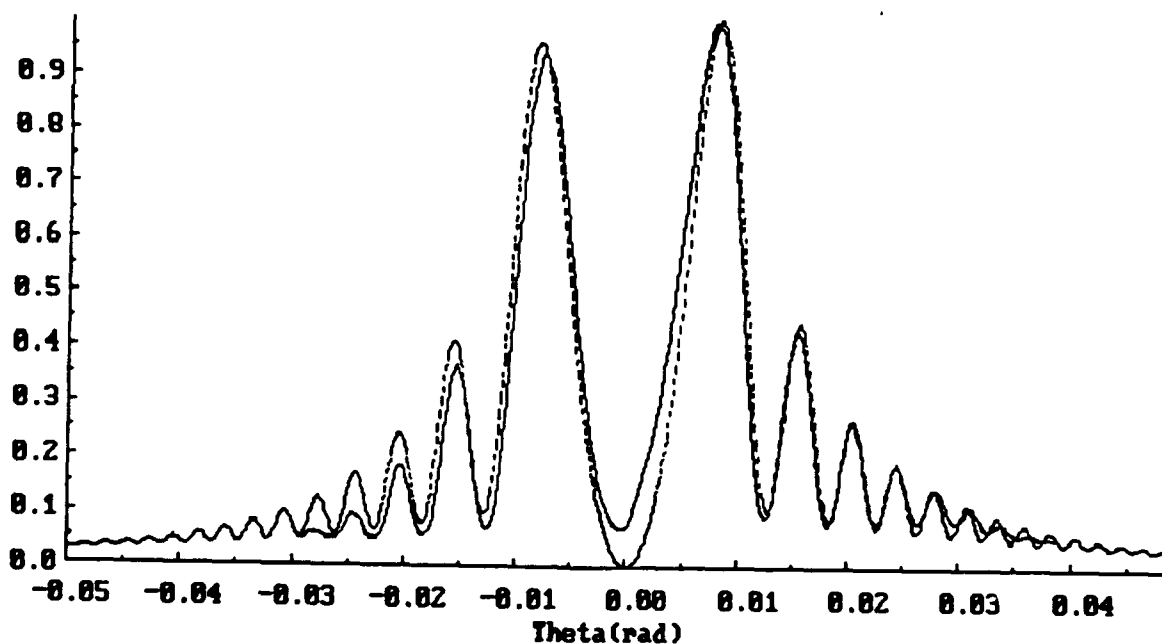


Figure 26: Unpolarized, horizontal scan of ITOT of the  $0.5\ \mu\text{m}$  foil with nominal input parameters of: an effective foil thickness of  $7.571\text{E-}5\ \text{cm}$ , foil spacing =  $0.523\ \text{cm}$ , filter bandwidth  $440\text{-}470\ \text{nm}$ , and  $n_{\text{foil}} = 1.60$ .

slightly filled in compared to the theoretical OTR pattern, and this suggests that the background subtraction may be masking some useful information (this may also be tied into the washing out of the left side of the data). These effects are consistent throughout both the coherence and emittance measurements. The degree of asymmetry for all the data agree with the predicted theoretical OTR patterns, which are generated consistent with the similar observations by Wartski [Ref. 13] referred to in Chapter II. Figure 26 demonstrates excellent correlation between the data and the OTR patterns generated by Rule's clear foil computer code.

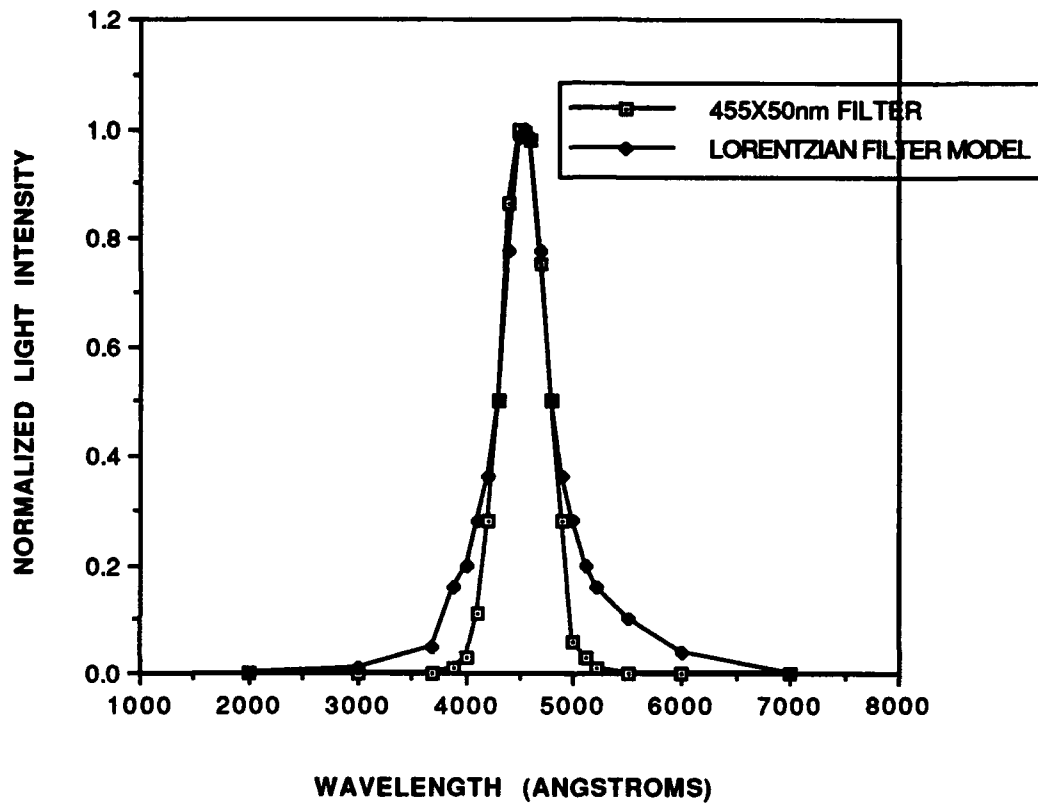
Initially, the 0.5  $\mu\text{m}$  nitrocellulose foil interferometer unpolarized data is fit to the theoretically generated OTR patterns, and several interesting developments occur. First, fringe matching and clarity are poor due to the inputted filter bandwidth being too large. In Rule's analytic code [Ref. 19], the inputted filter function assumes a Lorentzian shaped bandwidth filter. When compared with the normalized actual filter of 455x50 nm profile in Figure 27A, the Lorentzian wings appear significant. This fact becomes more apparent in Figure 27B, because one can see that the wings pass 10-22 percent of the intensity in the 10 nm bandwidths just outside of the filter bandwidth. The solution would be to digitize the actual filter bandwidth profile and use this file as the inputted data for the computer code, or use a filter that closely resembles a Lorentz profile like the Corning filter used in September. For the 455x50 nm filter, the modelled Lorentz profile was based on a bandwidth of 440-470 nm, and used as the filter input parameter consistent throughout all of the emittance and coherence measurements. Second, after the new filter bandwidth was input, the data parameter for the index of refraction for the foil was 1.5, and

Figure 28 shows that despite good peak matching, fringes visibility in the theoretical OTR patterns is poor. This phenomena is diagnosed by recalling [Ref. 23] that, for clear prisms, the frequency dependent index of refraction ( $n(\omega)$ ) is related to the plasma frequency ( $\omega_p$ ) and the observation frequency ( $\omega$ ) by :

$$n(\omega) \cong 1 + \frac{\omega_p^2}{2} \left( \frac{1}{\omega_o^2 - \omega^2} \right), \text{ where } \omega_o \text{ is the resonance frequency.} \quad (28)$$

Therefore, the actual refractive index is dependent on the observed frequency bandwidth, and this phenomena is convolved with the sensitivity of foil thickness to the change in the index of refraction. With the 0.5  $\mu\text{m}$  (thin) foil interferometer modelled in the code, the inputted foil index of refraction is stepped from 1.5-1.65 in steps of 0.05 in Figures 28, 29A, 26, and 29B respectively. Figure 26 displays the optimum correlation of the theoretical intensity, ITOT, to the data for an index of refraction of 1.60, and, by viewing these OTR comparisons together, the thin foil exhibits good sensitivity to the change in the index of refraction with respect to both fringe visibility and the expected asymmetry of the OTR pattern. Figure 29B,  $n=1.65$ , closely correlates the theory to the data, but shows the mismatch in the asymmetry in the OTR pattern as compared to Figure 26. The correlation of Figures 28 and 29A are easily discernable. Therefore, for the 455x50 nm filter bandwidth, the 0.5  $\mu\text{m}$  foil OTR pattern is able to "dial in" the refractive index as  $\sim 1.60$ . In order to verify this result, the 5  $\mu\text{m}$  (thick) foil data is used, and the index of refraction is again stepped from 1.5-1.65 in Figures 30A, 30B, 30C, and 30D respectively. Although the thick foil does not show the degree of sensitivity of

### 455x50 NM FILTER VS. LORENTZIAN FILTER MODEL



**Figure 27A:** The computer code Lorentzian shaped filter model compared to the actual filter bandwidth. The wings of the model still pass a significant portion of the spectrum intensity outside the bandwidth.

## SIGNIFICANCE OF LORENTZIAN BANDPASS WINGS

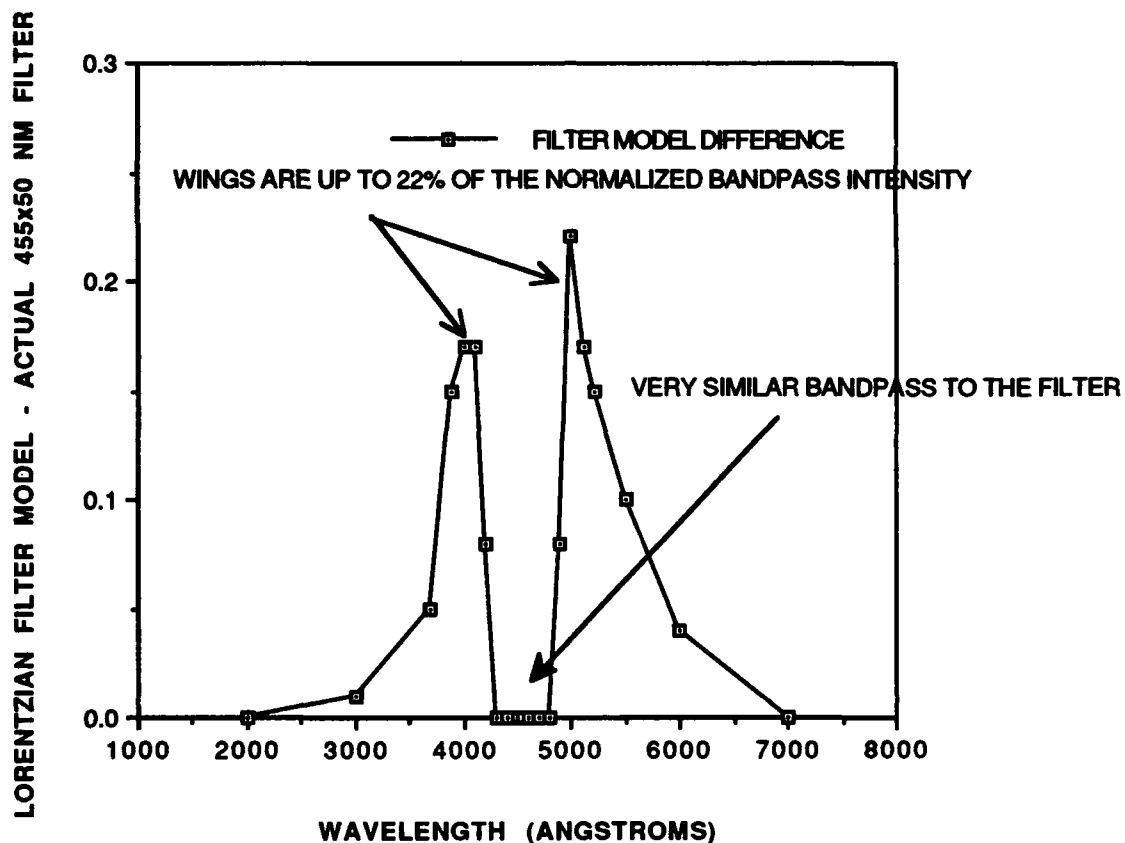


**Figure 27B:** The difference between the filter model and the actual filter profile is evident in the models wings outside the bandpass region. The model passes 10-22% of the intensity in this outer spectrum.

OTR25-2, REFRACTIVE INDEX INPUT:  $n=1.5$

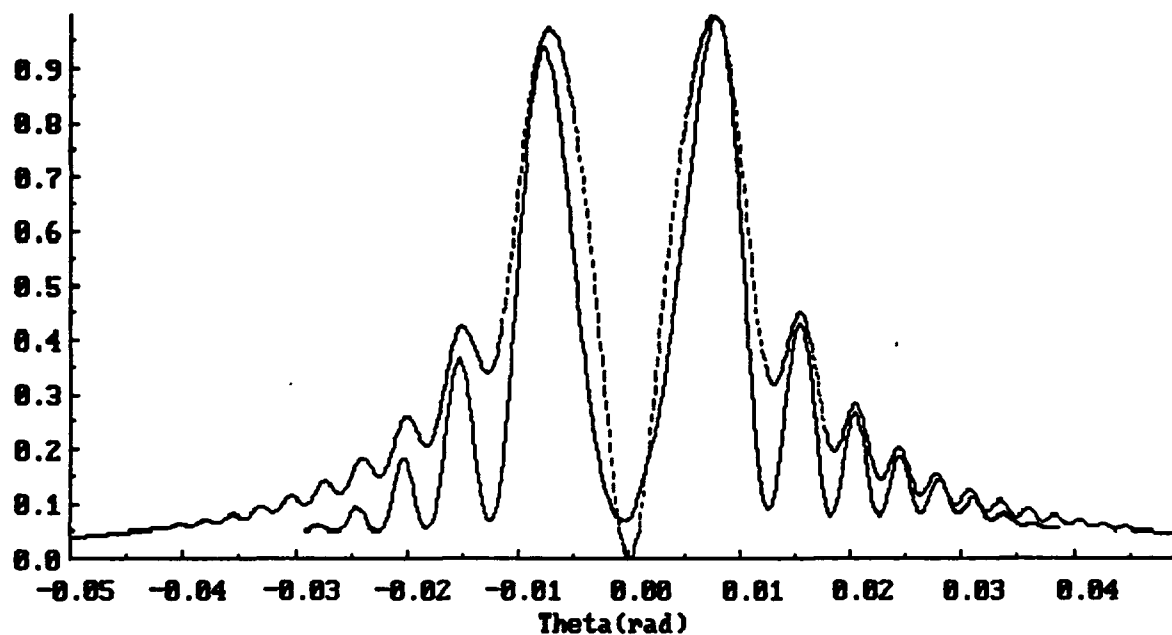


**Figure 28:** The unpolarized, horizontal scan of ITOT of the 0.5  $\mu\text{m}$  foil with an index of refraction of the foil of 1.5. Note that the fringes have washed out in the theory and the asymmetry does not match the data. the effect of the thin foil is magnified compared to the thick foil.

OTR2S-2, REFRACTIVE INDEX INPUT:  $n=1.55$

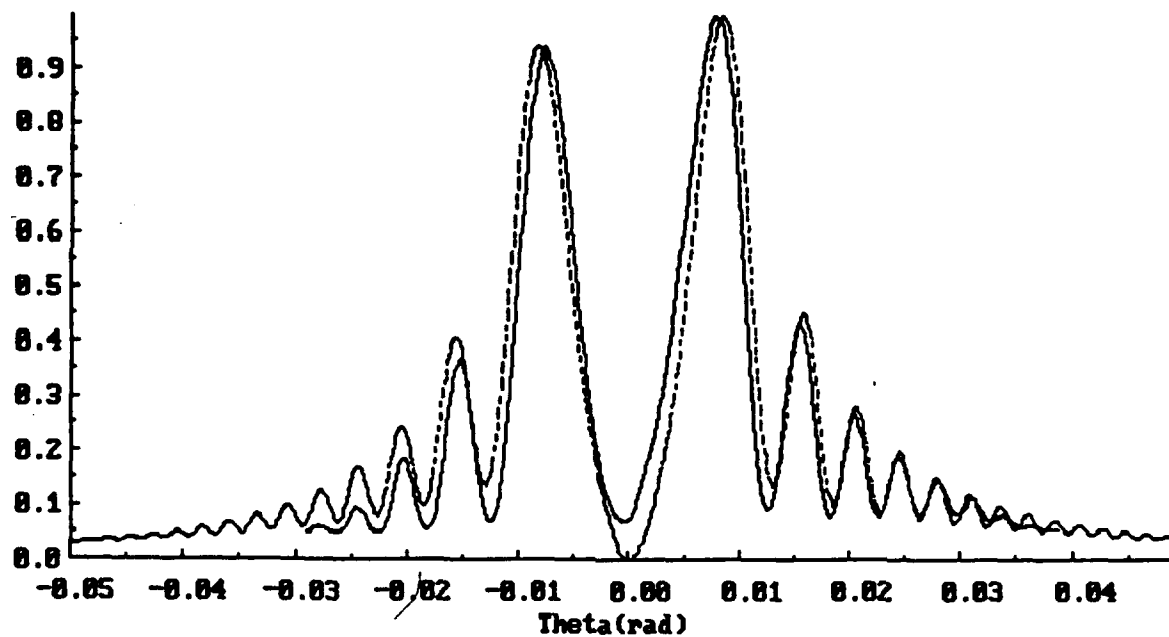


**Figure 29A:** The unpolarized, horizontal scan of ITOT for the thin foil with  $n=1.55$ . Note poor fringe matching.

OTR25-2, REFRACTIVE INDEX INPUT:  $n=1.65$

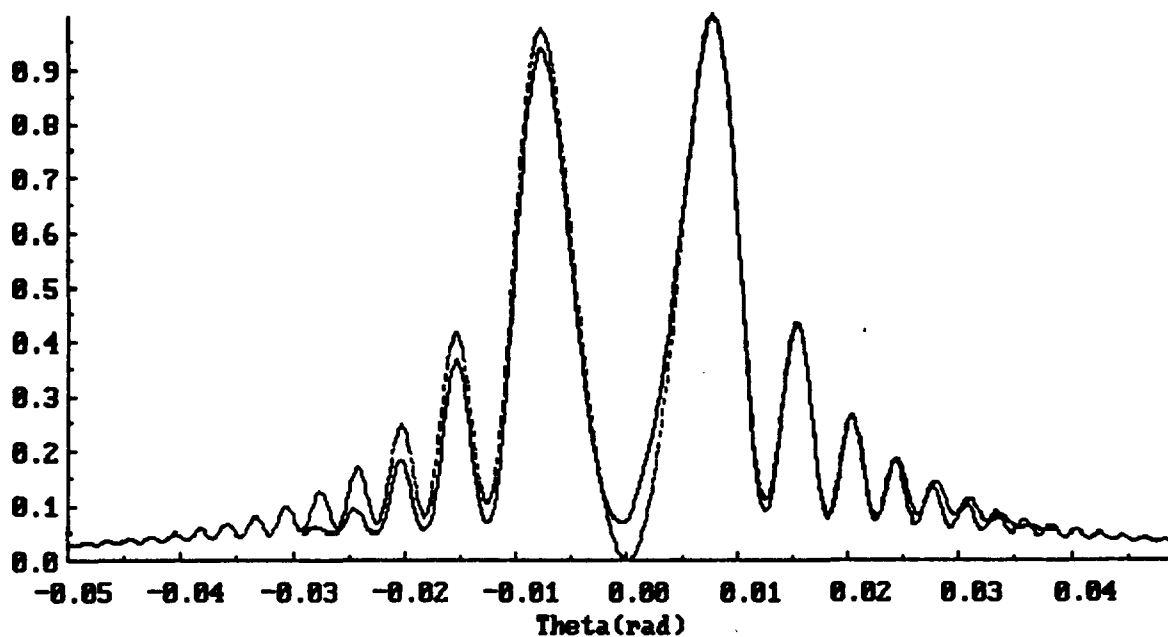


**Figure 29B:** The unpolarized, horizontal scan of ITOT for the thin foil with  $n=1.65$ . Note the asymmetry mismatch despite good fringe matching.

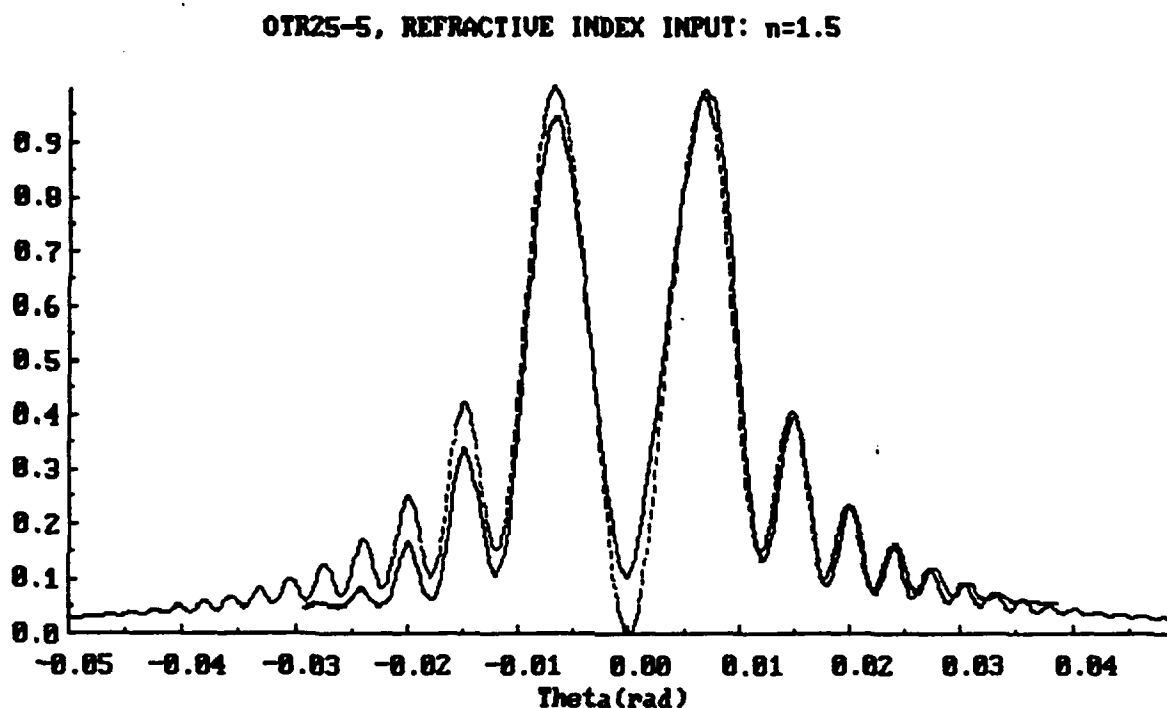


**Figure 30A: The unpolarized, horizontal scan of ITOT of the 5  $\mu\text{m}$  foil thickness for an inputted index of refraction  $n=1.5$ . The asymmetry of the theoretical OTR does not match the data.**

**The effect is not as pronounced as in the thin foil case probably because of attenuation of the radiation through the foil and the foil is much greater than the coherence length in the foil medium.**

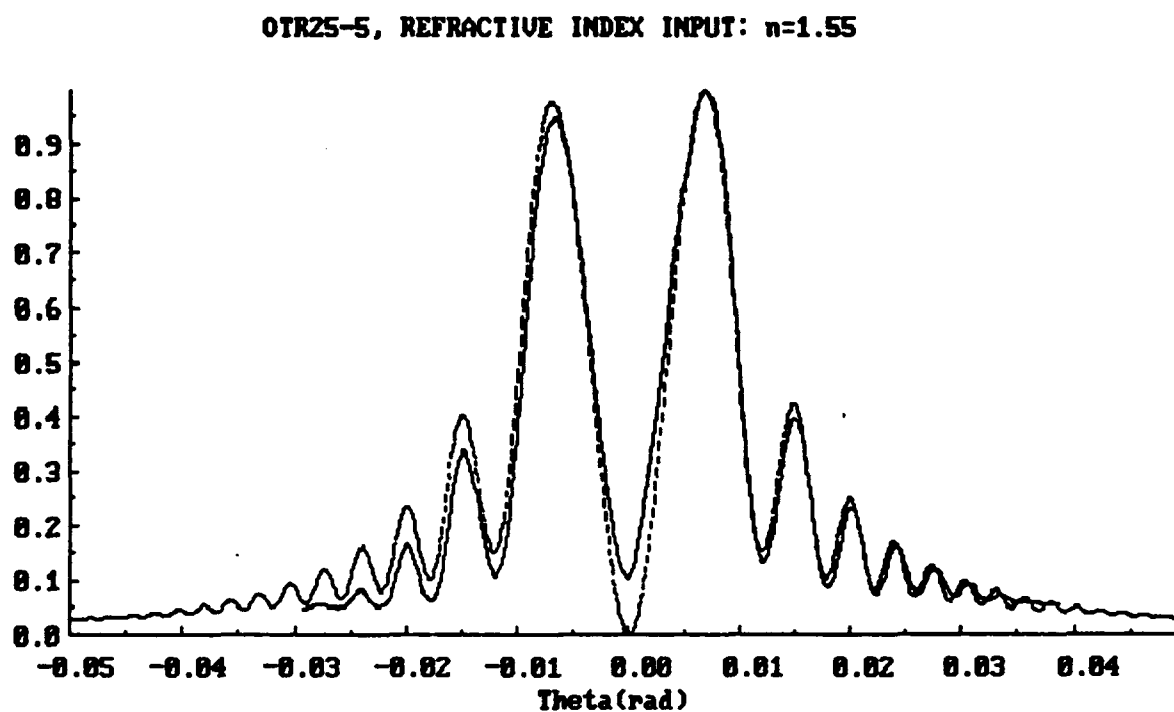


**Figure 30B:** The unpolarized, horizontal scan of ITOT of the thick foil with  $n=1.55$ . Note again the asymmetry mismatch.

**OTR25-5, THICK FOIL 5 $\mu$ m, ITOT, NOMINAL PARAMETERS**

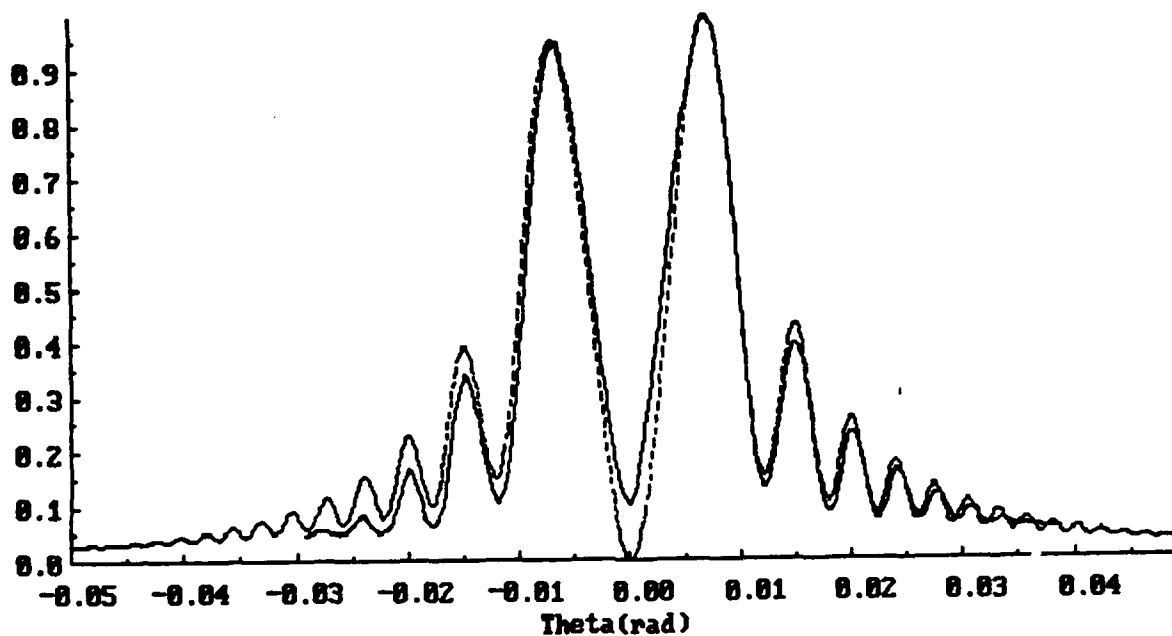


**Figure 30C: The unpolarized, horizontal scan of ITOT for the 5  $\mu$ m foil thickness with an index of refraction of 1.60 in the bandwidth of 455x50 nm. The fringe and asymmetry matching are good. These input parameters are the nominal input parameters for the emittance measurement.**

OTR25-5, REFRACTIVE INDEX INPUT:  $n=1.65$

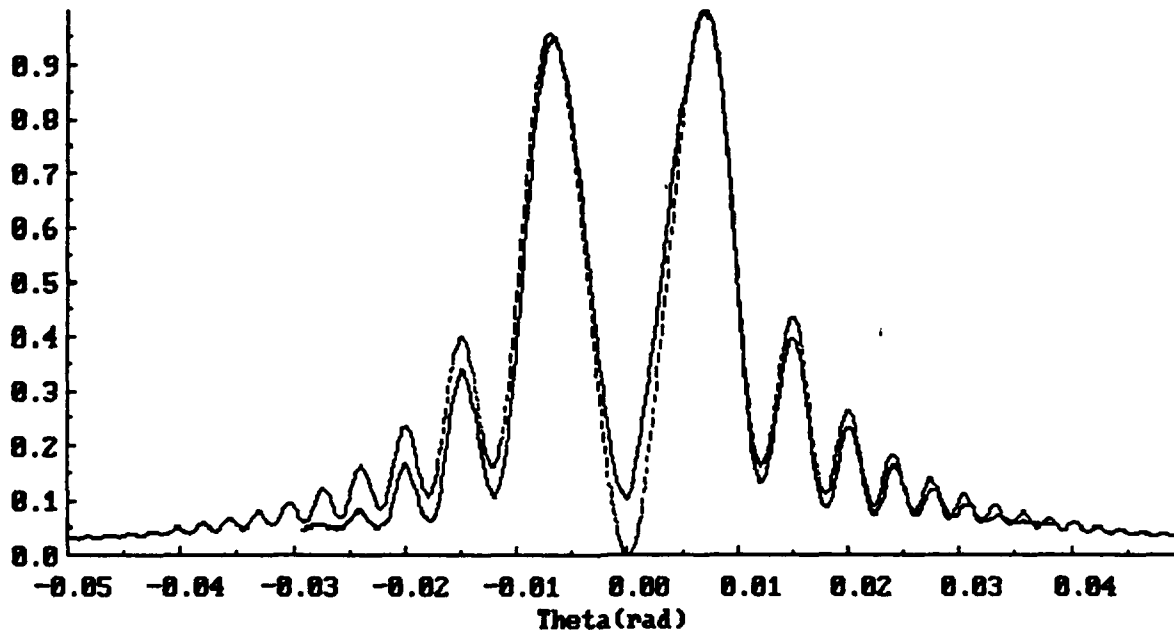


**Figure 30D:** The unpolarized, horizontal scan of ITOT of the thick foil for  $n=1.65$ . Good fringe matching is evident, but the slight difference in asymmetry indicates that the correlation is not optimum.

the thin foil with regards to fringe visibility, the asymmetry of the figures is affected. Figure 30C displays the optimum correlation of the theory to the data at  $n=1.60$ . The changing asymmetry phenomena evident in the theoretical OTR patterns in the figures is probably attributed to the constructive and destructive interference of the clear foil OTR amplitudes generated at the front and back surfaces of the foil, and these interference phenomena are dependent on the foil's index of refraction through the reflection and transmission coefficients given by equations (20A) and (20B).. Figure 31 shows a photograph of the 5  $\mu\text{m}$  foil interferometer OTR pattern with the 455x50 nm filter, and is the nominal OTR data pattern used to determine the input parameters to the computer code for the emittance measurement. The lesser sensitivity of the thicker foil to the index of refraction is due to two mechanisms. The foil spacing between the foil and the mirror is very narrow, 0.523 cm, and, consequently, the reflected OTR of all three clear foil amplitudes are emitted back through the foil to the optical sensor on the SITCAM. The result is that the thicker foil will attenuate (small effect) the outgoing OTR more than the thin foil by its thickness (see Figure 32). The thicker foil exhibits the dominant feature of the asymmetry, because the front foil surface generated OTR travels two different path lengths through the foil on each side of the beam line shown in Figure 32 at point A, and the foil path lengths are more pronounced in the thicker foil. The thin foil exhibits the asymmetry and the fringe visibility sensitivity, because the thickness of the thin foil approaches the radiation coherence length in the medium,  $L_m$ , given in equation (9), and the path lengths,  $d$  and  $d'$ , differ in their approximation to  $L_m$ . The thick foil is less sensitive, because its thickness is greater than  $L_m$ . The radiation coherence length is proportional to the square root of the dielectric

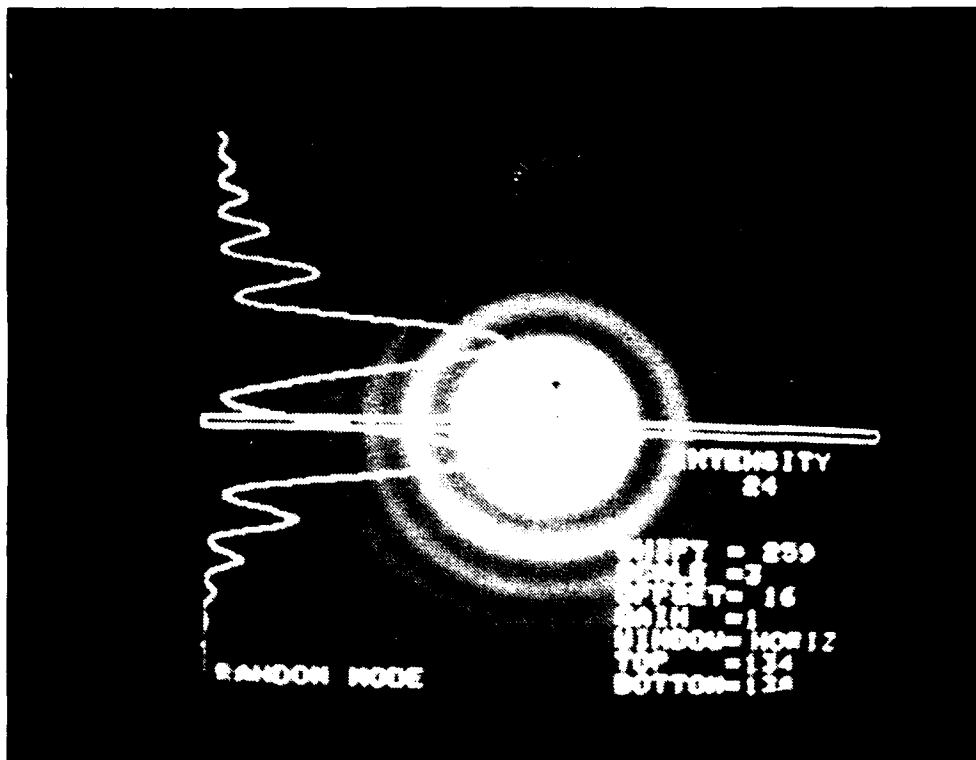


**Figure 31: Photo of the 5  $\mu\text{m}$  foil OTR pattern with the 455x50 nm filter bandpass used for determining the index of refraction for the foil for the emittance measurement.**

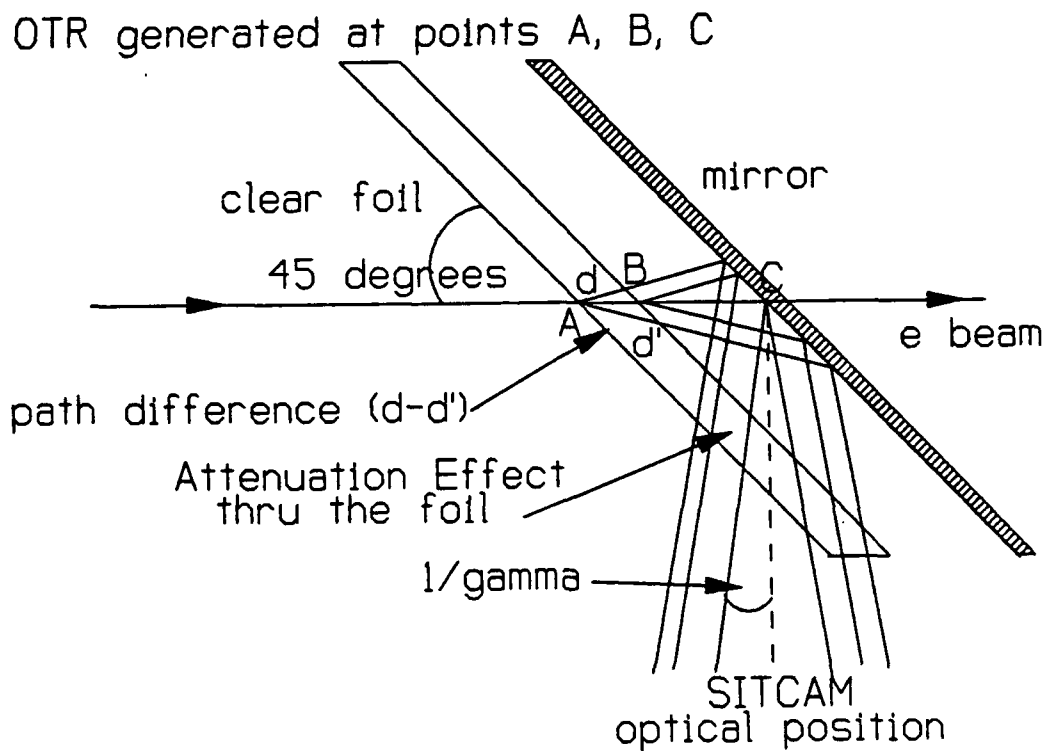


**Figure 32: The coherence effects of the OTR radiation through the foil. The asymmetry is mainly generated by the path differences  $d$  and  $d'$  from the clear foil OTR amplitude originating at point A and their approximation to the magnitude of the foil's radiation coherence length.**

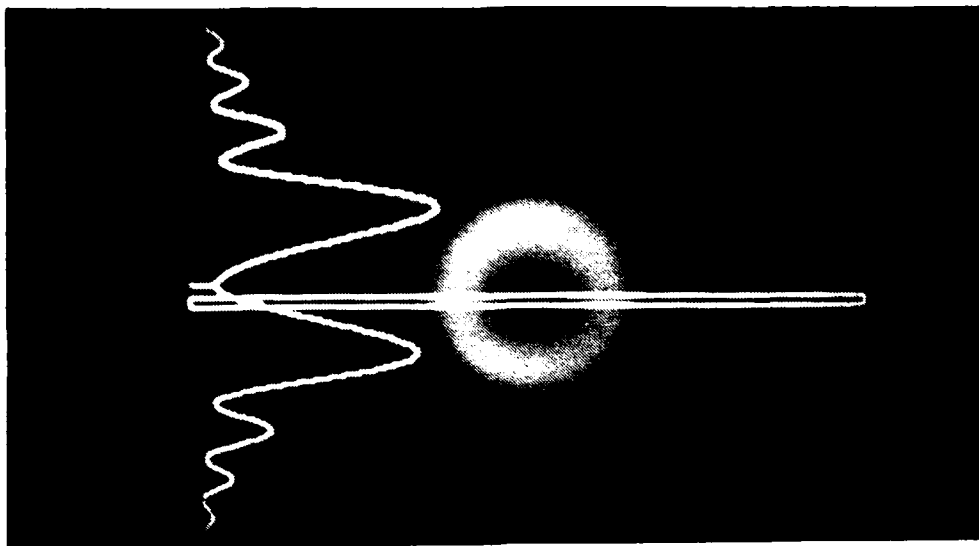


Figure 33: Photo of the unpolarized OTR pattern from the 5  $\mu\text{m}$  foil in the bandwidth of 650x70 nm.

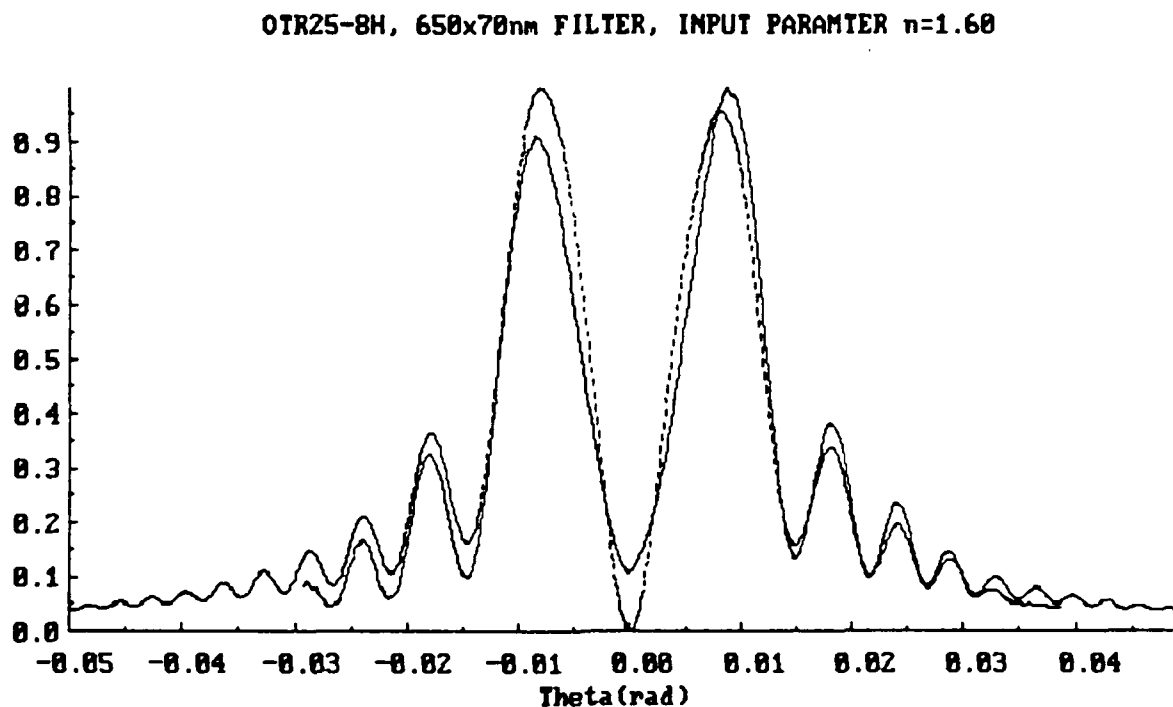
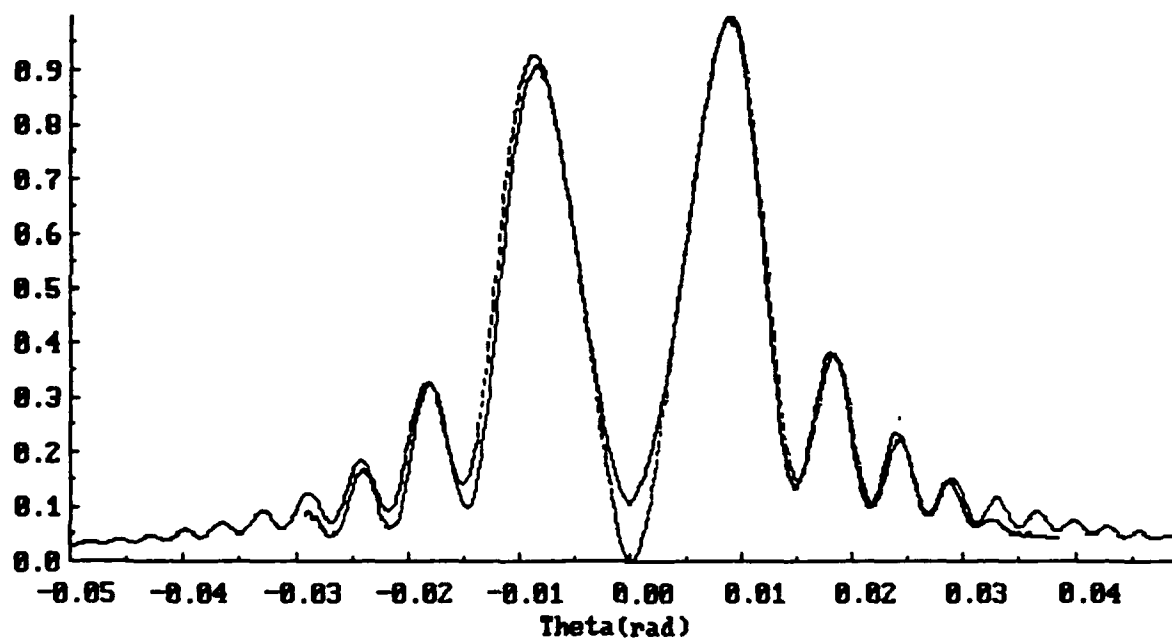


Figure 34A: The unpolarized, horizontal scan of ITOT for the 5  $\mu\text{m}$  foil in the bandwidth of 650x70 nm with  $n=1.60$ . The theory exhibits poor fringe and asymmetry matching.

OTR25-84, 650x70 nm FILTER, REFRACT. INDEX,  $n=1.46$



**Figure 34B: The unpolarized, horizontal scan of ITOT for the 5  $\mu\text{m}$  foil in the 650x70 nm bandpass with  $n=1.46$ . The theory shows strong correlation with the data matching asymmetry and fringe visibility.**

constant, and, consequently, the thickness of the thin foil may be less than the wave formation zone in the foil resulting in a non-coherent OTR wave exiting the foil. In addition, from Chapter II, Wartski shows that the asymmetry is inherent in the backward OTR due to the Fresnel effect, but the effect is amplified or changed due to the phase addition of the clear foil OTR amplitudes. Figure 28 displays this result effectively for  $n=1.5$ . In order to verify these effects, a possible experiment is to develop a Wartski interferometer with a foil spacing large enough to view the exiting OTR between the foils without looking through the front foil. The asymmetry phenomena and the coherence effects should be larger and easier to measure without the foil interference. Returning to the dependence of the index of refraction on the frequency of the observed radiation, Figure 33 shows a photo of the unpolarized, horizontal scan of ITOT of the 5  $\mu\text{m}$  foil in the bandwidth of 650x70 nm, and Figure 34A displays the theoretical OTR pattern generated with an input index of refraction of 1.60. Figure 34A exhibits poor  $1/\gamma$  central peak matching and no asymmetry as is evidenced by the actual 650x70 nm image data. By fitting the index of refraction at  $n=1.46$ , Figure 34B demonstrates good correlation between the computer generated OTR pattern and the data. The maximum variation of the published index of refraction is less than 8 percent, and supports the dependence of the index of refraction on the observed frequency bandwidth.

Finally, in order to further verify the coherence effect of the clear foil thickness, the foil thicknesses were varied by the published margin of error of 10 percent. The 5  $\mu\text{m}$  foil exhibited little sensitivity to changes in the thickness of the foil as evidenced by Figures 35A and 35B, because the thickness was greater than the medium radiation coherence length. In fact, using  $n=1.60$  and

the input parameters of Figure 30C, Figure 35A closely correlates the theory with the data with the exception of being 90% of the nominal foil thickness. Figure 35B displays the same correlation to Figure 30C with the exception of a small variation in the expected asymmetry for 110% of the nominal foil thickness. On the other hand, Figure 26 displays the nominal parameters of the 0.5  $\mu\text{m}$  foil thickness, which has an input index of refraction of 1.60 and an inputted foil thickness of 103% of the published 0.5  $\mu\text{m}$  value. Figure 36A displays the peak mismatch in the theory caused by the inputted foil thickness of exactly 0.5  $\mu\text{m}$ , and, as shown previously, index of refraction does not affect the peak mismatch in the outer fringes. The high sensitivity to variations in the thin foil thickness is again based on the radiation coherence length in the foil given by equation (9). The OTR generated from the front surface of the foil must travel at least as far as the wave formation zone in the foil medium in order for it to add coherently with the other two transition radiation amplitudes. Figure 36B shows that, for 90% of the nominal thin foil thickness, the theoretical OTR pattern fails to show the necessary fringe visibility that is present in the data. Figure 36C is consistent with this view, because the foil is now thicker and is a order of magnitude of the coherence length, and the only difference is due to the oblique incident effects. In order to further validate the clear foil analytic code developed by Rule, the program's clear foil amplitudes were removed from the analysis of the thin foil. Figure 37 displays the theoretically generated non-clear foil OTR pattern against the data. The peak mismatch and weak fringe visibility quickly dictate that the clear foil amplitude effects are necessary to obtain the nominal results presented in Figure 26.

OTR25-5, FOIL THICKNESS INPUT:90% OF 5um

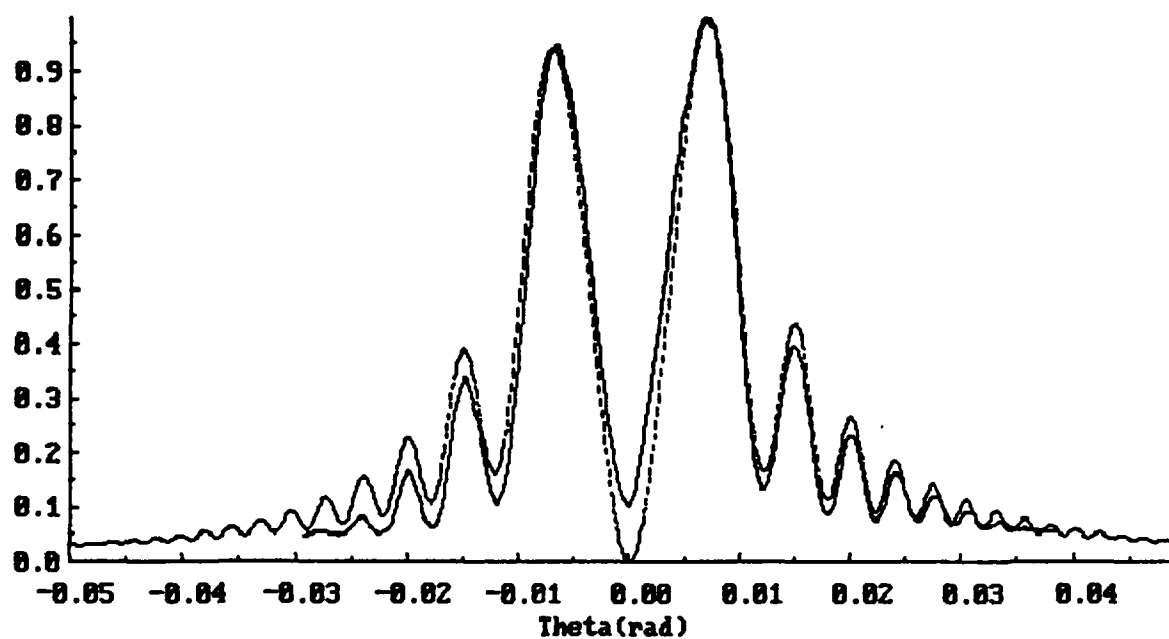


**Figure 35A: Unpolarized, horizontal scan of ITOT for the 5  $\mu\text{m}$  foil with the inputted foil thickness of 90% of the nominal value. Note that the thick foil is not sensitive to small changes in the foil thickness.**

OTR25-5, FOIL THICKNESS INPUT:110% OF 5um

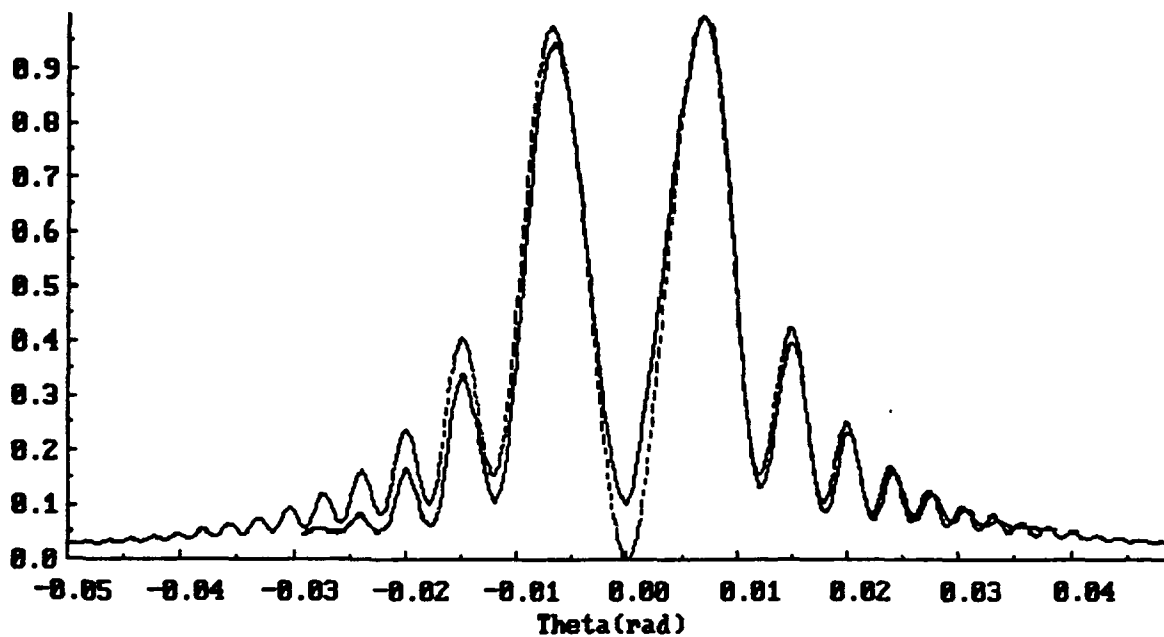


**Figure 35B: Unpolarized, horizontal scan of ITOT for the thick foil with an inputted foil thickness of 110% of nominal. Some slight asymmetry, but fair correlation.**

OTR25-2, FOIL THICKNESS EQUAL TO EXACTLY .5 $\mu$ m

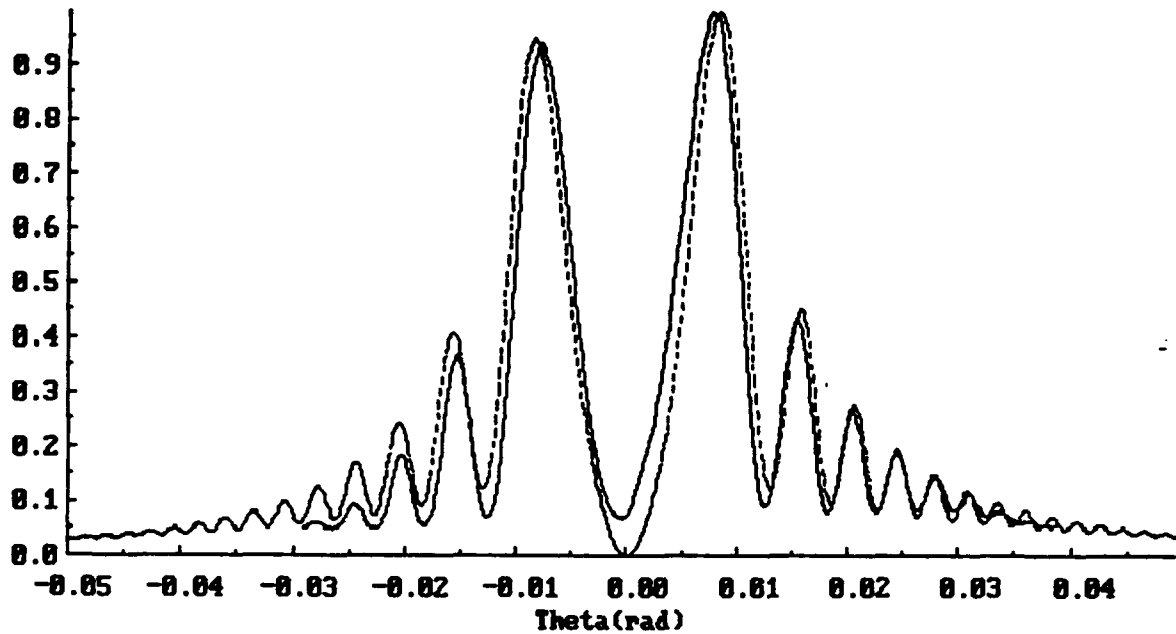


**Figure 36A: Unpolarized, horizontal scan of ITOT for an inputted foil thickness of exactly 0.5  $\mu$ m. Note the peak mismatch and decreased fringe visibility as compared to the nominal parameter thickness of 103% of 0.5  $\mu$ m as displayed in Figure 26.**

OTR25-2, FOIL THICKNESS INPUT: 90% OF  $.5\mu\text{m}$

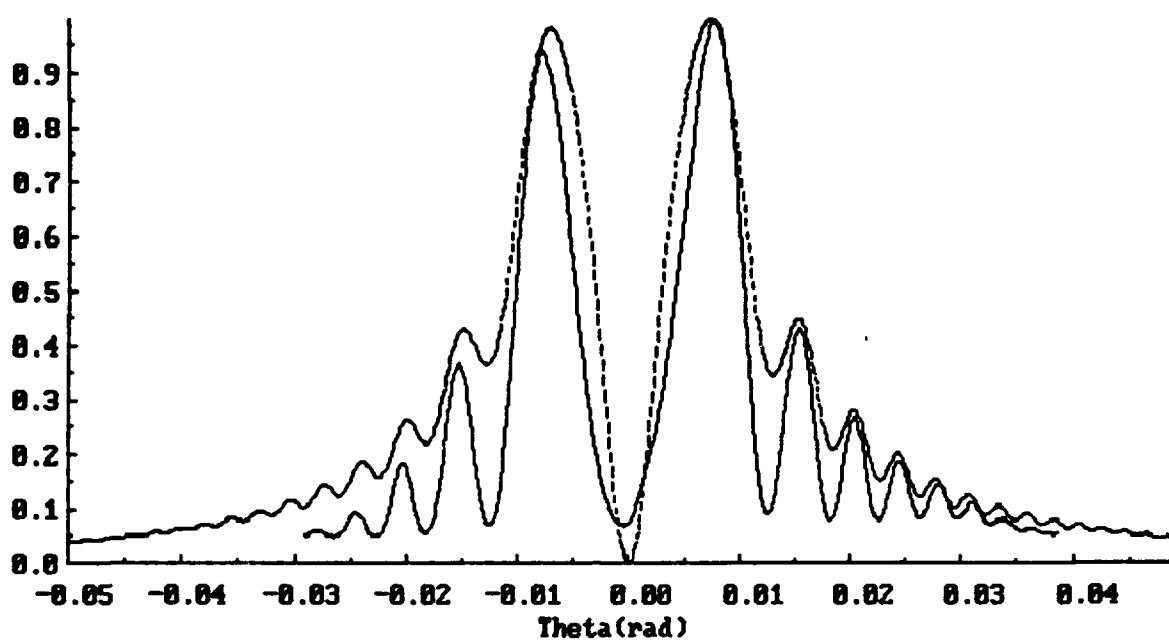


**Figure 36B:** The inputted foil thickness is 90% of the thin foil thickness, and the absence of fringe visibility indicates that the front-surface OTR amplitude is not adding coherently with the other OTR amplitudes.

OTR25-2, FOIL THICKNESS INPUT: 110% OF .5um

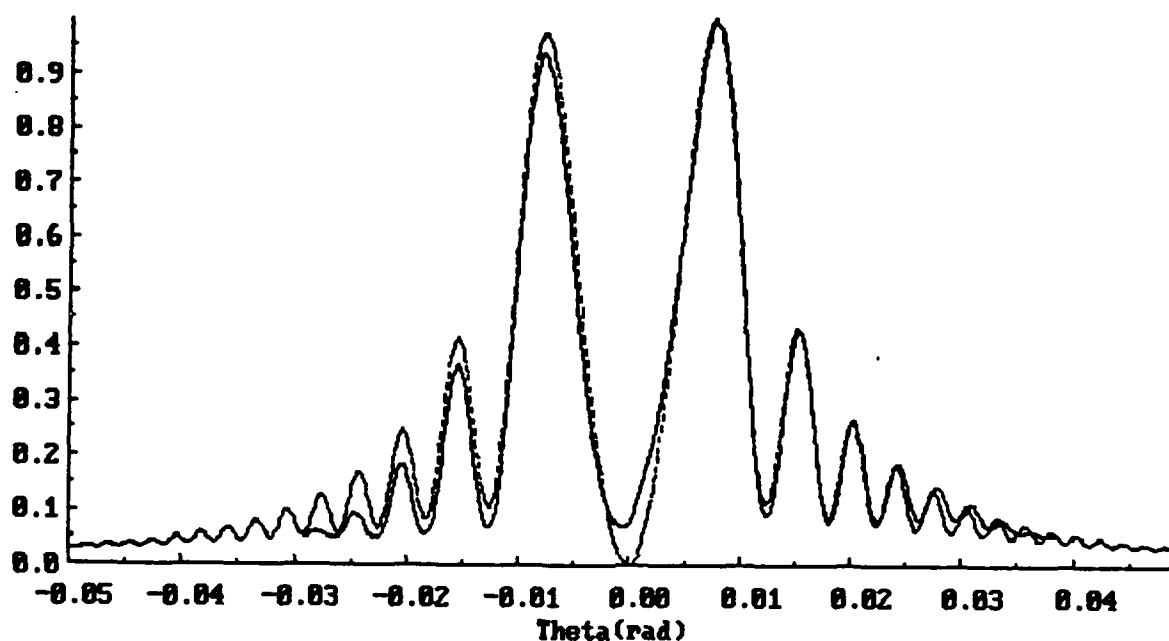


**Figure 36C: Unpolarized, horizontal scan of ITOT for the thin foil with the inputted foil thickness of 110% of the nominal value. The coherence effects are obvious, and the asymmetry is due to foil attenuation and interference with the back surface generated OTR.**

**OTR25-2, CLEAR FOIL AMPLITUDES REMOVED**

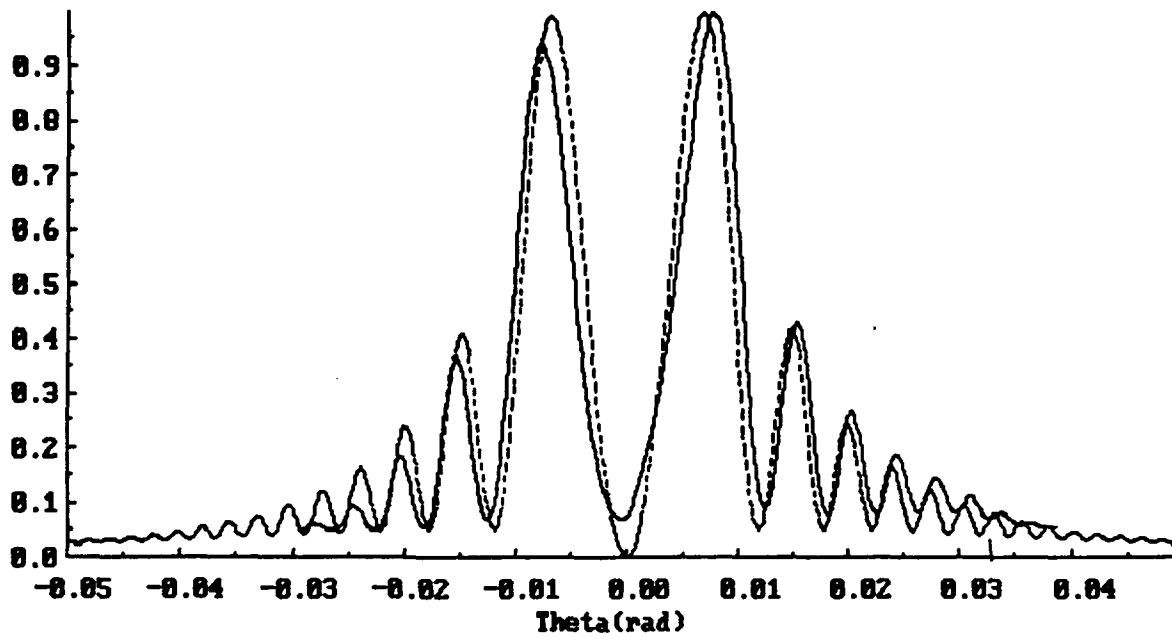


**Figure 37: The clear foil amplitudes are removed in the theoretically generated OTR pattern. The lack of 1/γ central maximum peak matching and outer fringe matching along with poor data correlation display the necessity and validity of Rule's analytic clear foil code.**

#### **D. THE EMITTANCE MEASUREMENT: NOVEMBER 1990**

Using the results from Part C above for the nitrocellulose foil coherence effects, the nominal input parameters for the emittance measurement are obtained from Figure 30C. The interferometer consisted of the nominal 5  $\mu\text{m}$  nitrocellulose clear foil and the aluminum polished mirror (with input indices of  $n=0.450$  and  $k=3.98$ ) with an effective foil spacing parallel to the beam line of 0.523 cm. The observed frequency bandwidth is 455x50 nm, and the inputted bandwidth is 440-470 nm due to the filter modelling in the code. The foil index of refraction is 1.60, and the beam energy is 91.36 MeV which corresponds to a Lorentz factor  $\gamma$  of 179. The divergence in the horizontal and vertical directions are free parameters in the emittance measurement and are adjusted as necessary to fit the data to the theory. The angular and distance calibrations are the same as for the Kapton foil interferometer measurement.

Figure 38A displays the photo of the X-waist beam image captured by the SITCAM at the image plane. The photo displays some reflection effect that was not effectively eliminated during the data acquisition. Figure 39 displays the X-waist beam intensity horizontal scan, and calculates the RMS beam radius for the x-emittance as  $2.43 \pm 0.1$  mm after the reflections were removed mathematically. The SITCAM was then repositioned to the focal plane, and Figure 38B shows the horizontally polarized, horizontal scan of IPAR intensity at the X-waist used to determine the divergence,  $\theta_x$ , for the emittance. The divergence measurement is obtained from Figures 40A, 40B, and 40C for the correlation of the theoretical IPAR OTR patterns at the horizontally polarized X-waist. Figure 40B displays the correlation of the theoretically generated OTR pattern for a 0.7 mrad divergence with excellent fringe visibility and matching.

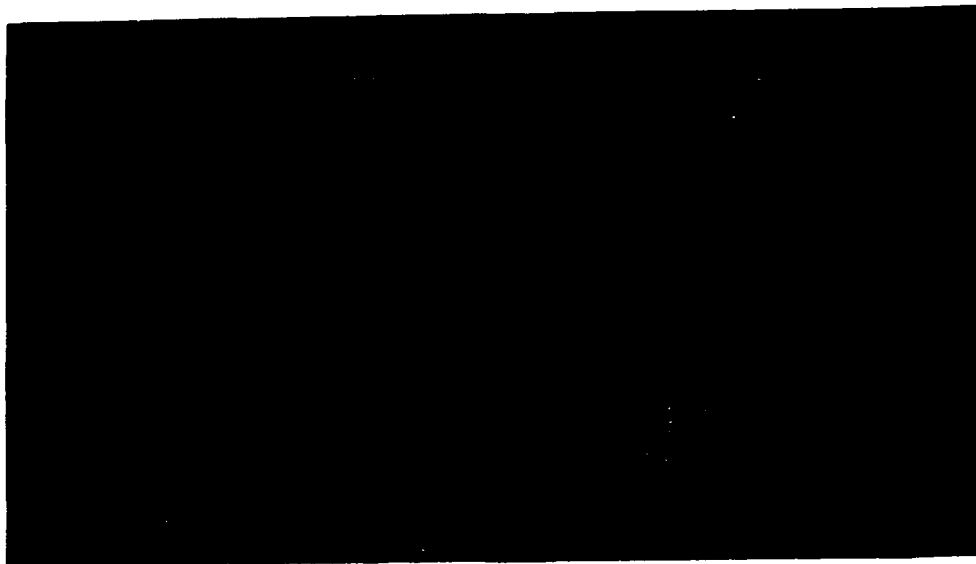


**Figure 38A:** Nitrocellulose foil. X-waist beam image focused at the image plane. Note the reflection images.

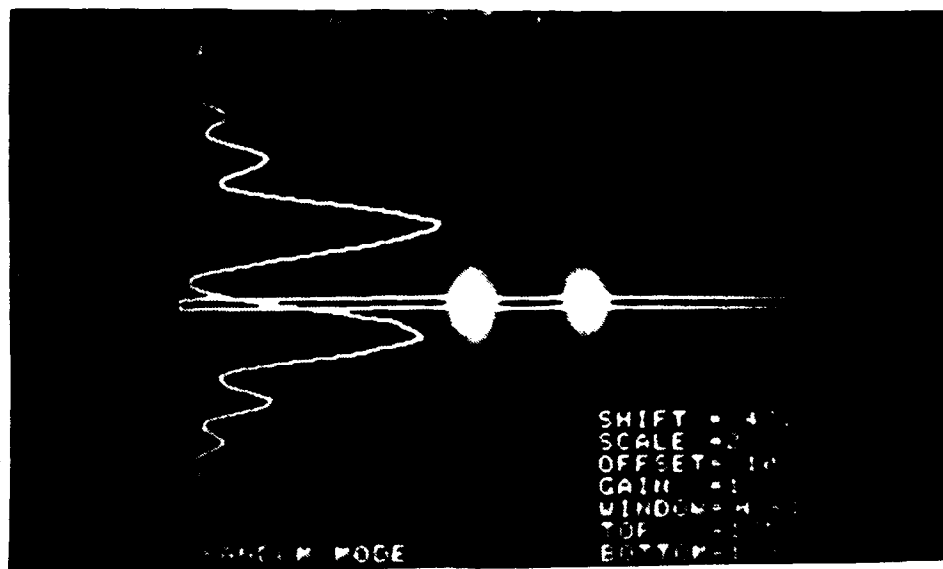


**Figure 38B:** Nitrocellulose foil. X-waist horizontally polarized, horizontal scan of IPAR used for the divergence measurement in the emittance measurement.

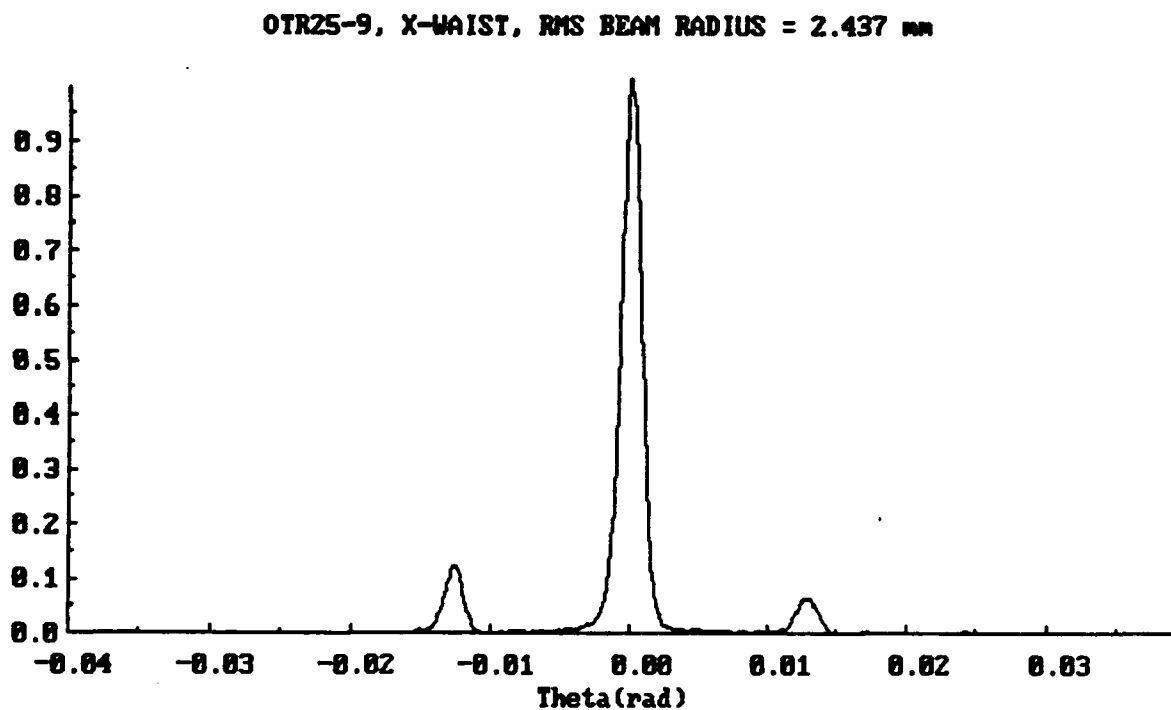


**Figure 39: Horizontal scan of intensity of the X-waist beam spot. The side lobes are due to window reflections. The RMS beam radius is 2.43 mm after the reflections are removed mathematically.**

OTR25-11, X-WAIST, HP, HS, IPAR, DIV.=0.6 mrad

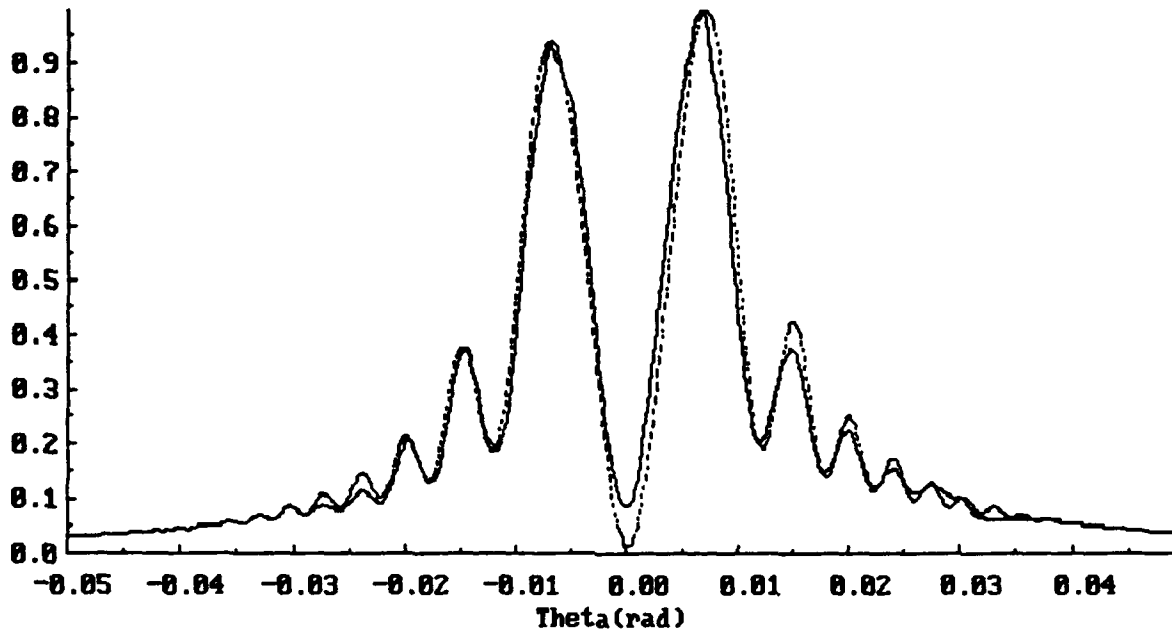


**Figure 40A: The X-waist horizontally polarized, horizontal scan of IPAR for the nitrocellulose foil using a divergence of 0.6 mrad. Despite good fringe matching, the divergence is too small to fit the minima in the fringes.**

OTR25-11, X-WAIST, HP, HS, IPAR, DIV.=0.7 mrad

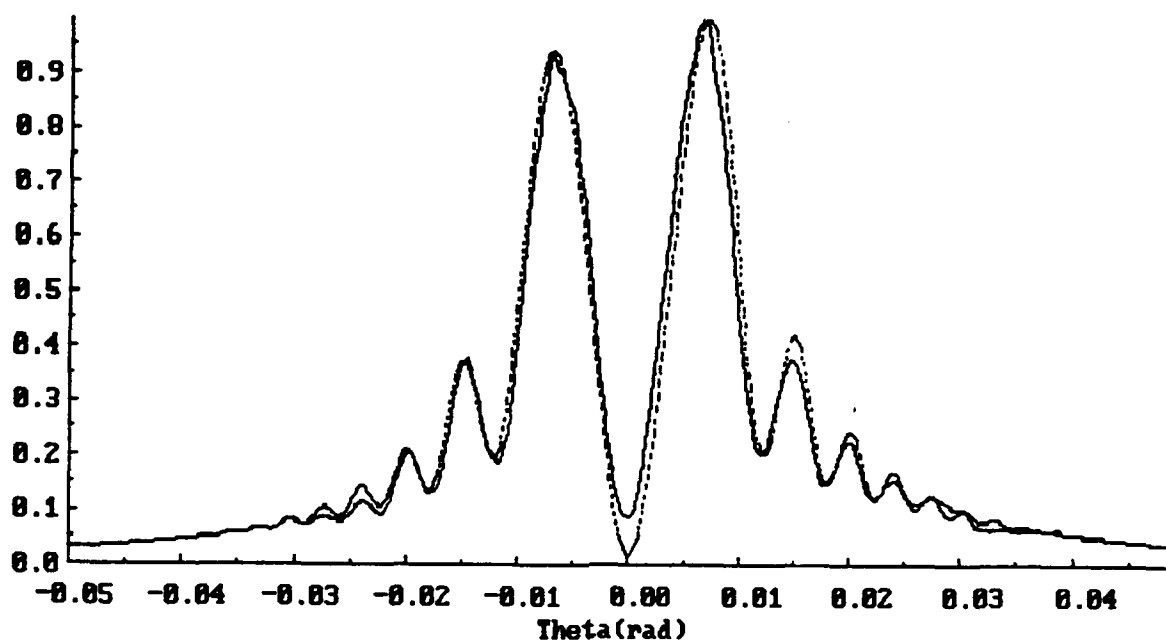


**Figure 40B: The X-waist horizontally polarized, horizontal scan of IPAR for the nitrocellulose foil. with a divergence of 0.7 mrad. The correlation is excellent, and this is the divergence measurement for the emittance.**

OTR25-11, X-WAIST, HP, HS, IPAR, DIU.=0.8 mrad

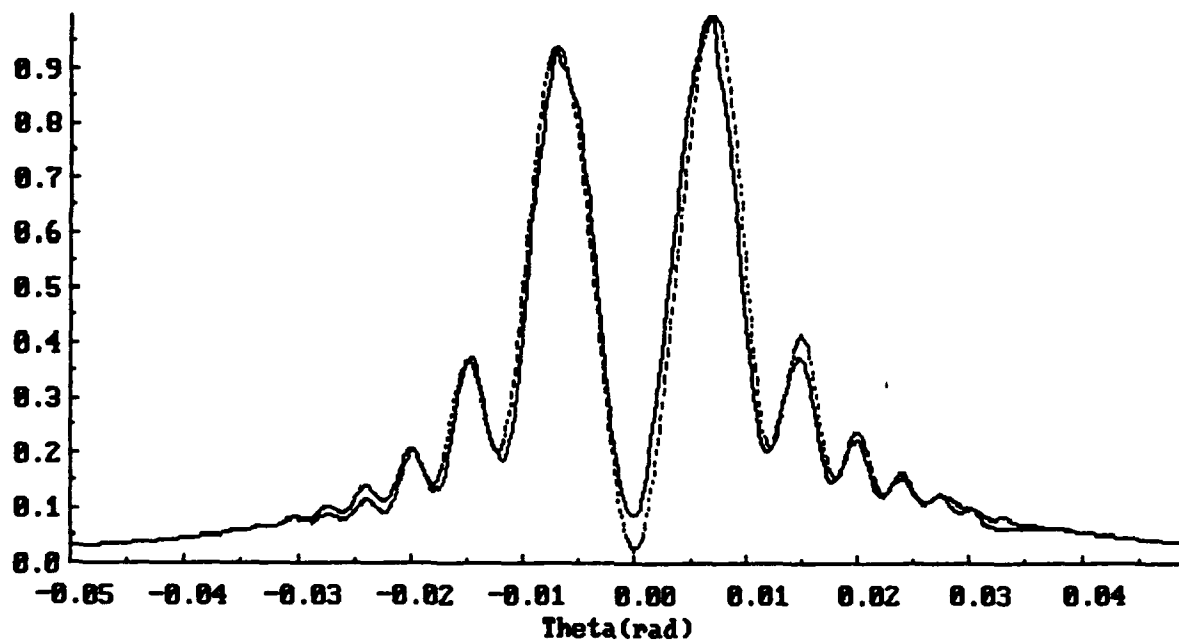


**Figure 40C:** The X-waist horizontally polarized, horizontal scan of IPAR for the nitrocellulose foil with a divergence of 0.8 mrad. Note that the fringe visibility is slightly less.

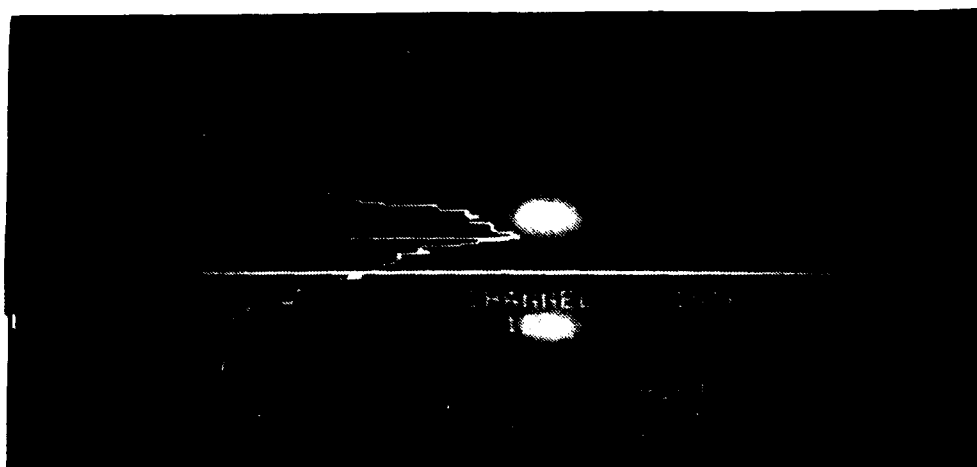


**Figure 41: X-waist vertically polarized, horizontal scan of IPERP SITCAM captured image.**

OTR25-10, X-WAIST, UP, HS, IPERP, DIU.=0.6 mrad

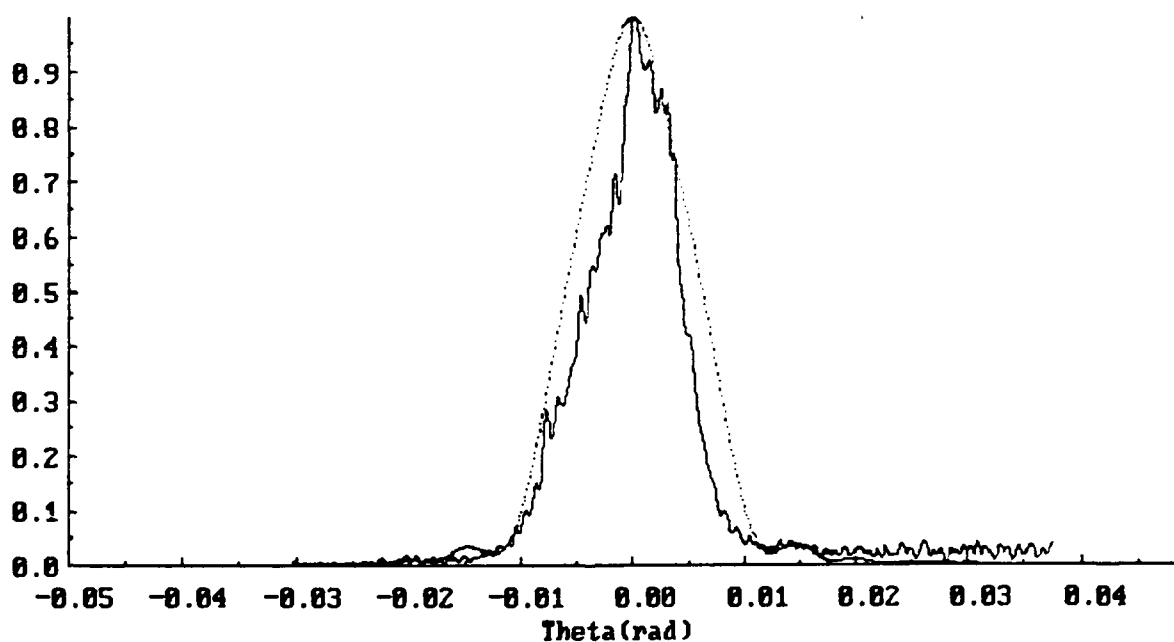


**Figure 42A: The X-waist IPERP graphical comparison to theory for an inputted divergence of 0.6 mrad.**

OTR25-10, X-WAIST, UP, HS, IPERP, DIV.=0.7 mrad

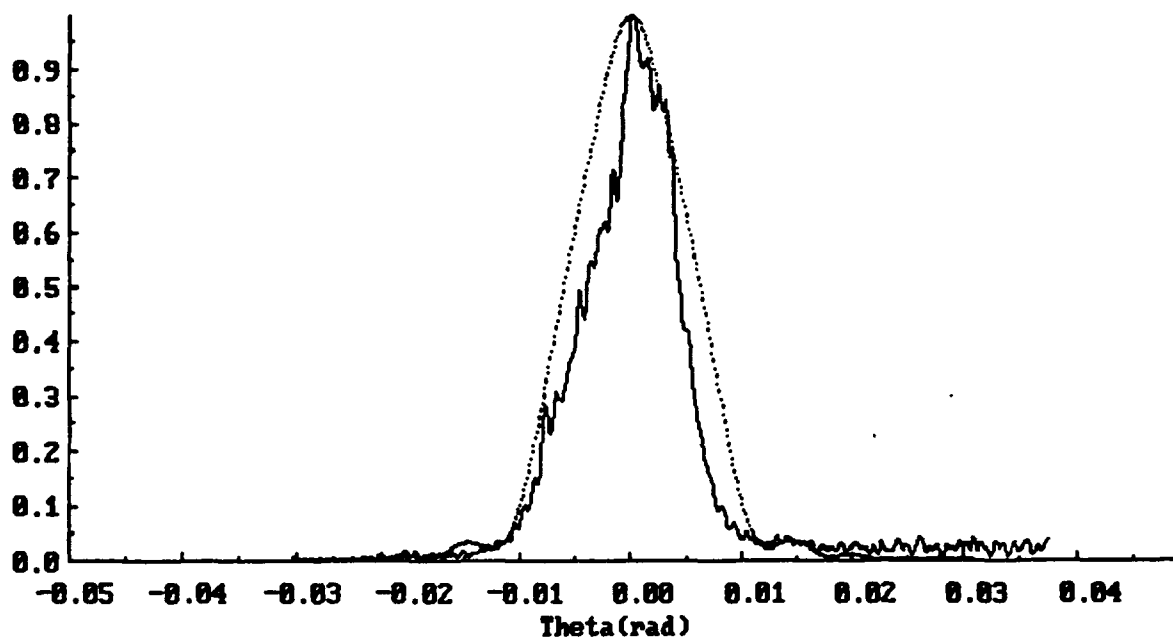


**Figure 42B: The X-waist vertically polarized, horizontal scan of IPERP for the nitrocellulose foil with a divergence of 0.7 mrad. The high background noise and the process of subtraction in the SITCAM causes the OTR patterns to exhibit only fair correlation, but enough to affirm the IPAR divergence measurement.**

OTR25-10, X-WAIST, UP, HS, IPERP, DIV.=0.8 mrad

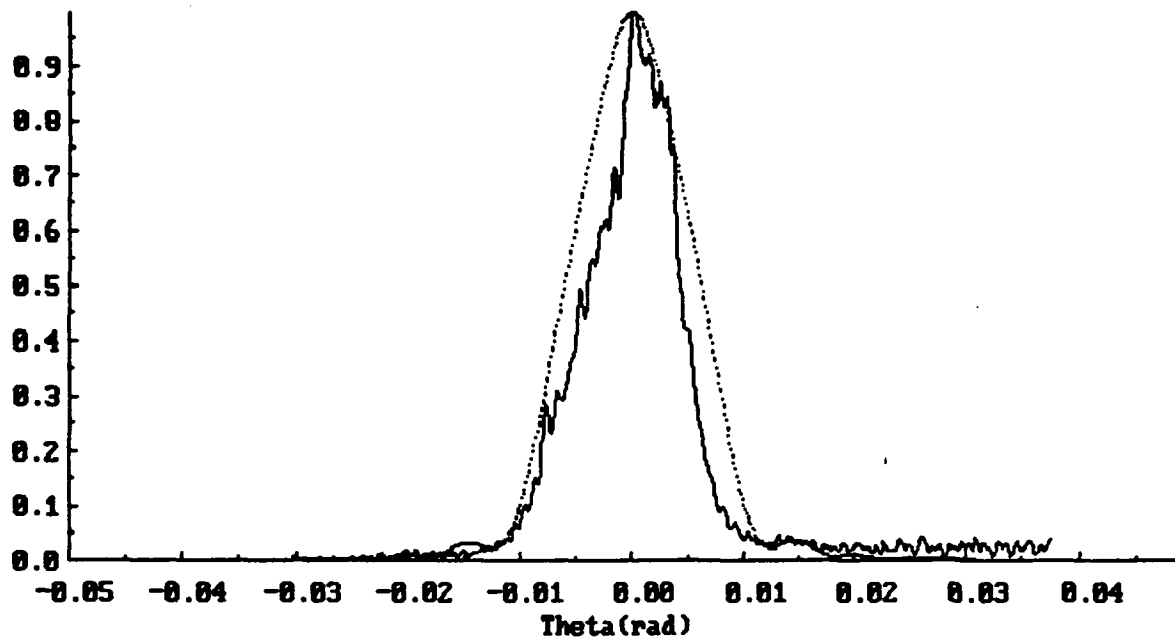


**Figure 42C: The X-waist vertically polarized IPERP OTR scan with an inputted divergence of 0.8 mrad. Note that the correlation is slightly less than the 0.7 mrad.**

The asymmetry for both the data and the theory match. Figures 40A and 40C are used for the error analysis, and these indicate that the nitrocellulose foil interferometer is very sensitive to the divergence. The X-waist divergence,  $\theta_x$ , is  $0.7 \pm 0.1$  mrad for x-emittance measurement. In order to further validate the divergence measurement, the vertically polarized, vertical scan of the X-waist IPERP intensity was taken, shown in Figure 41. Due to the over-efficient method of background subtraction in the SITCAM and the fact that the scan is through the dark center region, Figures 42A, 42B, and 42C display fair correlation of the theoretically generated OTR patterns for the X-waist vertically polarized IPERP scans to the data. Figure 42B supports the divergence correlation in Figure 40B. Therefore, the inputs to the x-emittance measurement are the RMS beam radius of  $2.43 \pm 0.1$  mm and the  $\theta_x$  divergence of  $0.7 \pm 0.1$  mrad.

Figure 43A displays the Y-waist beam spot and vertical intensity scan. The reflections were eliminated by masking. Consequently, when the beam intensity vertical scan is analyzed and plotted in Figure 44, the RMS Y-waist beam radius is  $1.05 \pm 0.1$  mm. Figure 43B shows the photo of the vertically polarized Y-waist OTR pattern captured from the SITCAM. Note the high degree of fringe visibility as compared to the Kapton foil measurement. Figures 45A, 45B, and 45C display the theoretically generated, Y-waist, vertically polarized, vertical scans of the IPAR compared to the data OTR scans. Figure 45B correlates the theoretical OTR pattern to the data with a divergence of 0.9 mrad. Figures 45A and 45C provide the error analysis of  $\pm 0.1$  mrad. The correlation is again very good for all of the figures, and the fringe sensitivity to the divergence is high. Finally, as a verification of the measurement, Figure 46

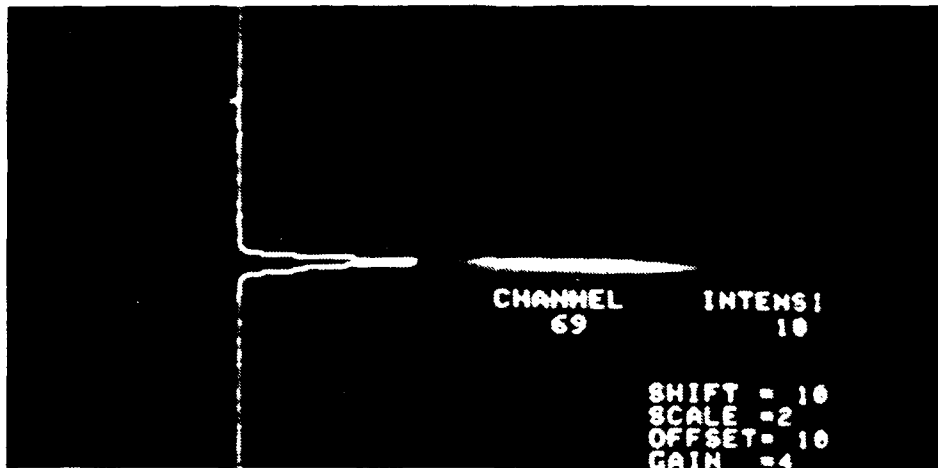


**Figure 43A: Photo of the Y-waist beam spot image.  
Reflections were not evident.**

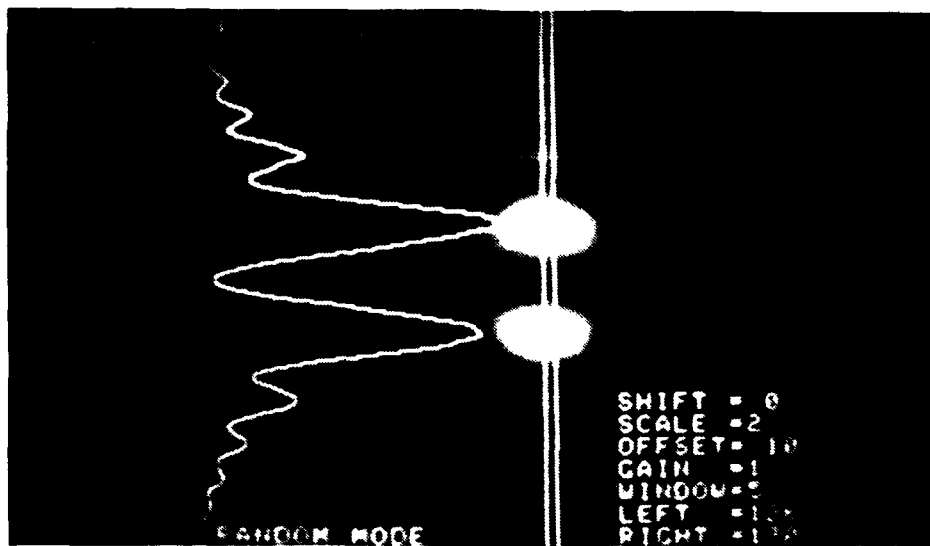


**Figure 43B: Photo of the Y-waist vertically polarized, vertical  
scan of IPAR used for the divergence measurement.**

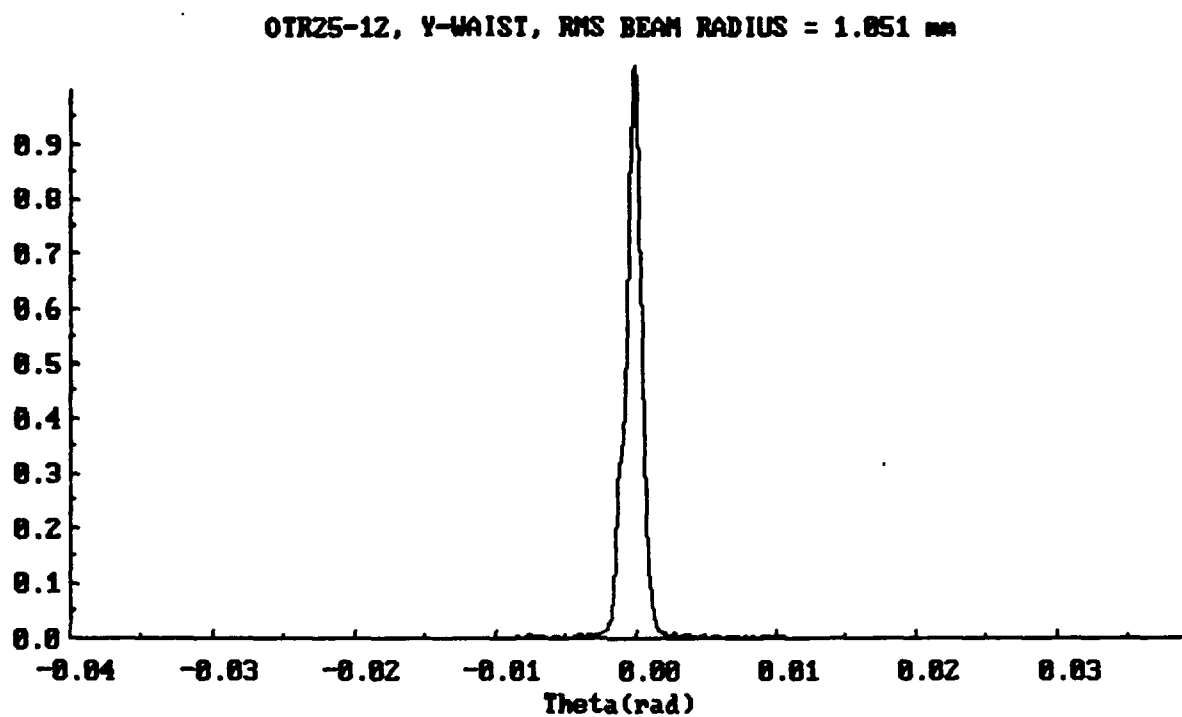


**Figure 44:** The Y-waist beam spot intensity scan, which yields the RMS Beam radius of 1.05 mm.

OTR25-14, Y-WAIST, UP, US, IPAR, DIV.=0.8 mrad

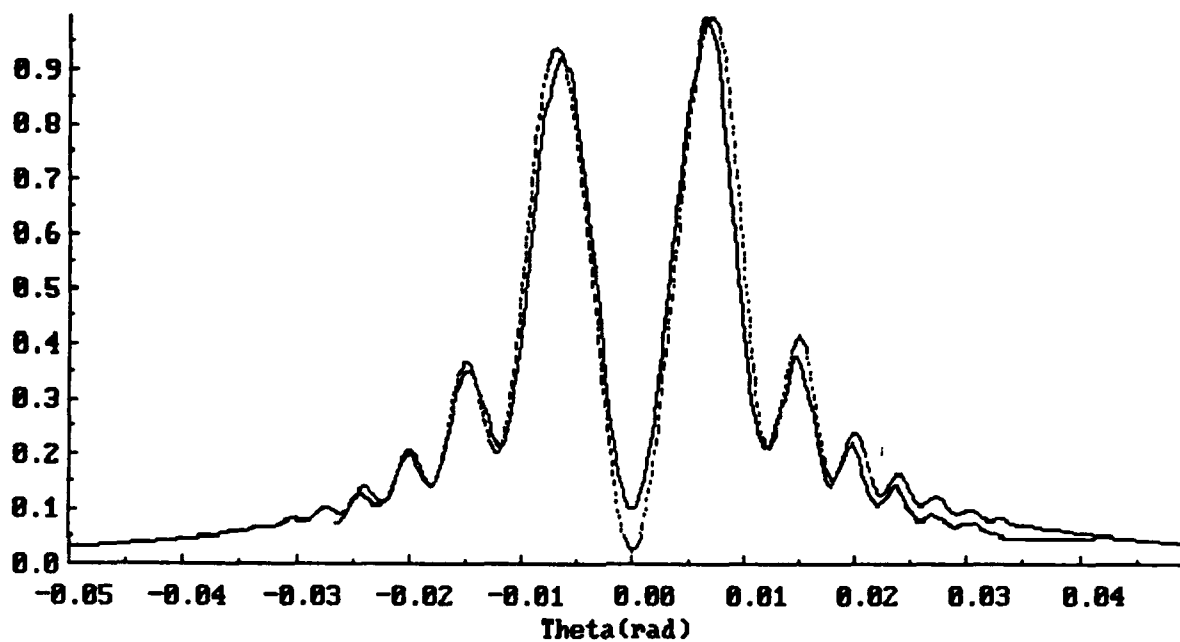


**Figure 45A: The Y-waist vertically polarized, vertical scan of IPAR with an inputted divergence of 0.8 mrad. Used in the error analysis.**

OTR25-14, Y-WAIST, UP, US, IPAR, DIV.=0.9 mrad

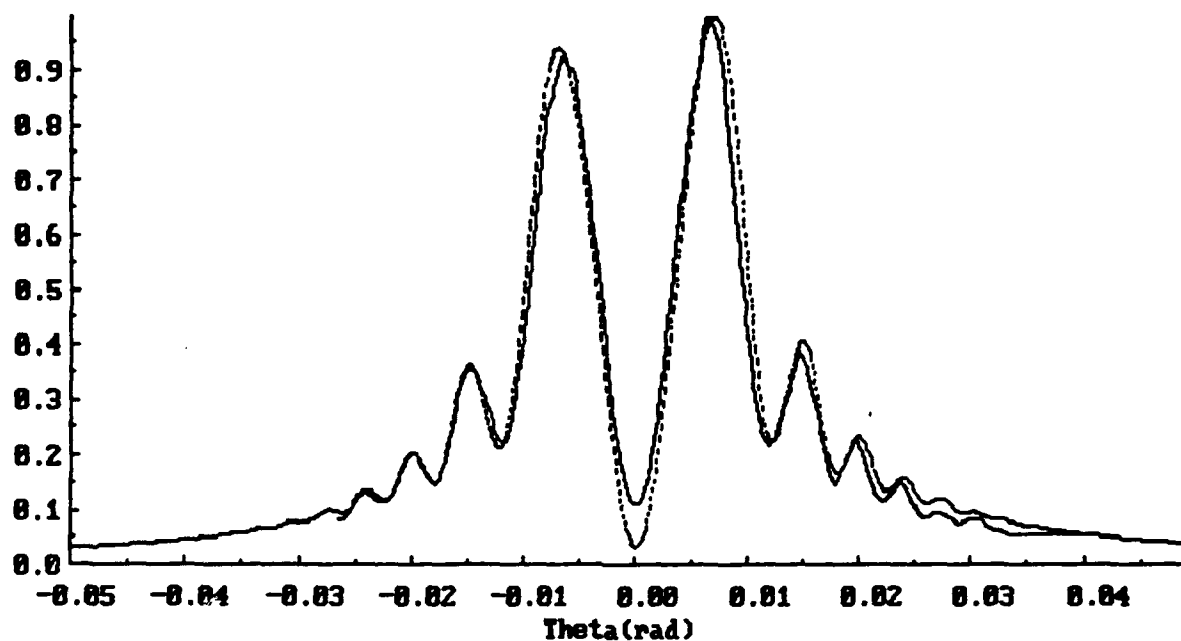


**Figure 45B: The Y-waist vertically polarized, vertical scan of the nitrocellulose foil IPAR OTR pattern with a divergence of 0.9 mrad used in the y-emittance measurement. Note the excellent fringe visibility and matching as compared to the Kapton foil.**

OTRZ5-14, Y-WAIST, UP, VS, DIV.=1.0 mrad

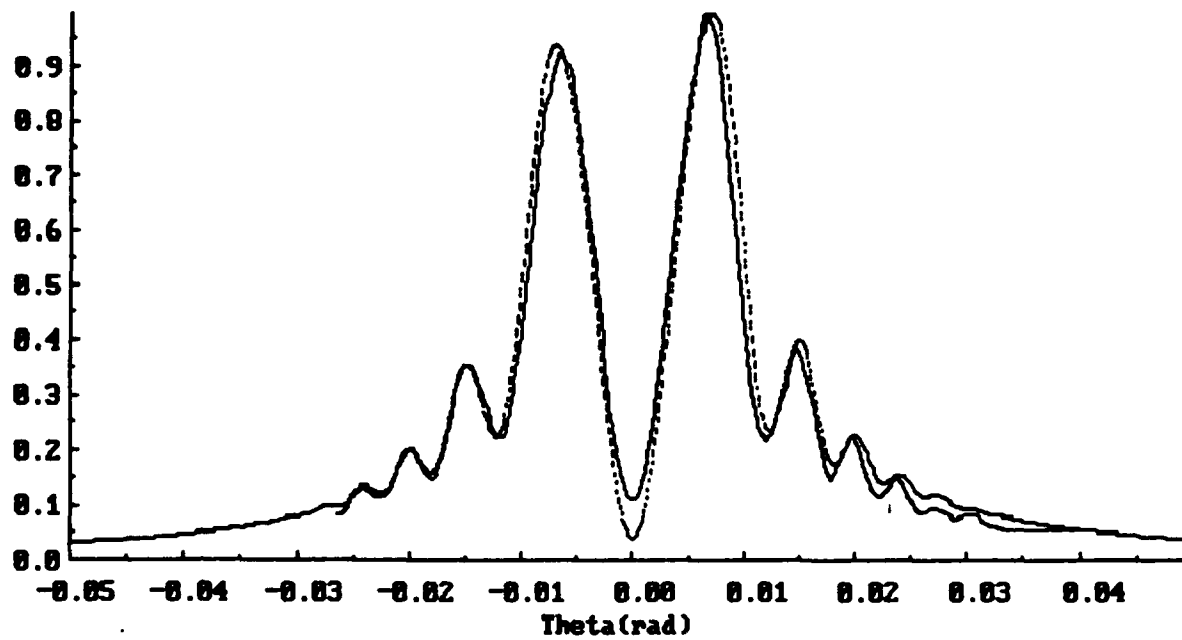


**Figure 45C: The Y-waist vertically polarized, vertical scan of IPAR with an inputted divergence of 1.0 mrad. The sensitivity of the theory to divergence is high.**

OTR25-13, Y-WAIST, HP, US, IPERP, DIV.=0.9 mrad

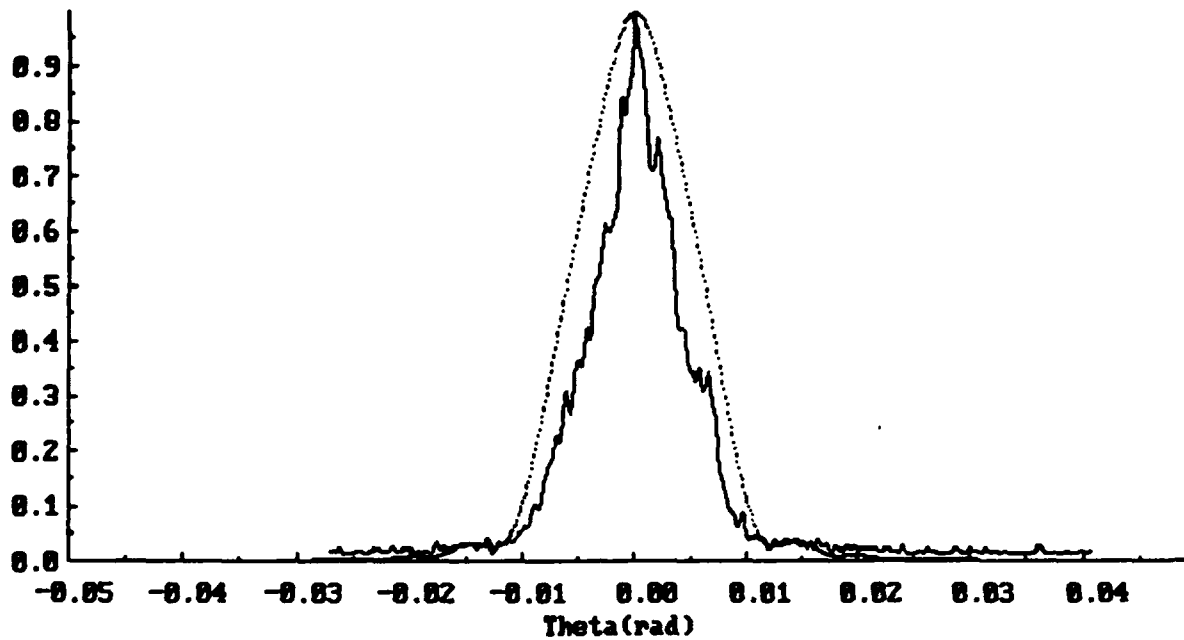


**Figure 46: The Y-waist horizontally polarized, vertical scan of IPERP for the nitrocellulose foil with a divergence of 0.9 mrad. The correlation is fair due to the background subtraction of the SITCAM probably being too great and thereby losing some information. The error analysis was consistent.**

correlates the horizontally polarized, vertical scan of the Y-waist IPERP to the actual IPERP data with a divergence of 0.9 mrad. Although not shown here, the error analysis yielded  $\pm 0.1$  mrad. Therefore, the inputs to the y-emittance measurement are the Y-waist RMS beam radius of  $1.05 \pm 0.1$  mm and a  $\theta_y$  divergence of  $0.9 \pm 0.1$  mrad.

Using equation (1), the unnormalized emittance values are:

$$\epsilon_x = 1.70 \text{ mm-mrad}$$

$$\epsilon_y = 0.95 \text{ mm-mrad.}$$

Using the Lorentz factor  $\gamma$  equal to 179 for 91.36 MeV electron energy, the normalized emittance values with error analysis are:

$$\epsilon_x = 97\pi \pm 10\pi \text{ mm-mrad}$$

$$\epsilon_y = 54\pi \pm 8\pi \text{ mm-mrad.}$$

## E. COMPARISONS TO OTHER LINACS

The first comparison is obviously between the two experiments using the Kapton foil interferometer and the Nitrocellulose foil interferometer as shown in Table I. The Kapton foil is viewed as an initial measurement to the normalized emittance, and yielded a horizontal emittance of  $95\pi \pm 34\pi$  mm-mrad and a vertical emittance of  $52\pi \pm 12\pi$  mm-mrad. These values are very good for the NPS linac given that it was built with 60's technology, and it is primarily designed for radiation studies and basic particle physics. The degree of error in the measurement is somewhat arbitrary given the aberrations in the data, but the estimation is conservative. The nitrocellulose foil used the lessons learned from the Kapton foil emittance measurement and improved data collection techniques to determine the emittance of the NPS linac more accurately. The nitrocellulose foil was thinner than the Kapton foil, and, consequently, the

nitrocellulose foil was highly sensitive to small changes in the input parameters. The nitrocellulose foil emittance measurement yielded a horizontal emittance of  $97\pi \pm 10\pi$  mm-mrad and a vertical emittance of  $54\pi \pm 8\pi$  mm-mrad. These numbers compare extremely well with the Kapton foil measurement. The errors overlap, and the increase in accuracy of the nitrocellulose foil measurement is evident. The margin of error in the normalized emittance measurements are 35% and 15% for the Kapton foil and the nitrocellulose foil respectively suggesting that the accuracy is increased by a factor of 2.

By taking a look at Table II, the emittance of the NPS linac is higher than the listed similar RF linacs. The emittance is only larger by one order of magnitude than the smallest emittance value. One must remember that the NPS linac is a product of the 1960's, and the newer accelerators such as the Los Alamos FEL and the Stanford Mark III RF linac are designed with better gun technology for FEL applications which require low emittance beams. The NPS linac compares very well with the LANL RF linac and the NBS L-band linac which are used mainly for radiation studies, and is of the same order of magnitude as the Boeing RF linac and the CEBAF injector, which is under construction. The NPS linac's emittance is too high for most FEL applications, but the emittance is low enough for radiation studies in high temperature superconductors, radiation hardening, coherent x-ray sources, and novel beam diagnostic studies which may have application to FEL advancement. The emittance of the NPS linac shows that the divergence of the beam is approximately 1 mrad for a beam radius of 1.75 mm circular, which is very good considering the age of the technology. The NPS linac has a good quality beam that is sufficient for a variety of purposes, and is currently being used to

**develop novel parametric x-ray sources using OTR techniques to monitor and diagnose the beam profile.**

<u>Date</u>	<u>Foil</u>	<u>Mirror</u>	<u><math>\epsilon_N</math>(mm-mrad)</u>
Sept. 1990	Kapton	Silicon	$\epsilon_x = 95 \pm 34\pi$ $\epsilon_y = 52 \pm 12\pi$
Nov. 1990	Nitrocellulose	Aluminum	$\epsilon_x = 97 \pm 10\pi$ $\epsilon_y = 54 \pm 8\pi$

**Table I: Comparison of the two emittance measurements**

<u>LINAC</u>	<u>ENERGY (MeV)</u>	<u><math>\epsilon_n</math>(mm-mrad)</u>
NPS	100	$\epsilon_x=97\pi; \epsilon_y=54\pi$
LANL	20	$50\pi$ [Ref. 24]
BOEING	150	$16\pi$ [Ref. 24]
CEBAF Injector*	80	$21\pi$ [Ref. 25]
LOS ALAMOS FEL	21	$2.5\pi$ [Ref. 26]
STANFORD MARK III	44	$\epsilon_x=4\pi; \epsilon_y=2\pi$ [Ref. 27]
NBS L-band	80	$84\pi$ (estimated) [Ref. 28]
NBS Microtron	180	$3\pi$ [Ref. 29]

\*under construction

**Table II: Comparison of the NPS Linac emittance to other accelerators of differing technologies.**

## V. CONCLUSIONS AND RECOMMENDATIONS

### A. CONCLUSIONS

The emittance of the NPS linac has been determined by means of two independent experiments using the OTR developed by a Kapton foil interferometer and a nitrocellulose foil interferometer. The Kapton foil is viewed as an initial measurement of the actual emittance, because of the novel technique and procedure of using OTR to determine the divergence of the beam. Aberrations in the data due to camera alignment and focus and reflection flares caused a greater uncertainty in the measurement of the divergence and the beam radius. The Kapton foil did not exhibit a high degree of sensitivity to the input parameters of bandwidth, indices of refraction, energy, foil thickness, and foil spacing, because the thickness of the foil was several orders of magnitude greater than the radiation coherence length in the foil, and, therefore, the OTR exiting the foil was fully developed and added coherently with the other radiation amplitudes. The normalized emittance values from the Kapton foil are:

$$\epsilon_x = 95\pi \pm 34\pi \text{ mm-mrad}$$

$$\epsilon_y = 52\pi \pm 12\pi \text{ mm-mrad}.$$

The nitrocellulose foil interferometer emittance measurement yielded more accurate results due to the lessons learned from the Kapton foil measurement and improved data collection. The experiment consisted of the emittance measurement with a preliminary investigation into the clear foil coherence effects. The nitrocellulose foil exhibited high degrees of sensitivity to

the input parameters when used in Rule's analytic program. First, the filter bandwidth caused washing out of the fringe visibility, and this phenomena is due to the Lorentzian filter model used in Rule's computer code. In order to temporarily correct the discrepancy, the filter bandwidth was narrowed by 10 nm to more closely model the actual filter function. This approximation performed very well in the data analysis. Second, the theoretically generated OTR exhibited high sensitivity to the index of refraction of the foil which is frequency dependent by equation (28). The 0.5  $\mu\text{m}$  and 5  $\mu\text{m}$  foil thicknesses were used to compare sensitivity and coherence effects. The thin foil exhibited a great sensitivity to the index of refraction, and the foil was able to "dial in" the index of refraction for a specific frequency bandwidth. The thicker foil exhibited some sensitivity to the index of refraction in the asymmetry of the OTR pattern, but not to the degree of the thin foil. The conclusion is that the thin foil is very close to the radiation coherence length of the foil medium, and by varying the index of refraction the foil thickness may be smaller or larger than the coherence length. This situation causes the OTR exiting the foil to either not be fully developed and not adding coherently with the other OTR amplitudes or to be fully developed and the processes of interference are dominant. By varying the thicknesses of both foils within their margin of error, the above discussion is supported. The thicker foil exhibited little if any sensitivity to the change in the thickness of the foil. On the other hand, the thin foil exhibited high sensitivity when the foil thickness was reduced only by 10 percent, because the thickness of the foil was less than the coherence length in the medium. From these sensitivity measurements, the input parameters to Rule's computer code were determined with a high degree of confidence

supplied by the thin foil coherence effects. The normalized emittance values were determined using OTR with a high degree of confidence and are:

$$\epsilon_x = 97\pi \pm 10\pi \text{ mm-mrad}$$

$$\epsilon_y = 54\pi \pm 8\pi \text{ mm-mrad}.$$

These emittance values compare very well with the Kapton foil emittance measurement, and show the utility of OTR as a beam diagnostic even without optimum conditions for data collection. The nitrocellulose foil coherence effects and the emittance measurement validate the code used by Rule in the computer analysis. Due to the higher degree of confidence and sensitivity in the nitrocellulose foil experiment, the NPS linac emittance are the values measured in the second experiment with the nitrocellulose foil.

The NPS linac has a good emittance value given its technology. The emittance compares well with the LANL RF linac used for radiation studies and is on the order of magnitude with more modern linacs such as the Boeing RF linac and CEBAF Injector, which indicates that beam diagnostic techniques developed at NPS have applications to machines. In fact, Rule et al. have applied these techniques to the Los Alamos FEL and Boeing FEL [Ref. 6-8].

## B. RECOMMENDATIONS

The above experiments demonstrate the unique properties of Optical Transition Radiation as a beam diagnostic at a reasonable cost without cumbersome equipment and complicated beam transport models. The NPS emittance measurement was obtained in one day of data collection, albeit many weeks of thought and preparation were expended. Rule's analytic computer code accurately correlates the theory to the observed data OTR radiation patterns, and is invaluable to the analysis of beam characteristics. The OTR

patterns revealed beam quality problems, and pointed to the direction in which to solve them. The following paragraph suggests improvements to the techniques and recommendations for future work.

The filter model in Rule's computer code must be reconfigured to analyze with the measured filter profile provided normally by the manufacturer. This can be accomplished by digitizing the filter profile for input to the program or choosing a filter that approximates the filter model. By choosing a thinner foil on the order of the radiation coherence length, more accurate measures of the input parameters are obtained, and, consequently, the OTR patterns can determine the observed index of refraction and show high degrees of sensitivity to the divergence of the pattern. Rule's computer program can be used as a real time diagnostic tool to determine the expected OTR pattern during the experiment to correct early on any beam quality problems. A suggested experiment is to develop an interferometer foil spacing large enough to look between the foils, which eliminates the small attenuation effect and should increase the clear foil coherence effects. There is a possibility of developing the experiment to look at the OTR amplitudes developed by the clear foil separately. Currently, OTR is being used at the NPS linac to monitor beam quality for the parametric x-ray experiment.

## LIST OF REFERENCES

1. Frank, I. M., and Ginsburg, V. L., *Radiation of a Uniformly Moving Electron Due to Its Transition from One Media to Another*, Zhurnal Eksperimental'noi i Teoreticheskoi Fiziki, Vol. 16, 1946.
2. Ginsburg, V. L., and Tsytovich, V. N., *Several Problems of the Theory of Transition Radiation and Transition Scattering*, Physics Reports, Vol. 49, No. 1, 1979.
3. Ter-Mikaelin, M. L., High-Energy Electromagnetic Processes in Condensed Media, (Wiley-Interscience, New York, 1972).
4. Garibian, G. M., *Theoretical Foundations of Transition Radiation*, Soviet Physics JEPT, Vol. 10, 1960.
5. Wartski, L., *Study on the Optical Transition Radiation Produced by 30 to 70 MeV Energy Electrons. Application to Diagnostics of Beams of Charged Particles*, Ph. D. Dissertation, The Universite de Paris-Sud, Centre D'Orsay, France, 1976.
6. Rule, D. W., and Fiorito, R. B., *Transition Radiation Diagnostics for Intense Charged Particle Beams*, Nuclear Instruments and Methods in Physics Research, B24/25, North Holland, Amsterdam, Netherlands, 1987, pp. 901, 904.
7. Fiorito, R. B., et al., *Optical Transition Radiation Diagnostics for Low Emittance, High Energy, Charged Particle Beams*, paper presented at EPAC proceedings of the European Particle Accelerator Conference, June 7-11, 1988.
8. Iversen, S. G., et al., *Charged Particle Beam Divergence Measurements Using Transition Radiation*, IEEE Particle Accelerator Conference, March 16-19, 1987, pp. 573-575.
9. Bosser J., et al., *Optical Transition Radiation Proton Beam Profile Monitor*, submitted for publication to Nuclear Instruments and Methods, 1984.
10. Naval Surface Weapons Center Report TR 84-134, *The Use of Transition Radiation as a Diagnostic for Intense Beams*, by Dr. D. W. Rule and Dr. R. B. Fiorito, Silver Spring, Maryland, July 1984.

11. Lumpkin, A. H., et al., *Initial Optical Transition Radiation Measurements of the Electron Beam for the Boeing Free-Electron Laser Experiment*, Nuclear Instruments and Methods in Physics Research, A296, North-Holland, Amsterdam, Netherlands, pp. 150-158.
12. Reid, C., *Procedures for Electron Beam Emittance and Profile Measurements using Optical Transition Radiation*, Master's Thesis, Naval Postgraduate School, Monterey, California, December 1990.
13. Wartski, I., et al., *Interference Phenomena in Optical Transition and its Application to Particle Beam Diagnostics and Multiple-Scattering Measurements*, Journal of Applied Physics, Vol. 46, No. 8, August 1975, pp. 3644-3653.
14. Yuan, Luke C. L., et al., *Formation-Zone Effect in Transition Radiation Due to Ultrarelativistic Particles*, Physics Review Letter, Vol. 25, No. 21, 1970, p. 1513.
15. Pafamov, V. E., *Proceeding of the P. N. Lebedev Physics Institute*, edited by D. V. Skobel'tsyn (Consultants Bureau, New York, 1971), Vol. 44, pp. 25-157.
16. Wartski, L., et al., *Detection of Optical Radiation and Its Application to Beam Diagnostics*, IEEE Transactions in Nuclear Science, Vol. 20, 1973, p. 544.
17. Ashley, J. C., *Transition Radiation from Thin Foils due to Non-Normally Incident Electrons*, Physics Review, Vol. 155, No. 2, 1967, p. 208.
18. Longstaff, W. G., *Three-Dimensional Analysis of Optical Transition Radiation*, Master's Thesis, Naval Postgraduate School, Monterey California, December 1988, pp. 86-90.
19. Private Communication and Notes between Dr. Donald W. Rule, Naval Surface Weapons Center, Silver Spring, Maryland, and author, March - September 1991.
20. IBM Personal Computer Version, *Crosstalk VI*, Revision 3.61, Microstuf Inc., California, 1986.
21. National Photocolor Corporation, *Beam Splitting with NPC Pellicles*, Sales Brochure, National Photo Corp., Mamaroneck, New York, 1990.

22. Handbook of Optical Constants, edited by Edward D. Palik, Academic Press Inc., 1985.
23. Moller, K. D., Optics, University Science Books, Millvalley, California, 1988, pp. 278-294.
24. Roberson, C. W., and Sprangle, P., *A Review of Free Electron Lasers*, Naval Research Lab, published in Physics of Fluids, Vol. 1, 1989, p. 81.
25. Private communication between Dr. William B. Colsen, Naval Postgraduate School, Monterey California, and author, May 1991.
26. Watson, J. M., *Status of the Los Alamos Free Electron Laser*, Nuclear Instruments and Methods in Physics Research, A250, North-Holland, Amsterdam, Netherlands, 1986, pp. 1-3.
27. Benson, S. V., et al., *First Operation of the Rocketdyne/Stanford Free Electron Laser*, Nuclear Instruments and Methods in Physics Research, A272, North-Holland, Amsterdam, Netherlands, 1988, pp. 10-14.
28. Private communication between Dr. Ralph Fiorito, Naval Surface Weapons Center, Silver Spring, Maryland, and author, August 1991.
29. Private communication between Professor X. K. Maruyama, Naval Postgraduate School, Monterey California, and author, August 1991.

## APPENDIX A

This appendix describes the operation of the interface subroutine used in conjunction with Rule's clear foil program for data obtained by the SITCAM and recorded by the HP Plotter or the XTALK data conversion program installed in the Compaq II portable computer.

First, edit (using the 'edlin' command in DOS) the GAUSIN.DAT input parameters file. The setup of the file is as follows:

line 1: 1, 3, 0, 1, 1, 1; these are the radiation amplitude codes for the main program. The fifth 1 is the clear foil on/off (1/0) code indicator.

line 2: beam energy(MeV), foil spacing parallel to the beam (cm), foil thickness parallel to the beam (cm)

line 3: lower filter bandwidth (angstroms), upper filter bandwidth (angstroms), refractive index n of the foil, k of th foil (0.0 for clear foils), n of the mirror, k of the mirror.

line 4: lower graphical range (radians), upper graphical range (radians), range steps

line 5: x-divergence (radians), y-divergence (radians), 3.

Edit the file as necessary to input the parameters of the specific experiment and interferometer used.

Second, edit the SITCAM files, either digitized or in an ASCII format, to remove negative inputs caused by the background subtraction. Finally, call up Rule's main program GINTRF1, which was written in FORTRAN, installed on the Compaq II IBM portable computer. The program will automatically call up the DATAOTR.FOR subroutine to interface the data with the program. The

sequence of events is:

"Would you like to plot real points (Y/N)?" answer 'Y'.

"(T)heory file?; (D)igitized file?; (O)TR file?, which type of data file is it?" Specify the file by letter.

"Type the data file with extension;" type the data filename which has been copied to the C:\ directory.

For Theory data, the program will automatically calculate the theoretical OTR pattern for the given inputs, and then send it to the plotter routine.

For the Digitized data: "Input the number of data points;" type in the exact number of points. For the OTR data the number of points is not necessary, because it reads to the end of the file.

"The factor is> 3.04E-04 radians/pixel, do you want to change it? (Y or <cr>). If 'Y', "enter factor>", enter the new calibration, or hit <cr>.

"The e-factor is>0.00 mm/pixel, do you want to change it? (Y or <cr>). If this is a beam spot profile, type 'Y', and the computer will ask: "enter the e-factor>'. Enter the mm/pixel conversion.

"Do you want to flip the data? y/n. Answer 'y', because the data conversion program flips the data when it records.

"Do you want to subtract background? y/n. Normally, type 'n', because the SITCAM can background subtract. The background subtraction is in whole number increments of intensity.

If 'y' is typed, the computer will ask: "enter your background value," and enter a whole number of pixel intensity.

At this point the computer starts to setup the graphical calculations. "What is the center of the graphical data?" Enter the pixel location of the center minimum of the data OTR pattern. The program does not calculate this, but must be entered manually.

The computer performs the data file read, calculating the vertical maximum of the data for normalization, and the width of the pixels.

The computer asks: "Is this a beam spot profile?" y/n. If 'y', the computer automatically calculates the RMS beam radius and prints it on the screen: "The (mm) measurement of the beam spot is: XXXX."

The computer will then go directly to the graphics subroutine, or, if 'n', will calculate the theoretical OTR patterns using the input parameters. The computer also prints the input parameters to the screen.

The computer leaves this subroutine and goes into the GRAFPLUS subroutine for plotting the data. "enter interval for tic marks on the x-axis of the plot". Enter .01.

"How many plots on the same plane?" Enter 1,2, or 3. Usually 2 is sufficient for comparison.

"IP(E)RP?; IP(A)R?; (W)=ITOT?; (D)ATA FILE?; type the letter of the plot?" The computer will prompt as many times as the number of plots requested. Type the letter of the desired plot. Hit return after each.

"Type the title (up to 50) characters of the plot." Type the title of the plot not to exceed 50 characters. Hit return, and the computer will plot the data against the theory. The theory is (---) dashed lines, and the data is solid lines. The graphical output is hooked up to the HP Laserjet II printer, and takes approximately 5 minutes to output a hard copy.

Prior to running the graphics program, run GRAFLSR1 and follow the prompts using (1) for the HP Laserjet and (0) for the PC screen mode. The questions on graphical output should be answered: Y, N, N, Y.

"Would you like to see another plot? y/n." If 'y', the program will retreat back to: "How many plots on the same page?". The procedure is repeated. If 'n', the program releases the user back to the main program for another run. Type GINTRF1 and use another data set or different parameters.

This is the operation of the clear foil interferometer OTR program. Normally, the divergence of the GAUSIN.DAT file is the only parameter adjusted when fitting the data. The subroutine could be improved by finding the center of the data automatically. A better graphics program would also

increase the visual effectiveness of the data comparison. By following the above bullets, one can operate and interface with Rule's computer code. For the future users of Optical Transition Radiation, the following pages contain a copy of the interface program, DATAOTR.FOR.

```

SUBROUTINE DATAOPT(DX,DY,NDAT)
C THIS SUBROUTINE WAS WRITTEN TO INCORPORATE THE HAMAMATSU CAMERA DATA
C INPUTS INTO THE MAIN PROGRAM OF GINTRF1. THE PROGRAM WAS WRITTEN BY
C LT. MARK HELLSTERN ON 28 FEBRUARY 1991 WITH THE INVALUABLE ASSISTANCE
C OF MY ESTEEMED MENTOR DR. DONALD RULE.
C
C NOTE:
C THE NEGATIVE DATA INPUTS IN THE DATA FILES NEED TO BE EITHER ELIMINATED
C OR MODIFIED FOR THEM TO BE READ. THIS SUBROUTINE STARTED OUT BY REMOVING
C THE NEGATIVE SIGNS ON THE DATA SINCE THE BACKGROUND NOISE COULD ACCOUNT
C FOR THIS PHENOMENA. THE OTR DATA IS FROM THE NOVEMBER 1990 OTR EXPER.
character ch*1, char*1, datfil*20, char3*1, char4*1
real midx, midy, factor, x1, y1, x2, factor1
integer ndat
REAL DX(640), DY(640), CY(640), dz(4)
iback=0
WRITE(*,*) 'would you like to plot real data points (Y/N)? '
82 read(*,82) ch
format(a)
if (ch.eq.'Y' .or. ch.eq.'y') then
write(*,*) ' (T)heory file ?'
write(*,*) ' (D)igital data file?'
write(*,*) ' (O)TR file ?'
WRITE(*,*) 'what type of data file is it?: '
45 read(*,45) char
format(a)
write(*,*) 'type the data file name, with extension: '
78 read(*,78) datfil
format(a20)
OPEN(4, FILE=datfil, STATUS='OLD')
REWIND 4
C
C OTR DATA
C
if(char .eq. 'o' .or. char .eq. 'O') then
ndat = 224
factor=3.04e-04
170 write(*,*) 'the factor is>', factor, 'radians/pixel'
write(*,*) 'do you want to change it? y or <cr>>'
read(*,45) char
if (char .eq. 'y' .or. char .eq. 'Y') then
write(*,*) 'enter factor>'
read(*,*) factor
endif
write(*,*) ' the e-factor is>', factor1, 'mm/pixel'
write(*,*) ' do you want to change it? y or <cr>>'
read(*,45) char
if (char .eq. 'y' .or. char .eq. 'Y') then
write(*,*) 'enter the e-factor>'
read(*,*) factor1
endif
write(*,*) 'do you want to flip the data? Enter Y or N'
read(*,45) char
write(*,*) 'do you want to subtract const backgrnd? y/n'
read(*,45) char3
if(char3 .eq. 'y' .or. char3 .eq. 'Y') then
write(*,*) 'what is your background value?'
read(*,*) iback
endif
if(char .eq. 'y' .or. char .eq. 'Y') then
istart = ndat
ifin = 1
incr = -1
isign = 1
else
istart = 1
ifin = ndat

```

```

        incr = 1
        isign = 1
    endif
    read(4,*)yy
    read(4,*)zz
    dymax=-500.
    write(*,*)'what is the center of the OTR data?'
    read(*,*)midx
    read(4,*) (dy(i),i=istart,ifin,incr)
    do 172 i= istart,ifin,incr
        dy(i)=dy(i)-iback
        if (dymax .lt. dy(i)) then
            dymax=dy(i)
            idymax=i
        endif
        dx(i)=float(i)
C
C dx(i) is now the flipped difference from the center in radians
C dymax is the maximum intensity of the horiz scan, and is at idymax
C
172     continue
        close(4)
        do 173 i=1 , ndat
            dy(i)=dy(i)/dymax
            j=i/25
            if(j*25 .eq. i) write(*,*)dx(i),dy(i)
173     continue
        write(*,*)'vert: maximum of ',dymax,' at ',dx(idymax)
C
C BEAM SPOT MEASUREMENT
C
        x1=0
        x2=0
        write(*,*) 'is this a beam spot profile? y/n'
        read(*,45) char4
        if (char4 .eq. 'y' .or. char4 .eq. 'Y') then
            do 177 i=1,ndat
                x1=dy(i) * ((midx-dx(i))**2) + x1
                y1=dy(i) + y1
                x2= (x1/y1)**0.5*factor1
                dx(i)=isign*(float(i)-midx)*factor
            continue
177         else
                do 182 i=1,ndat
                    dx(i)=isign*(float(i)-midx)*factor
                continue
182         endif
        write(*,*) ' The (mm) measurement of the beam spot:',x2
C
C END OF THE OTR DATA INPUT
C
        elseif (char .eq. 'T' .or. char .eq. 't') then
            write(*,*)'type 1_iperp, 2_ipar, 3_itot, 4_polarization'
            read(*,*) nt
            read(4,111) xdum
            read(4,111) xdum
            read(4,111) xdum
111         format(5(e14.7,1x))
            read(4,*) ndat
            do 113 ii=1,ndat
                read(4,111) dx(ii),dz(1),dz(2),dz(3),dz(4)
                dy(ii)=dz(nt)
113         continue
C
C DIGITAL DATA CONVERSION FROM SCAN PROGRAM
C

```

```

elseif(char .eq. 'd' .or. char .eq. 'D') then
write(*,*) 'input the number of data points>'
read(*,*) ndat
factor=3.04e-04
write(*,*) 'the factor is>',factor,'radians/pixel'
write(*,*) 'do you want to change it? y or <cr>>'
read(*,45) char
    if (char .eq. 'y' .or. char .eq. 'Y') then
        write(*,*) 'enter factor>'
        read(*,*) factor
    endif
write(*,*) 'the e-factor is>',factor1,'mm/pixel'
write(*,*) 'do you want to change it? y or <cr>>'
read(*,45)char
    if (char .eq. 'y' .or. char .eq. 'Y') then
        write(*,*) 'enter the e-factor>'
        read(*,*) factor1
    endif
write(*,*) 'do you want to flip the data? enter y/n'
read(*,45) char
write(*,*) 'do you want to subtract background? y/n'
read(*,45) char3
if (char3 .eq. 'y' .or. char3 .eq. 'Y') then
    write(*,*) 'enter your background value>'
    read(*,*) iback
endif
if (char .eq. 'y' .or. char .eq. 'Y') then
    istart = ndat
    ifin=1
    incr=-1
    isign=-1
else
    istart=1
    ifin= ndat
    incr= 1
    isign= 1
endif
dymax=-500
write(*,*) 'what is the center of the DIGITAL DATA?'
read(*,*) midx
do 272 i= istart,ifin,incr
    read(4,*)dx(i),dy(i)
    dy(i)= dy(i) -iback
    if (dymax .lt. dy(i)) then
        dymax= dy(i)
        idymax= i
    endif
272 continue
close (4)
do 273 i=1,ndat
    dy(i)=dy(i)/dymax
    j=i/25
    if (j*25 .eq. i) write(*,*)dx(i),dy(i)
273 continue
write(*,*) 'vert: max of',dymax, 'at' , dx(idymax)
c
c end of digital data output
c
x1=0
x2=0
write(*,*) 'is this a beam spot profile?y/n'
read(*,45) char4
if (char4 .eq. 'y' .or. char4 .eq. 'Y') then
    do 373 i=1,ndat
        x1=dy(i) * ((midx-dx(i))**2) + x1
        y1= dy(i) + y1
    enddo
endif

```

```

x2= (x1/y1)**0.5 * factor1
dx(i) = isign * (dx(i)-midx) * factor
373 continue
    else
        do 473 i=1,ndat
            dx(i) = isign * (dx(i)-midx) * factor
473 continue
        endif
    endif
write(*,*) 'The (mm) measurement of the beam spot:', x2
ENDIF
RETURN
END

```

## INITIAL DISTRIBUTION LIST

	No. Copies
1. Defense Technical Information Center..... Cameron Station Alexandria, Virginia 22314-6145	2
2. Library, Code 52..... Naval Postgraduate School Monterey, California 93943-5002	2
3. Dr. K. E. Woehler, Code Ph/Wh..... Department of Physics Naval Postgraduate School Monterey, CA 93943-5002	1
4. Professor X. K. Maruyama, Code Ph/Mx..... Department of Physics Naval Postgraduate School Monterey, CA 93943-5002.	2
5. Lt. Mark J. Hellstern, USN..... Reactor Controls Assistant Reactor Department USS Carl Vinson, CVN 70 FPO Seattle, WA 98729-2840	1
6. Professor F. E. Buskirk, Code Ph/Bs..... Departement of Physics Naval Postgraduate School Monterey, CA 93943-5002	1
7. Professor J. R. Neighbours, Code Ph/Nb ..... Department of Physics Naval Postgraduate School Monterey, CA 93943-5002	1

8. Dr. R. B. Fiorito, Code R41..... 1  
Naval Surface Weapons Center  
10901 New Hampshire Avenue  
Silver Spring, MD 20903-5000
9. Dr. D. W. Rule, Code R41..... 1  
Naval Surface Weapons Center  
10901 New Hampshire Avenue  
Silver Spring, MD 20903-5000
10. Dr. M. A. Piestrup..... 1  
Adelfi Technology, Inc.  
532 Emerson Street  
Palo Alto, CA 94301
11. Mr. D. Snyder, Code 61Ph..... 1  
Department of Physics  
Naval Postgraduate School  
Monterey, CA 93943-5002
12. Professor C. W. Colsen, Code Ph/Cw ..... 1  
Department of Physics  
Naval Postgraduate School  
Monterey, CA 93943-5002